Recent Advances in Ocean Acoustic Waveguide Remote Sensing and Nonlinear Ocean Acoustic Sensing

Nicholas C. Makris
Massachusetts Institute of Technology

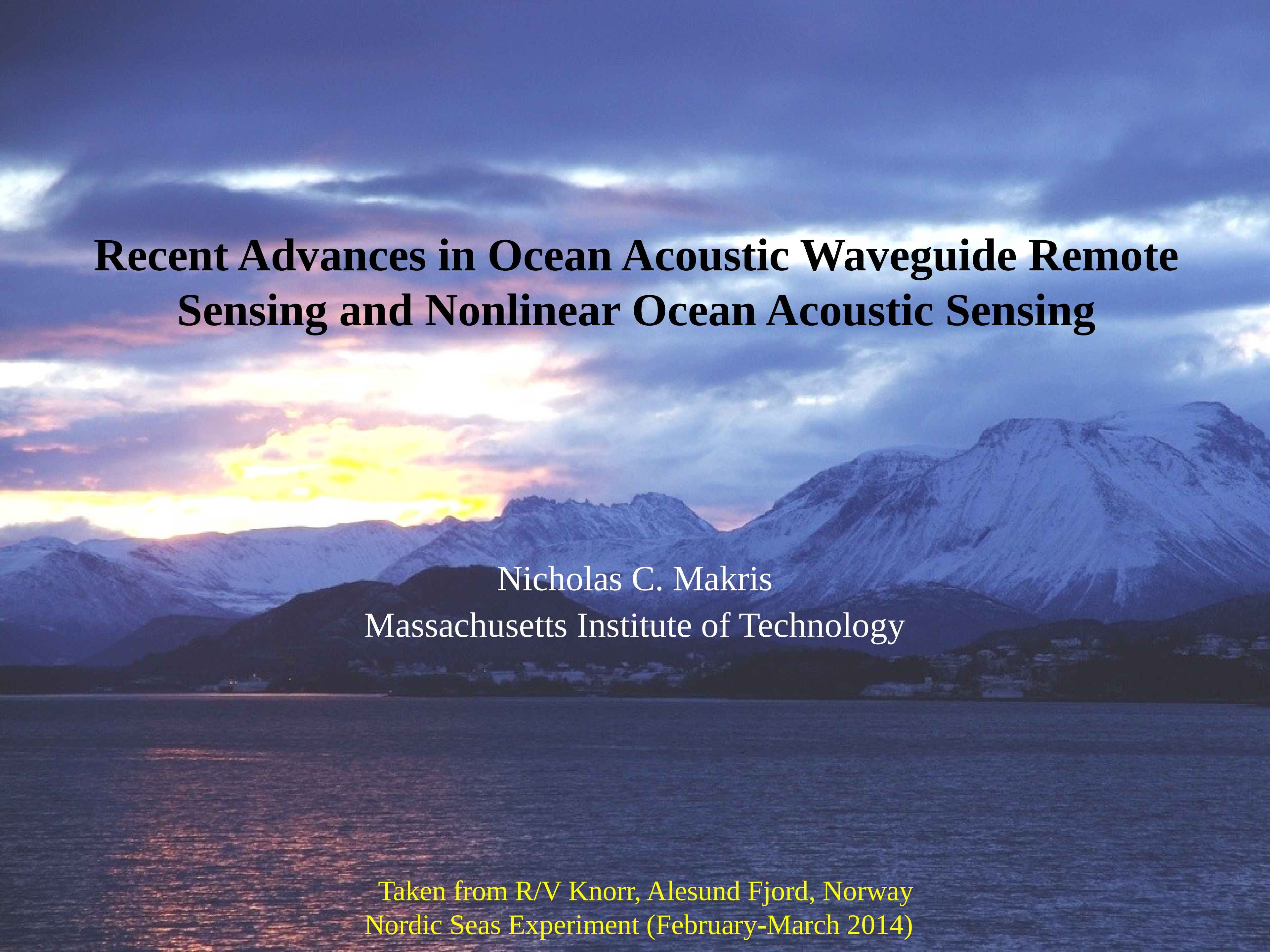

Taken from R/V Knorr, Alesund Fjord, Norway
Nordic Seas Experiment (February-March 2014)

Nordic Seas Experiment 2014
Overview of Cruise Tracks

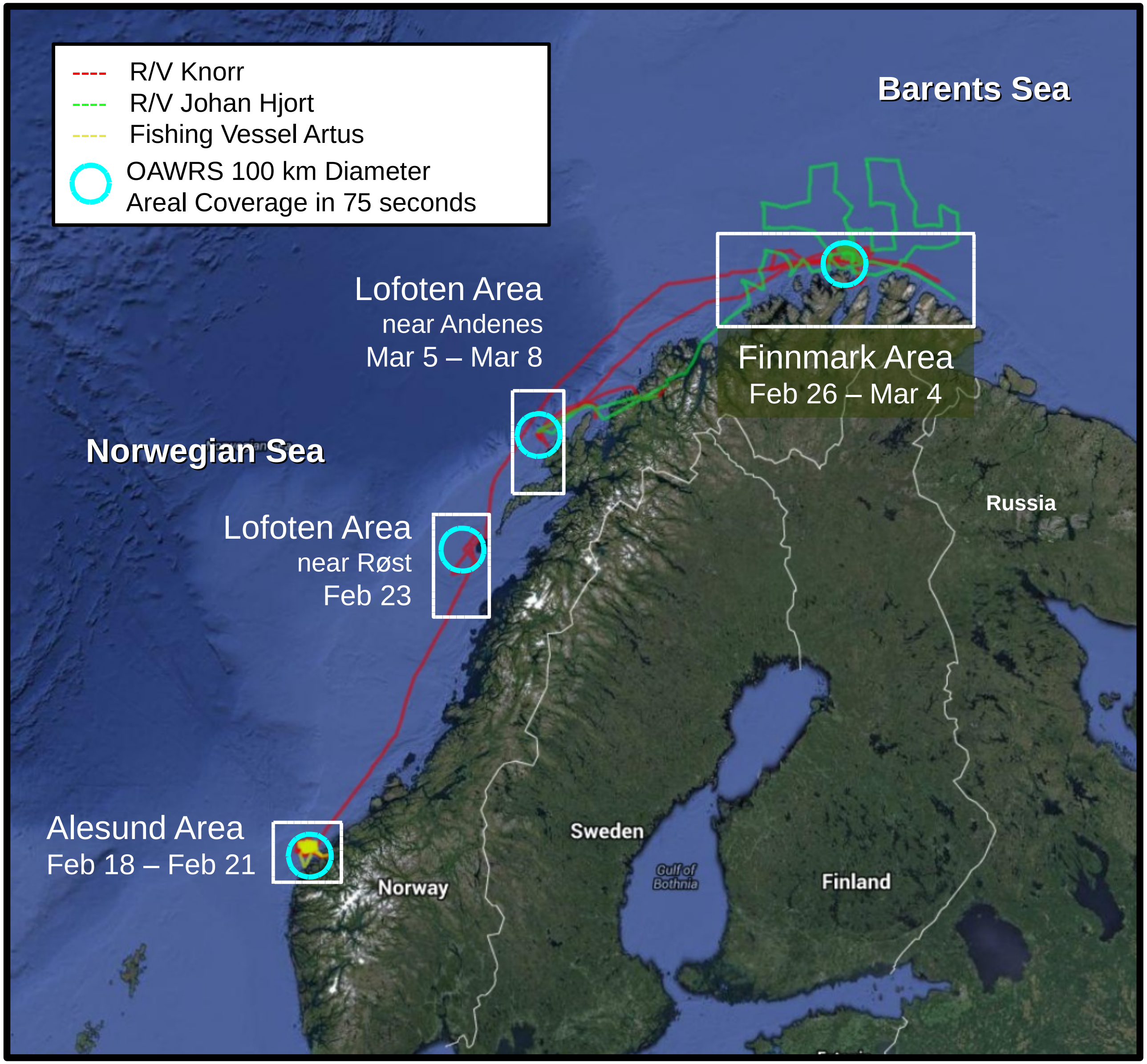

Wide-Area Towed Monostatic Ocean Acoustic Waveguide Remote Sensing (OAWRS)

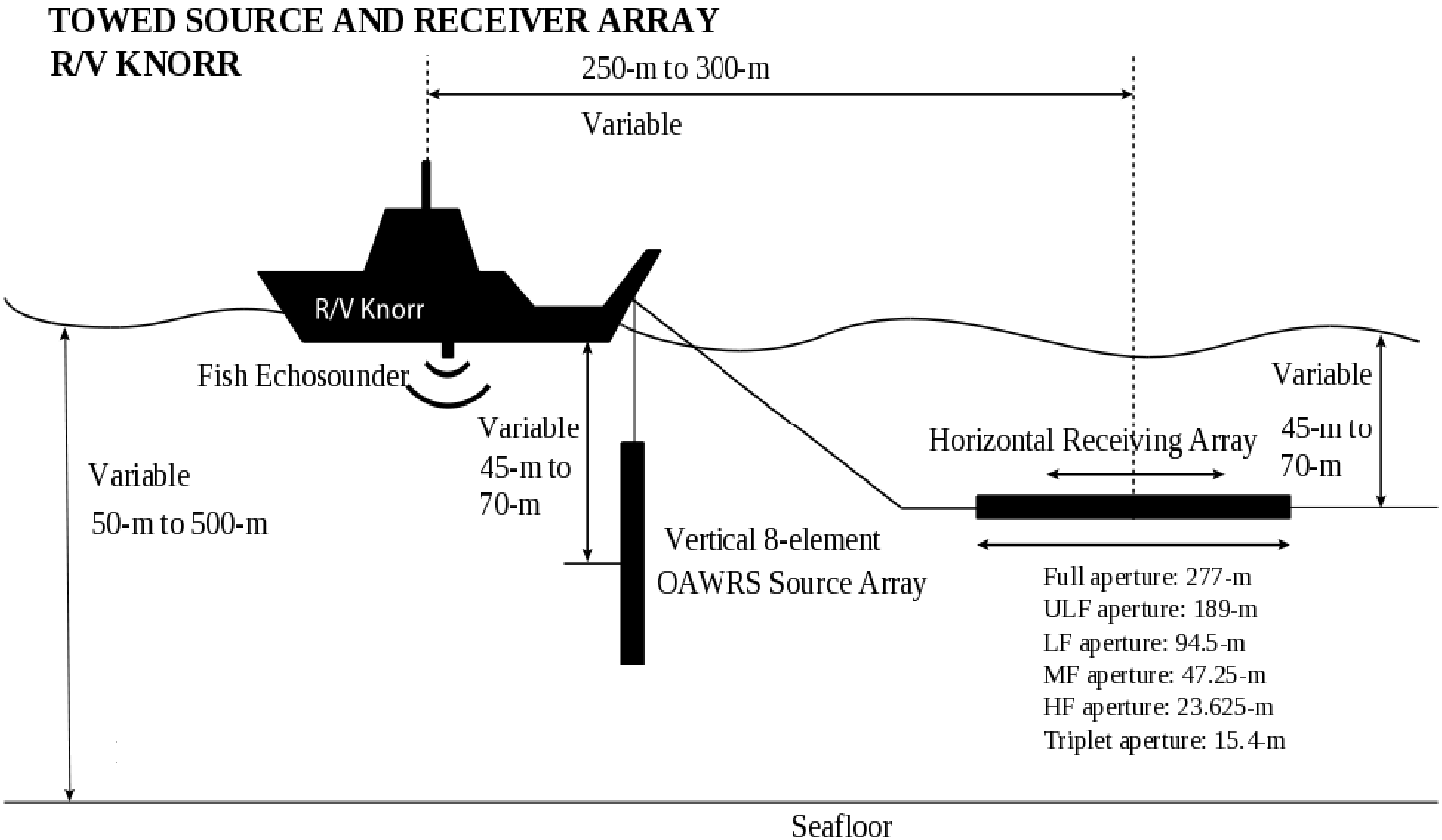

OAWRS Source Array and Receiver Array during Nordic Seas Experiment in Feb-Mar 2014 on the Stern of R/V Knorr

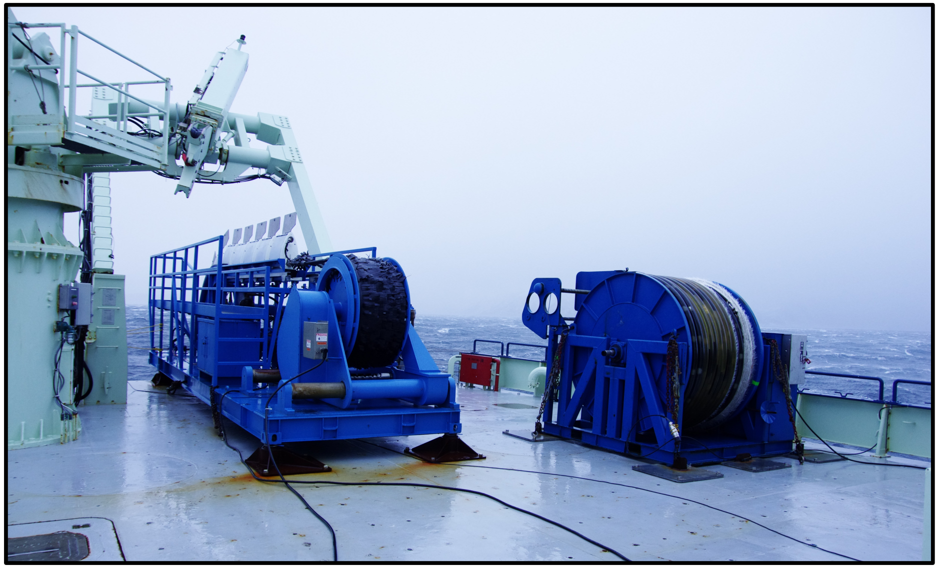

OAWRS Source Array

- First towable and portable low frequency source array. First use at sea: Nordic Seas Experiment 2014.

Ecosystem-scale Remote Species Classification with OAWRS System

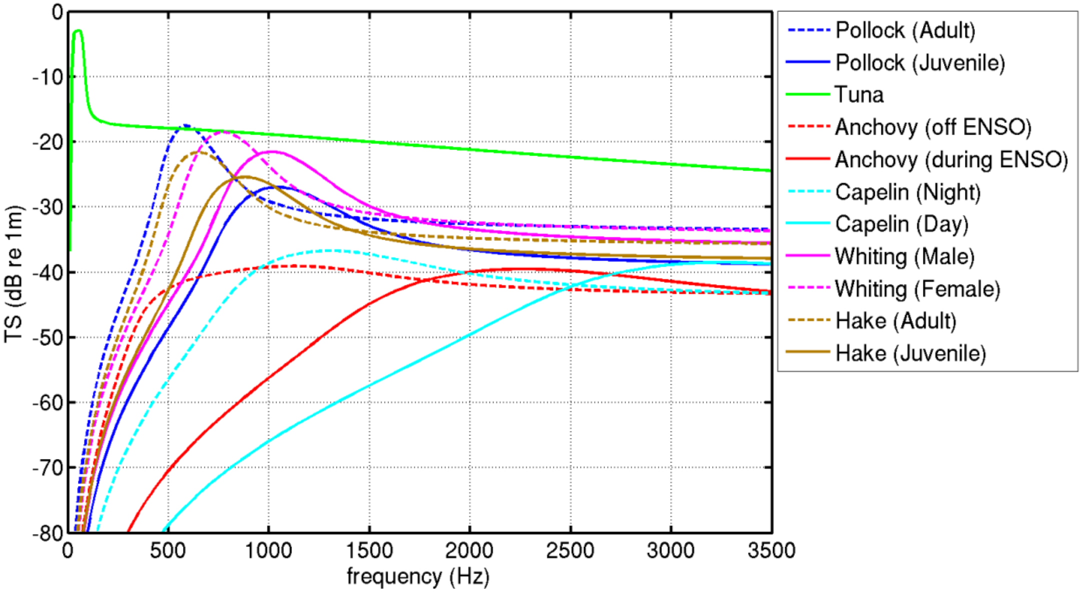

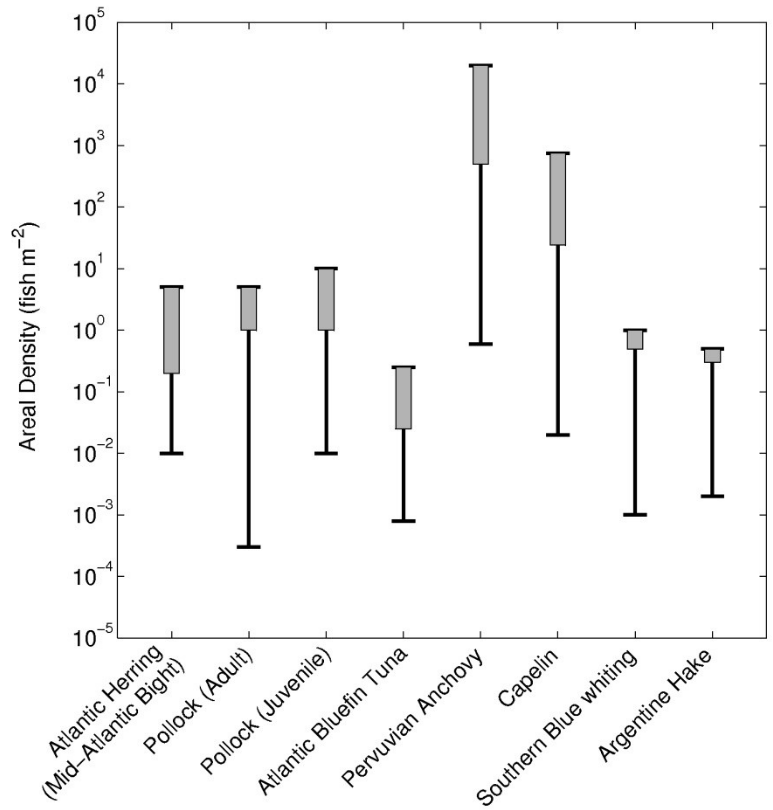

- Target strength of swimbladder bearing fish varies significantly across species at low- to mid-frequency range, which makes remote species classification possible with OAWRS's simultaneous multi-frequency survey approach.
- Large Dynamic range of population density expected in wide-area survey for 8 fish species. For typical shoaling densities (gray bars), all fish species are detectable by OAWRS system.

S. Jagannathan, I. Bertsatos, D. Symonds, T. Chen, H. T. Nia, A. D. Jain, M. Andrews, Z. Gong, R. Nero, L. Ngor, M. Jech, O. R. Godo, S. Lee, P. Ratilal, N. C. Makris, "Ocean Acoustic Waveguide Remote Sensing (OAWRS) of Marine Ecosystem",MEPS, 395,137-160 (2009)


UT 731 CD
FAR SIGMA
KNORR


ARTUS
PARKERING
FORAN
CONTAINEREN
FORBUDT
715
RESTAVFALL


JOHAN HJORT
BERGEN

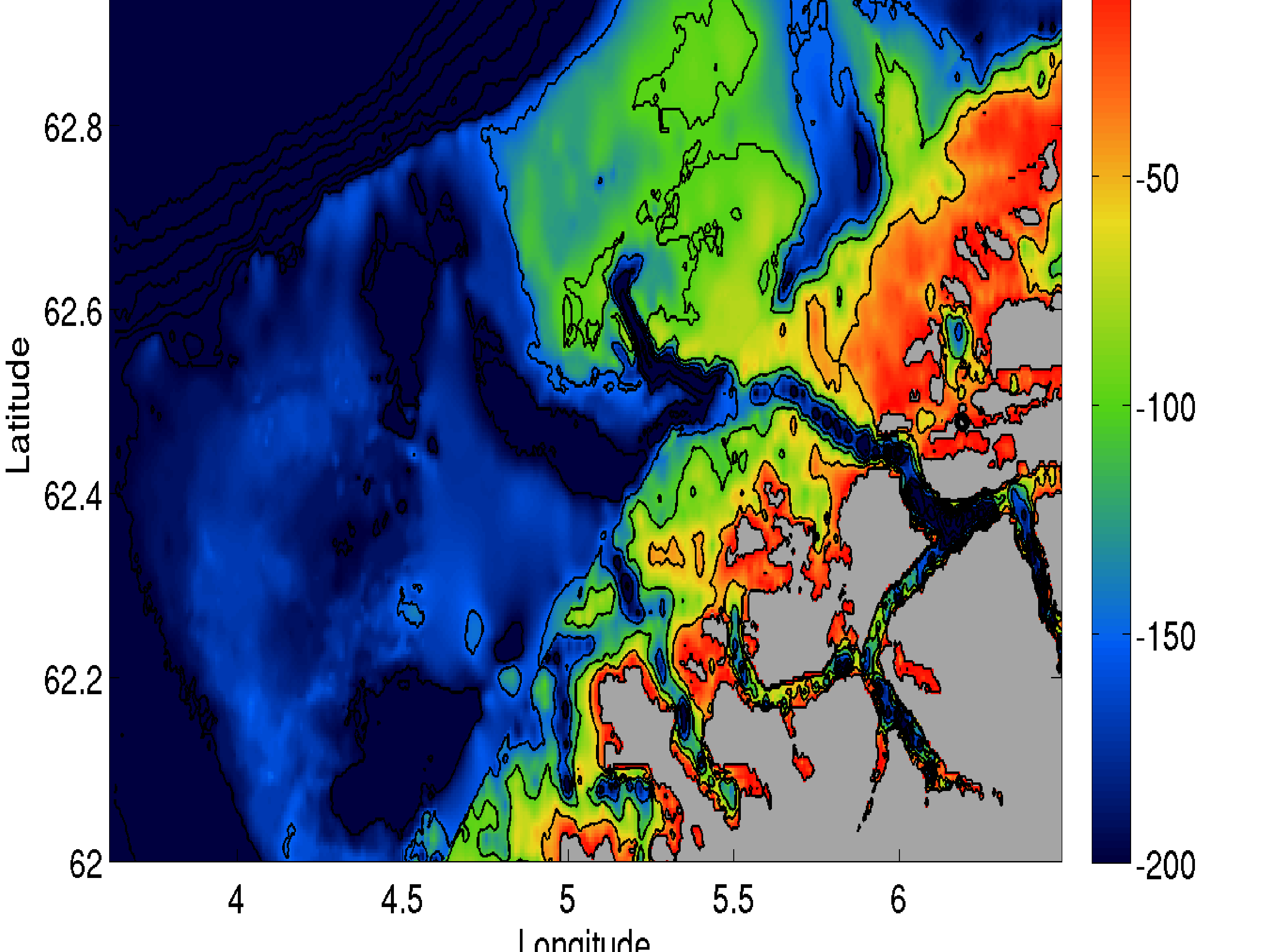

62.8
62.6
62.4
62.2
62
Latitude
4
4.5
5
5.5
6
Longitude
-50
-100
-150
-200

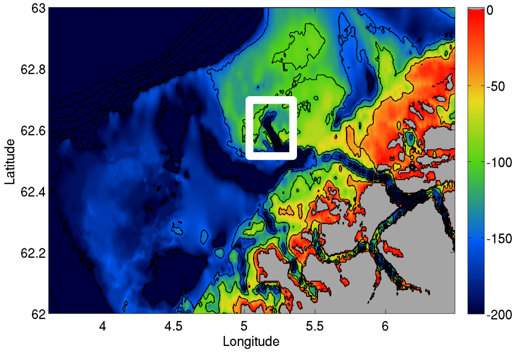

Instantaneously Imaged Gigantic Herring Shoal

Alesund Region, Feb 20 2014, 23:50 UTC

Areal Population Density (fish/m²)

Scattering Strength (dB)

Sound Pressure Level (dB re 1 μPa)

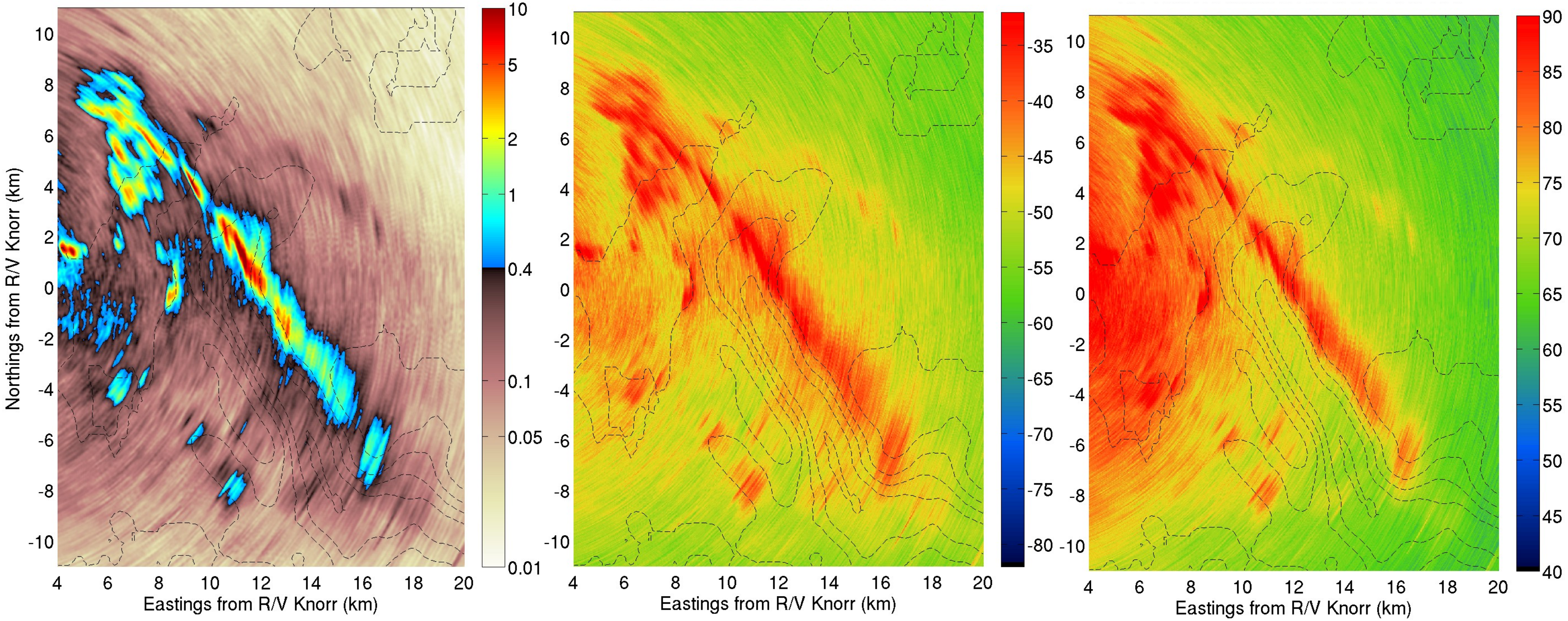

Excellent Correspondence Between Instantaneous Eulerian OAWRS Imagery of Herring Shoals and Lagrangian Particle Echograms along Fishing Vessel Artus Track

Instantaneous wide-area OAWRS images taken from R/V Knorr

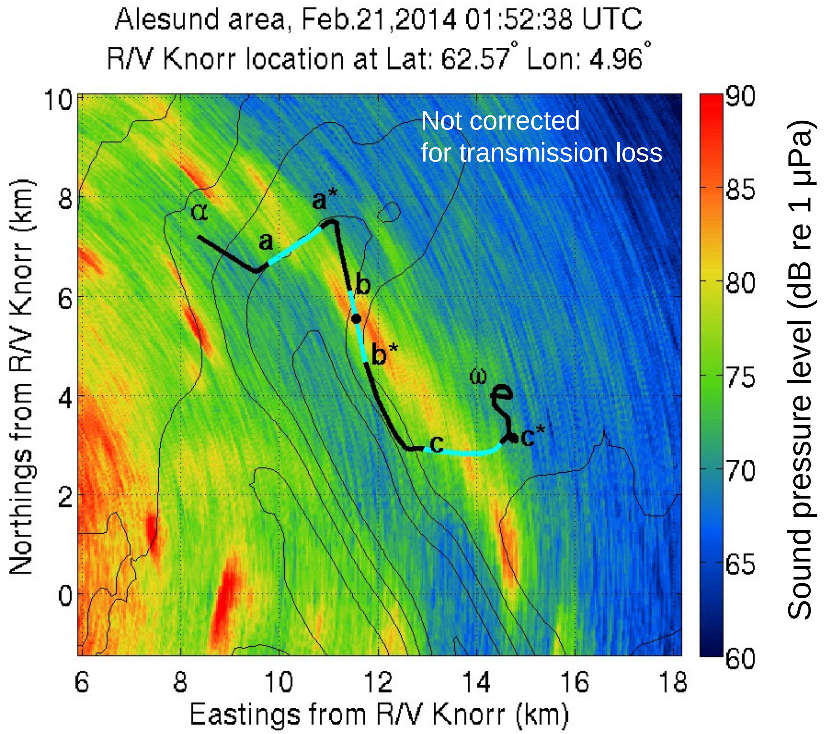

Range-depth echogram along Artus track

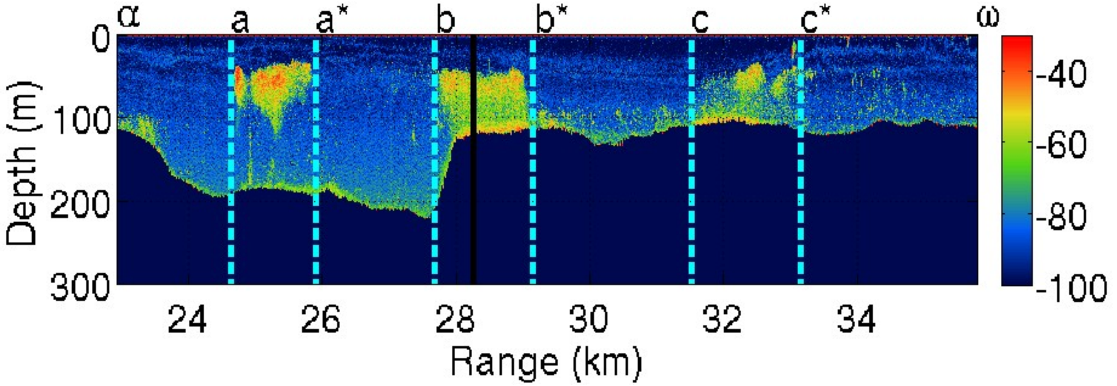

Norrkapp (Mike Collins NRL)

Cod and Capelin at Norrkapp

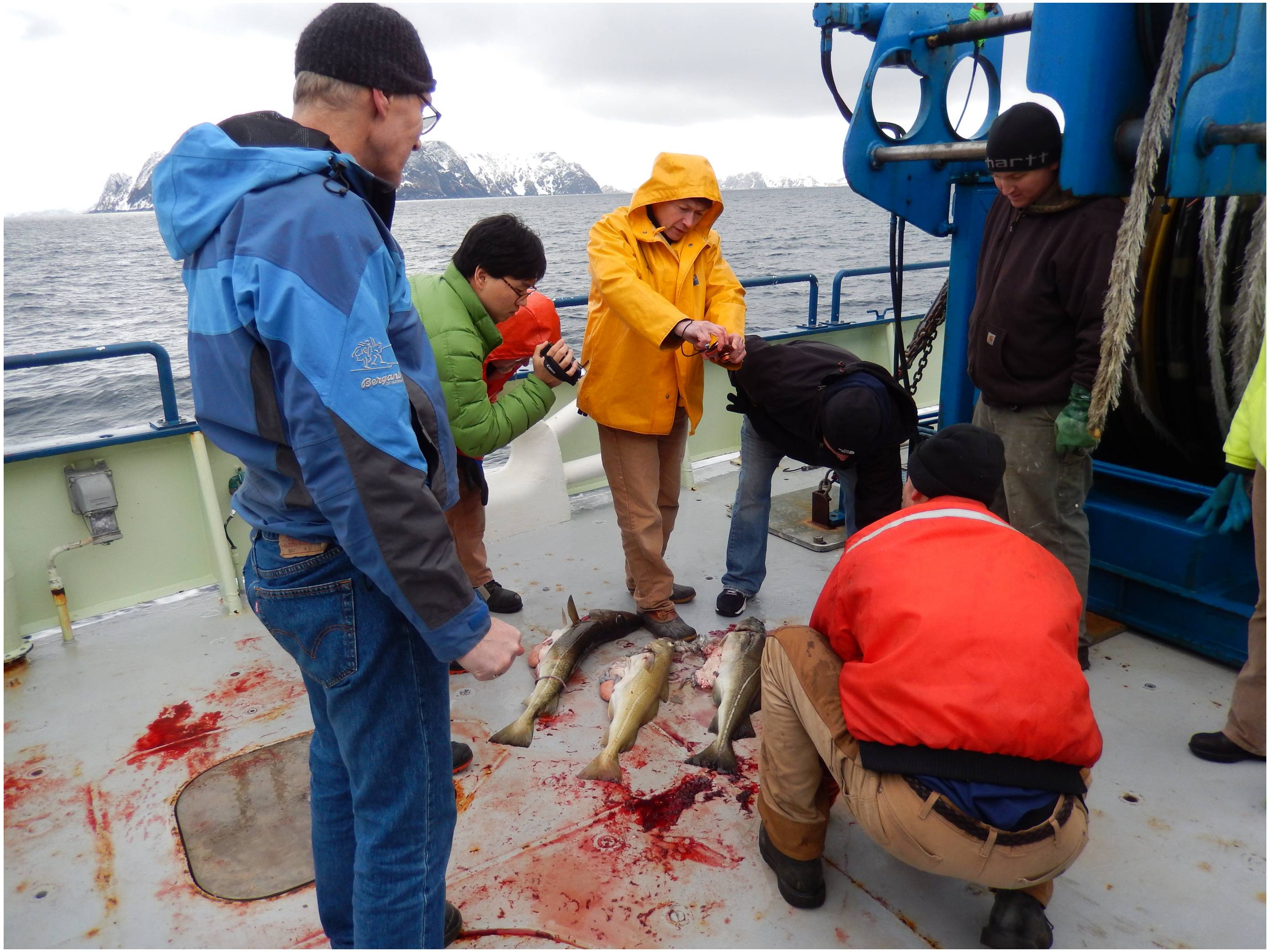

3/27/18

Cod and Capelin at Norkapp

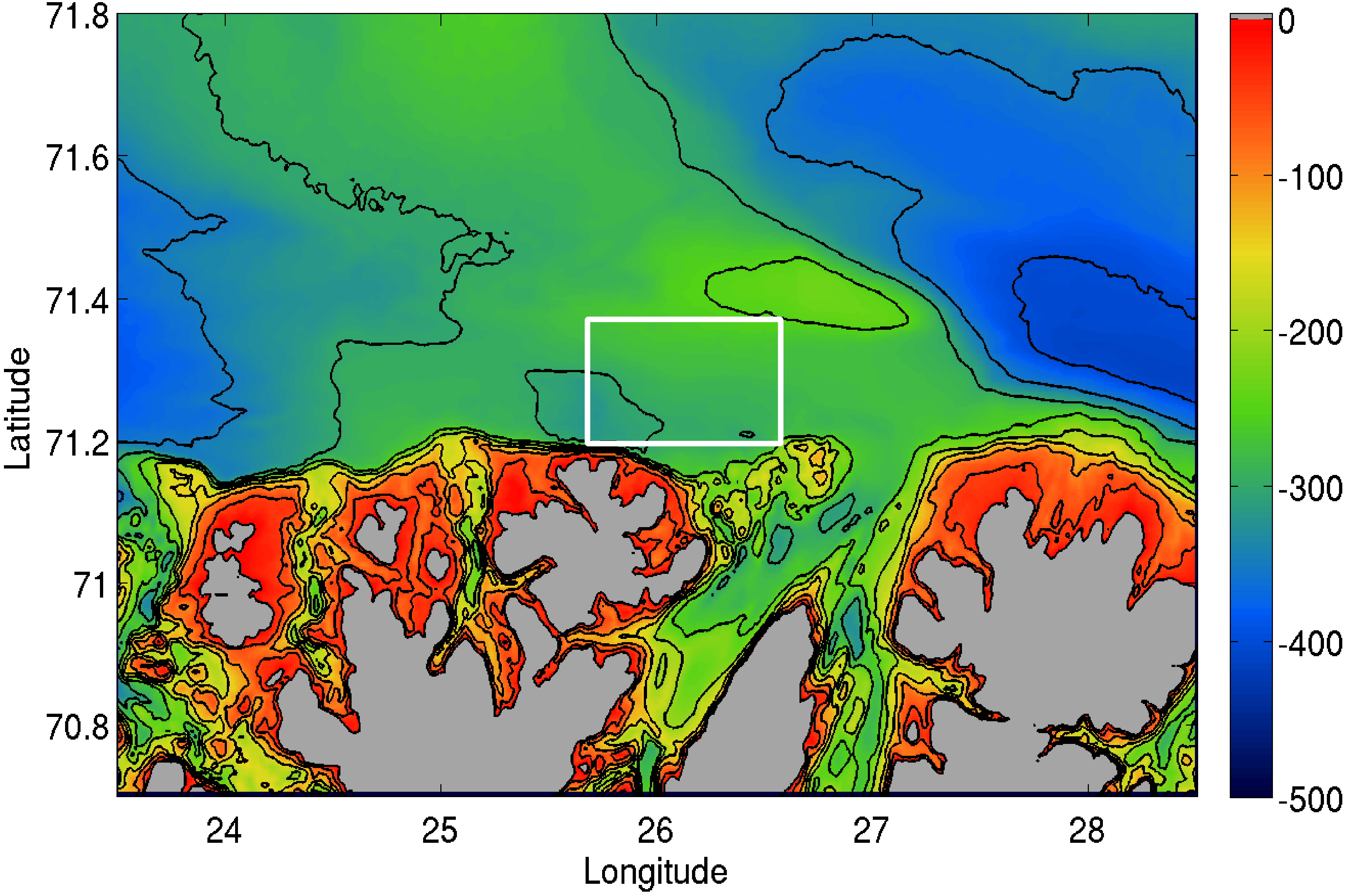
71.8
71.6
71.4
71.2
71
70.8
Latitude
24
25
26
27
28
Longitude
0
-100
-200
-300
-400
-500

March 4 Cod/Capelin Shoals Correspondence

OAWRS image at 05:52 UTC with R/V Johan Hjort tracks

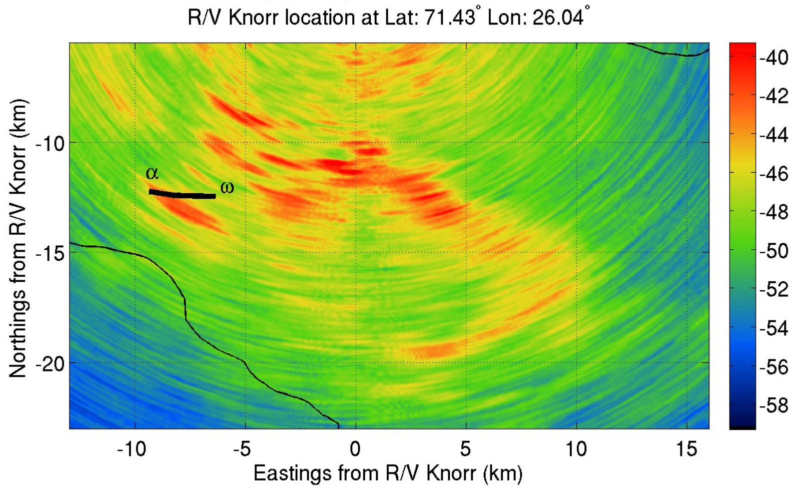

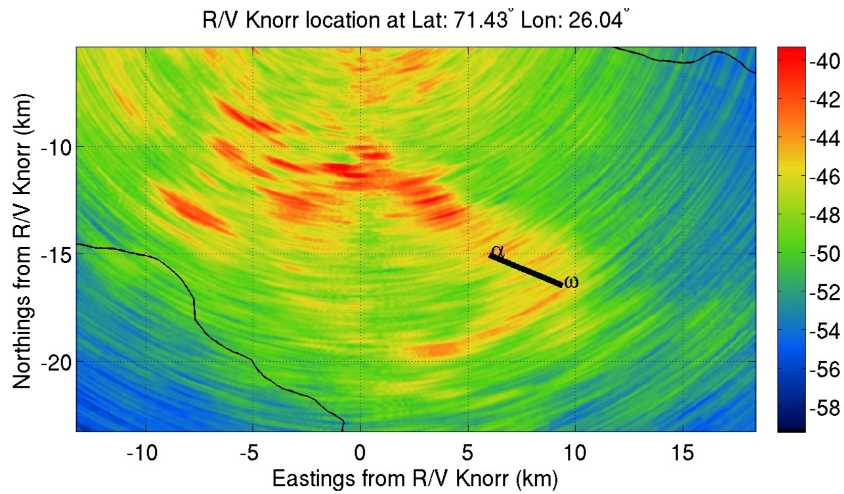

Corresponding R/V Johan Hjort Echograms showing both capelin and cod aggregations

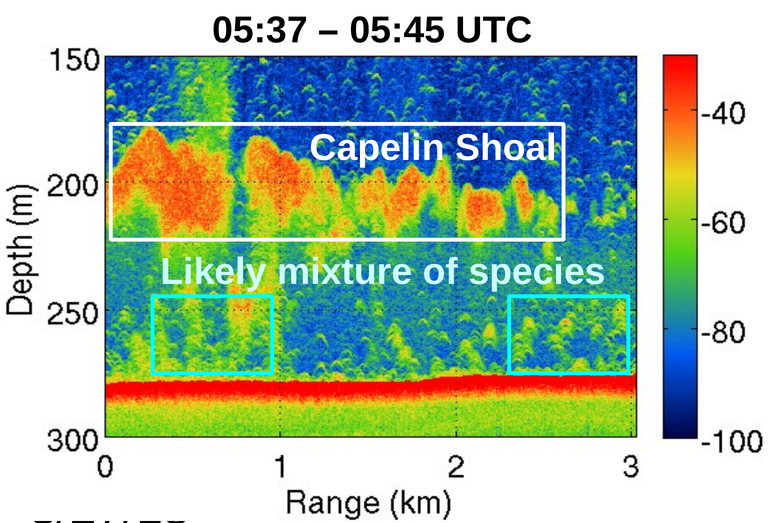

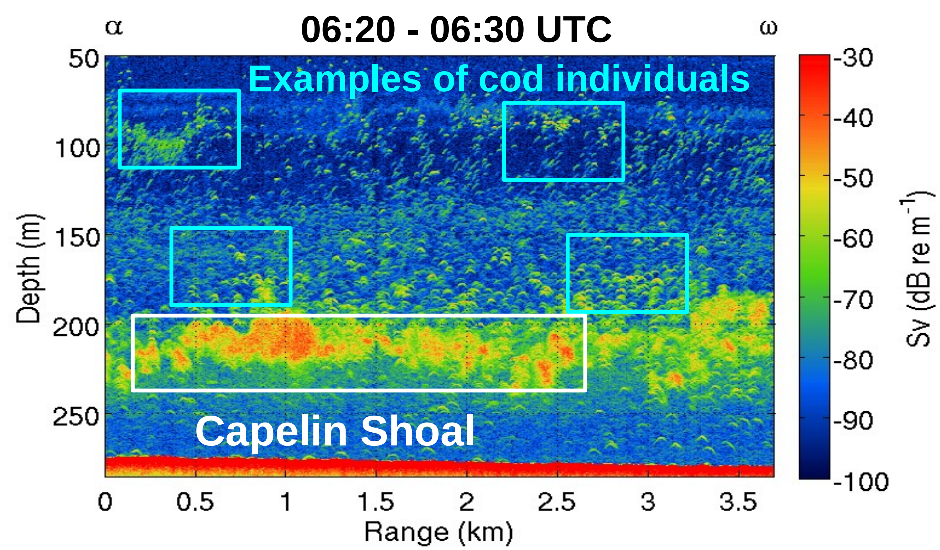

Instantaneously Imaged Gigantic Capelin Shoal

Finnmark Region, Feb 27 2014, 04:45 UTC

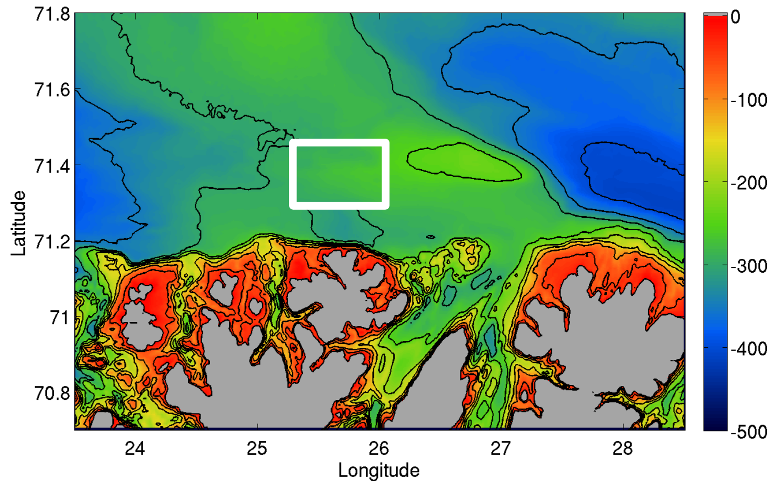

Areal Population Density (fish/m²)

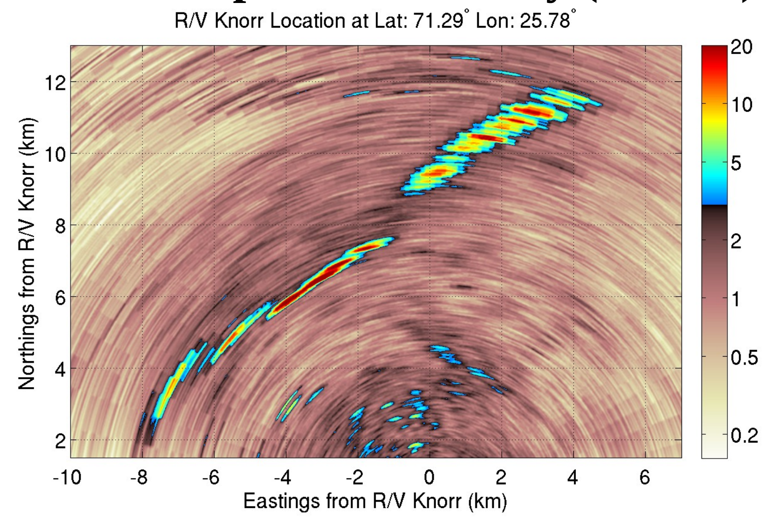

Scattering Strength (dB)

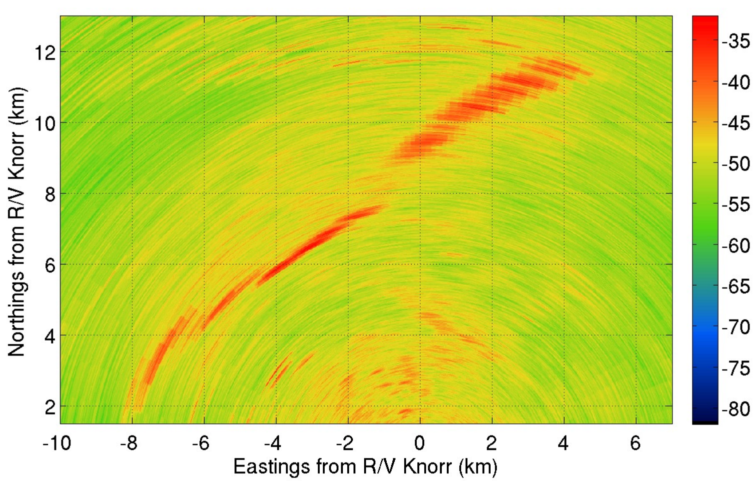

Sound Pressure Level (dB re 1 μPa)

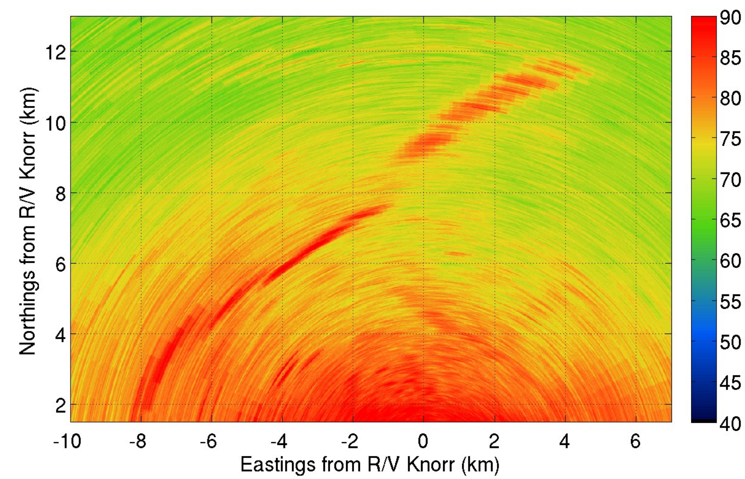

Instantaneous Imaging of Large Capelin Shoals in Finnmark area

Instantaneous wide-area OAWRS image taken from R/V Knorr at 04:45 UTC

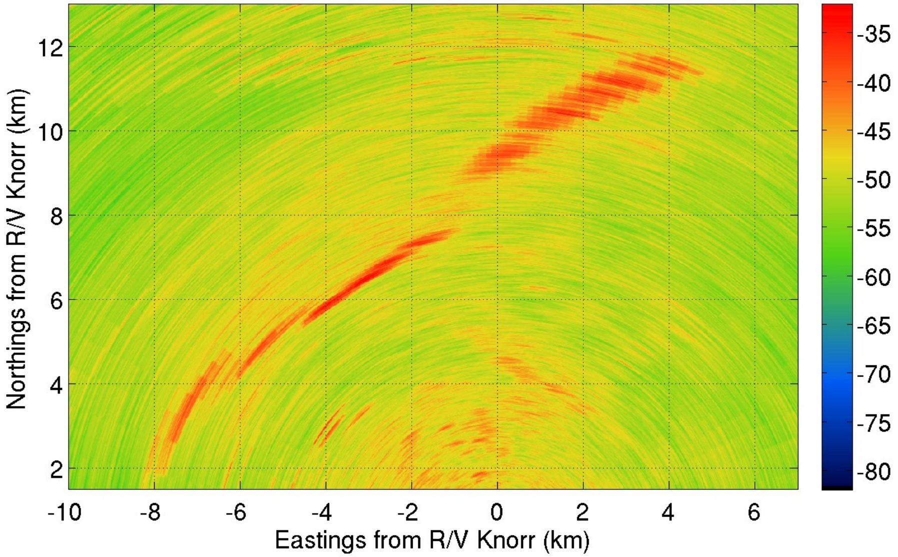

Capelin shoal confirmed by **R/V Knorr**'s downward directed echosounder, ship turned to cross shoal found by OAWRS between 03:10 – 03:45 UTC

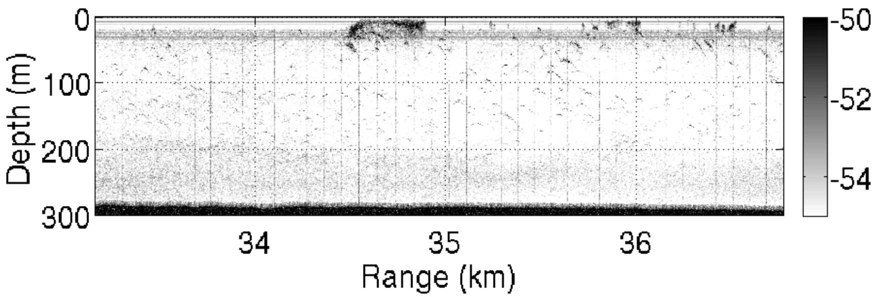

Lofoten Andenes

“A Descent into the Maelstrom”

Location of Large Cod and Haddock Shoals Imaged in Lofoten Area near Andenes using OAWRS

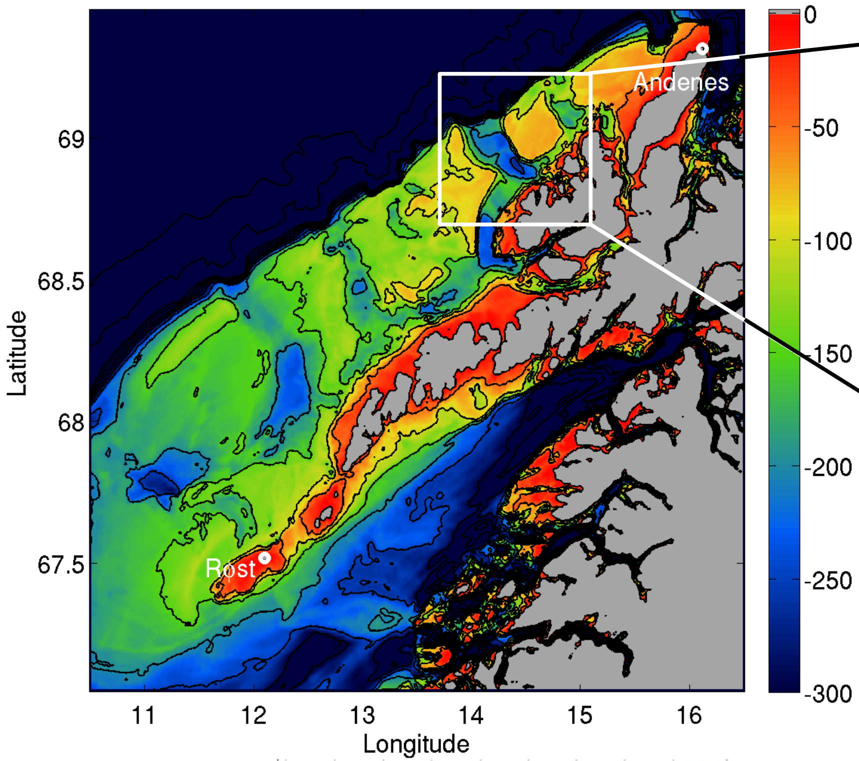

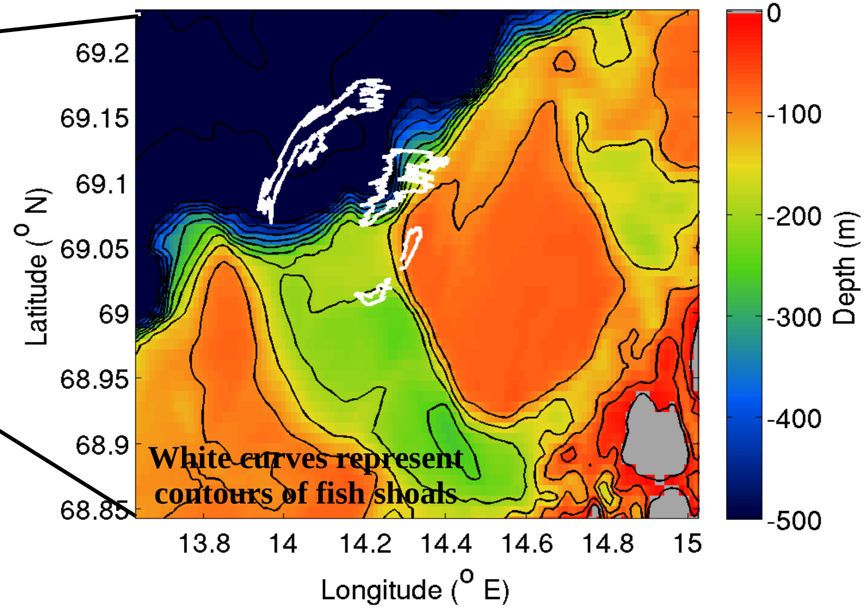

Historical Cod Hotspots

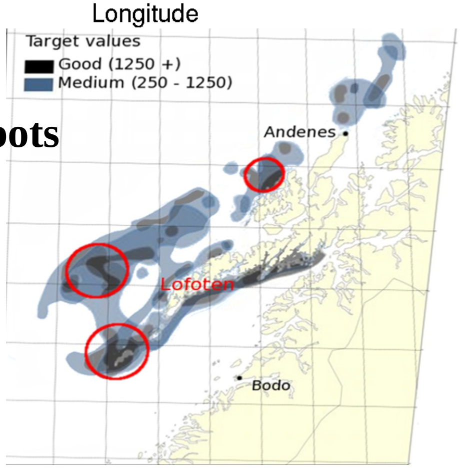

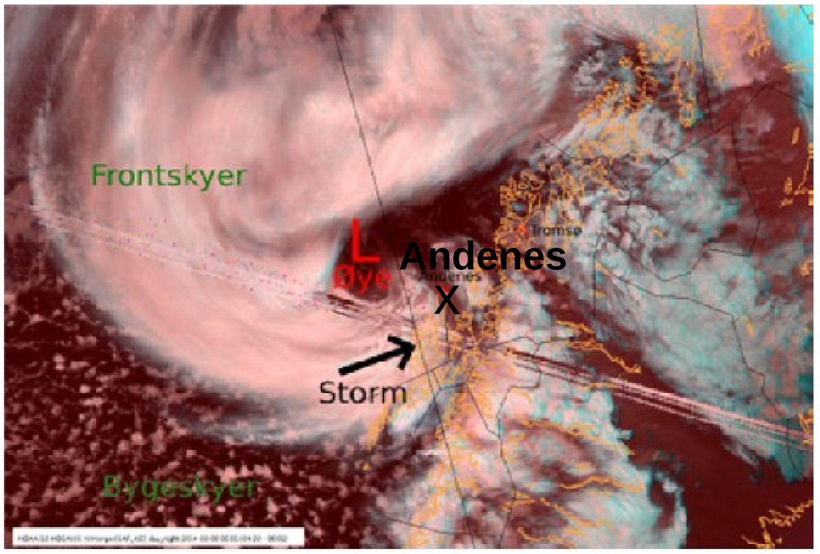


EXIT
NIOZ
TEXEL
sun'n'fun
gimme!
coffee
sticky
bumps

Instantaneously Imaged Gigantic Cod Shoals

March 8 00:16:49 UTC

Current crude estimate: 1 million cod individuals (> 0.02 fish/m^2)

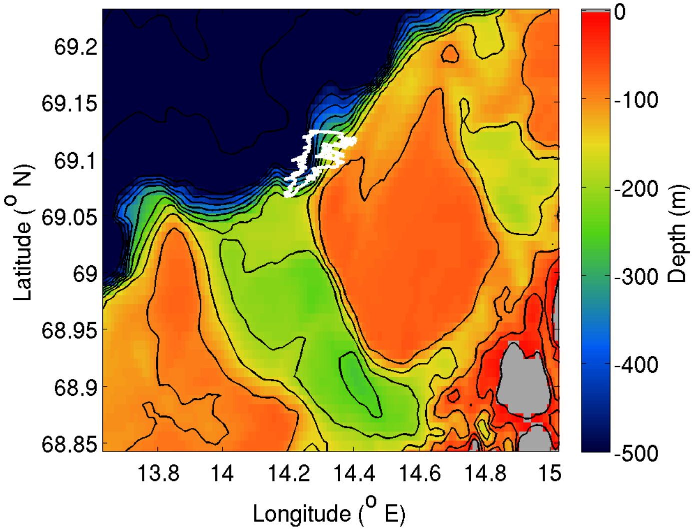

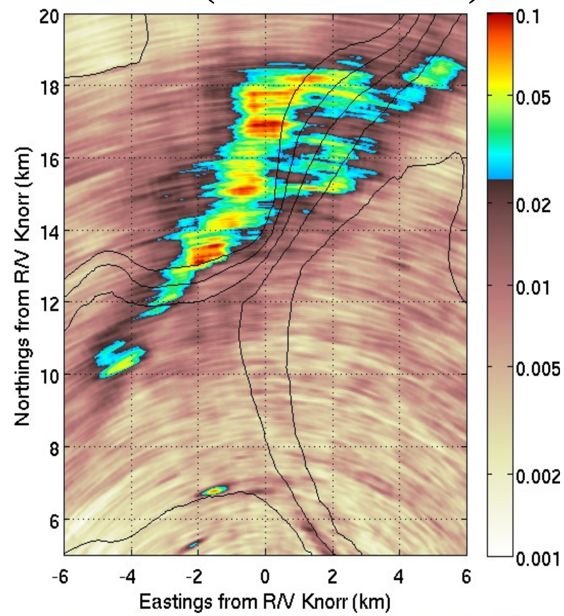

Areal population density (fish/m^2)

Scattering strength (dB)

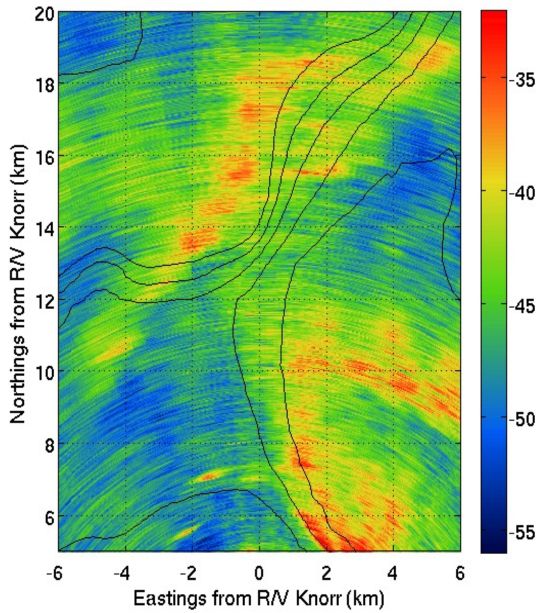

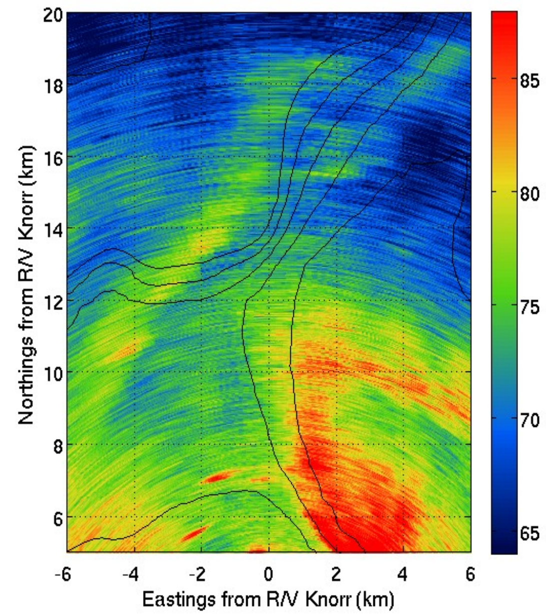

Sound pressure level (dB re 1 μPa)

3/27/18

Instantaneous Imaging of Large Cod Shoals in Lofoten Area near Andenes, March 8

Instantaneous wide-area OAWRS image taken from R/V Knorr at 00:16 UTC

Areal population density (fish/m^2)

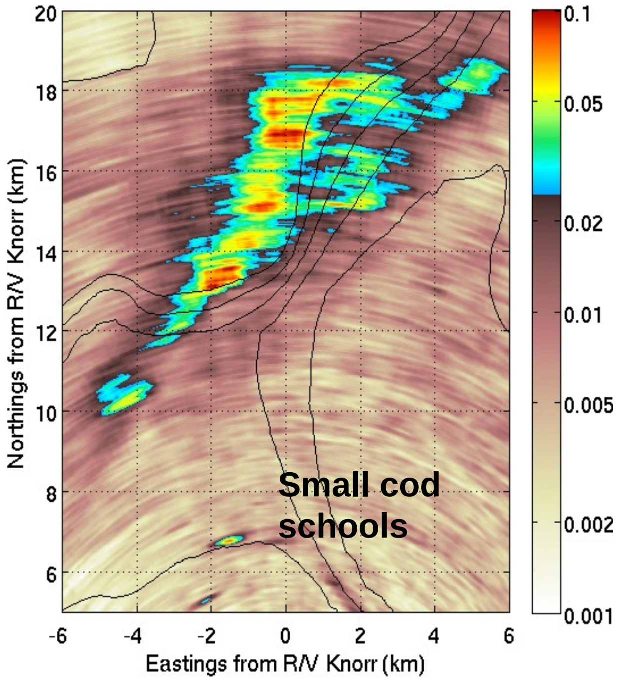

Cod shoal confirmed by **R/V Knorr**'s downward directed echosounder as the ship crossed over the shoal between 01:15 – 02:25 UTC

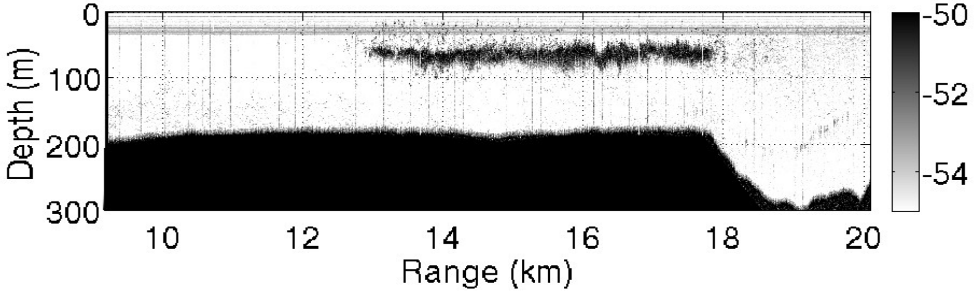

Cod shoal again confirmed by **R/V Johan Hjort**'s downward directed echosounder between 02:35 – 03:00 UTC

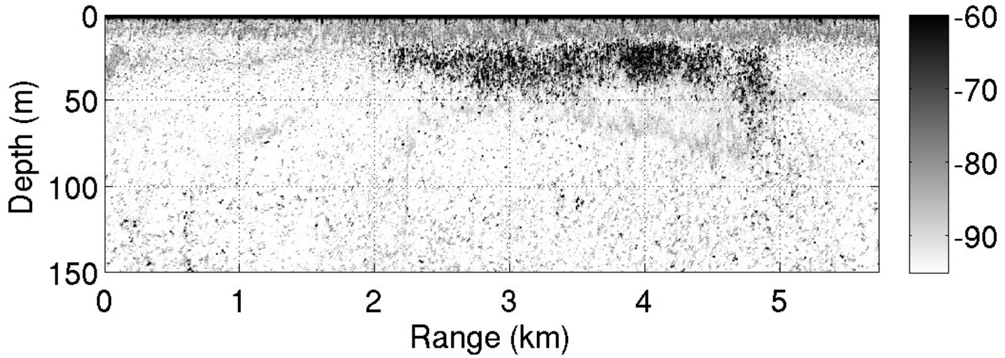

Large cod shoal (> 10 km) imaged by OAWRS for the first time. R/V Knorr turned to cross location of OAWRS returns confirming fish with ship's echosounder. Later R/V Johan Hjort arrived from the North and also confirmed the OAWRS returns were from a large cod shoal. All ships had to flee area immediately afterwards at coast guard request due to hurricane conditions.

Instantaneously Imaged Gigantic Haddock Shoals

March 5 23:43:49 UTC

Current crude estimate: 1.4 million haddock individuals (> 0.02 fish/m^2)

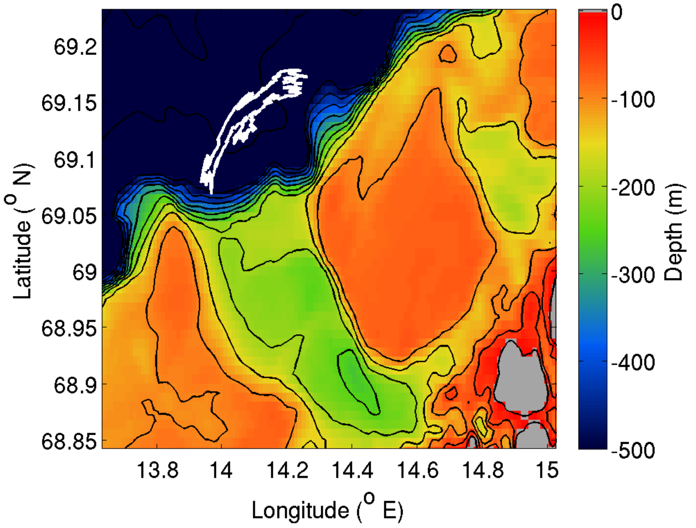

Areal population density (fish/m^2)

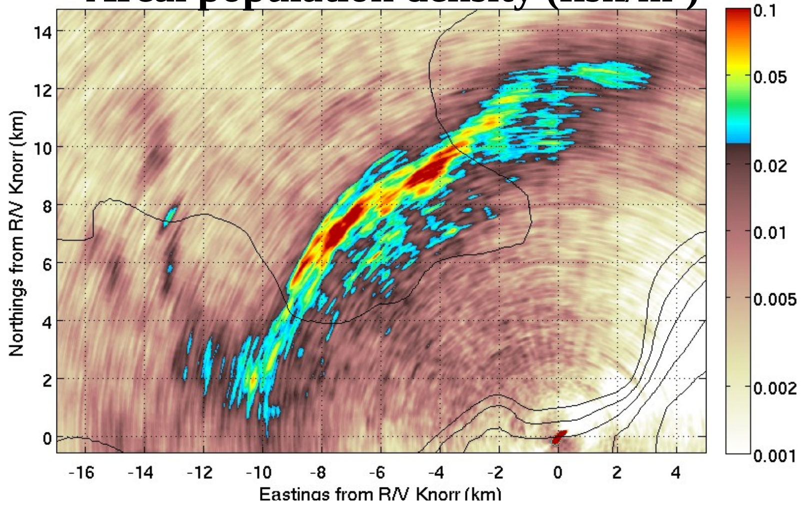

Scattering strength (dB)

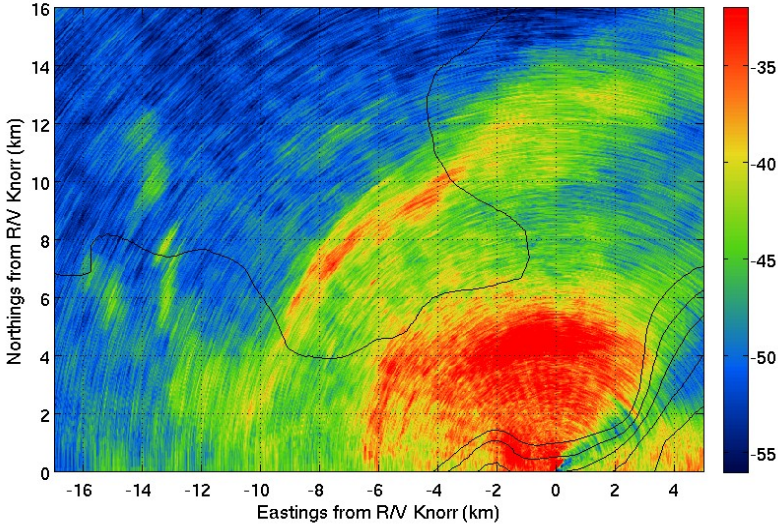

Sound pressure level (dB re 1 μPa)

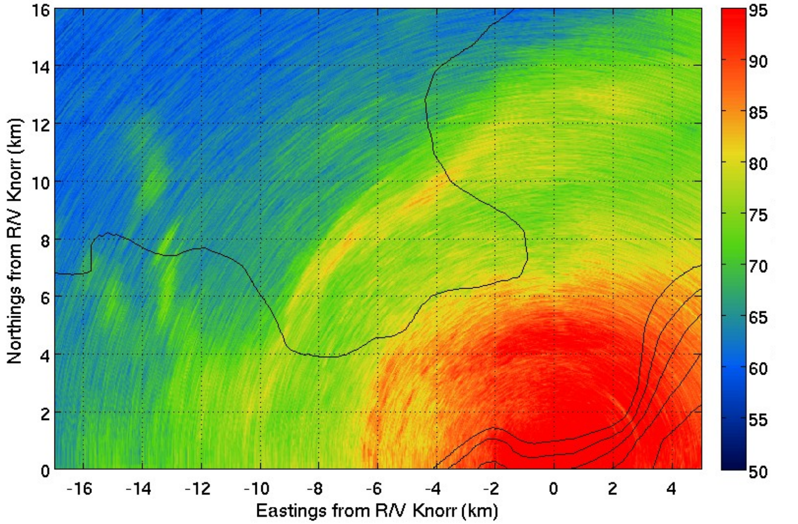

'This "little cliff" arose, a sheer unobstructed precipice of black shining rock, some fifteen or sixteen hundred feet from the world of crags beneath us'   A Descent into the Maelstrom

Lofeten, Rolst

Bounded Gigantic Shoals of Spawning Cod Imaged by OAWRS in Lofoten, Norway

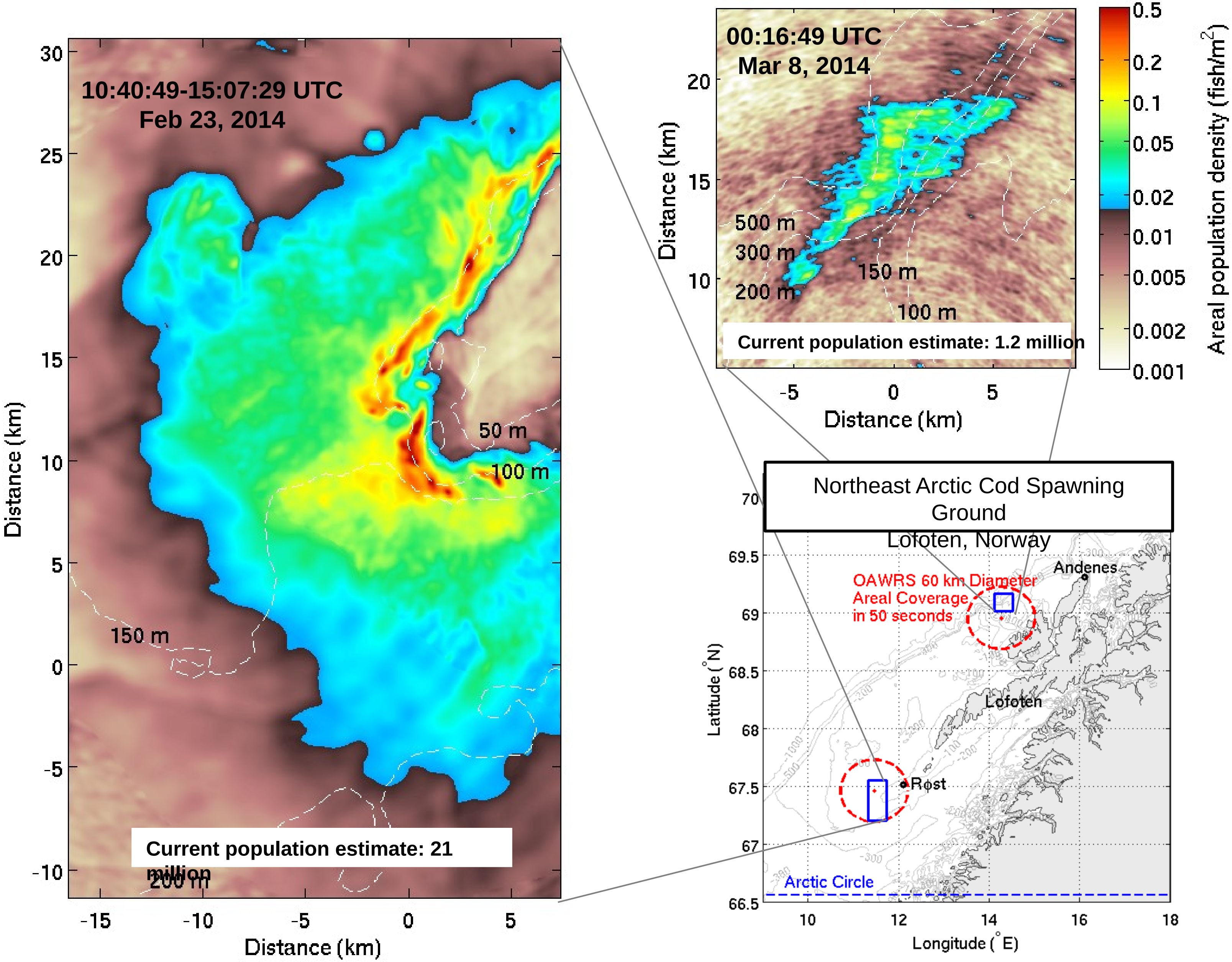

Lofoten Rolst

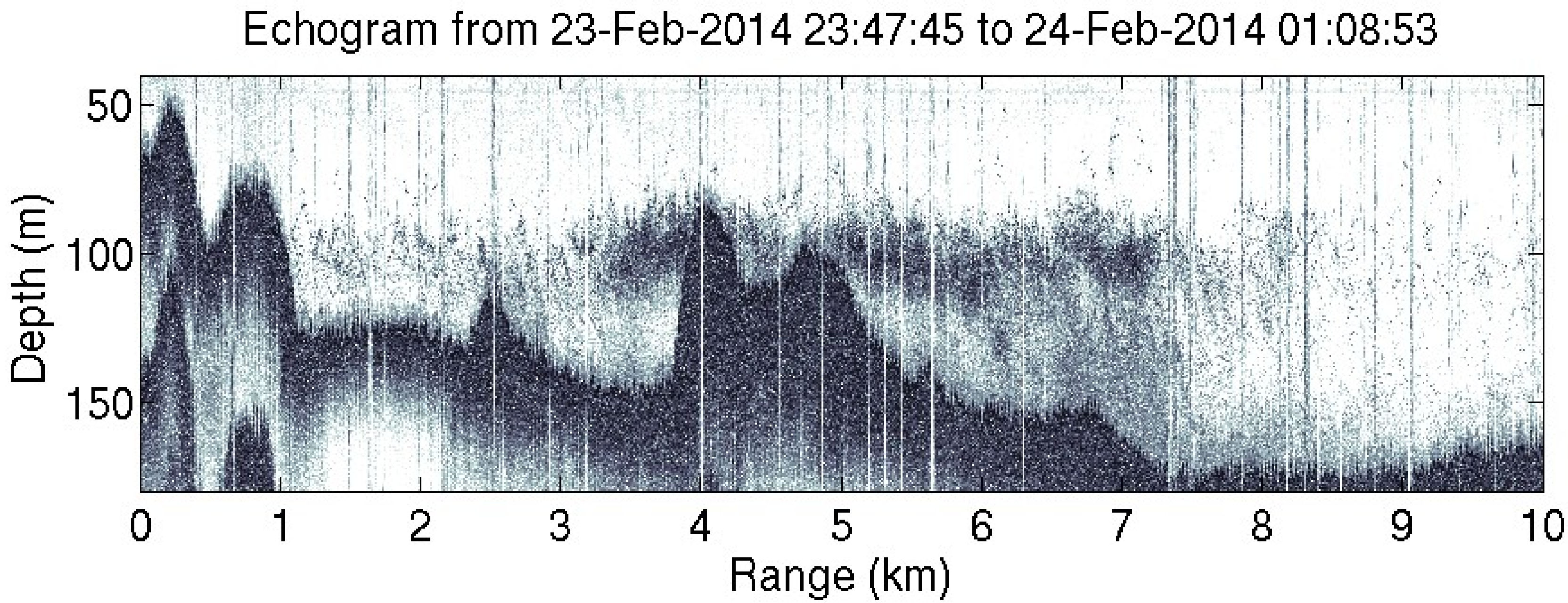

Lofoten Andenes

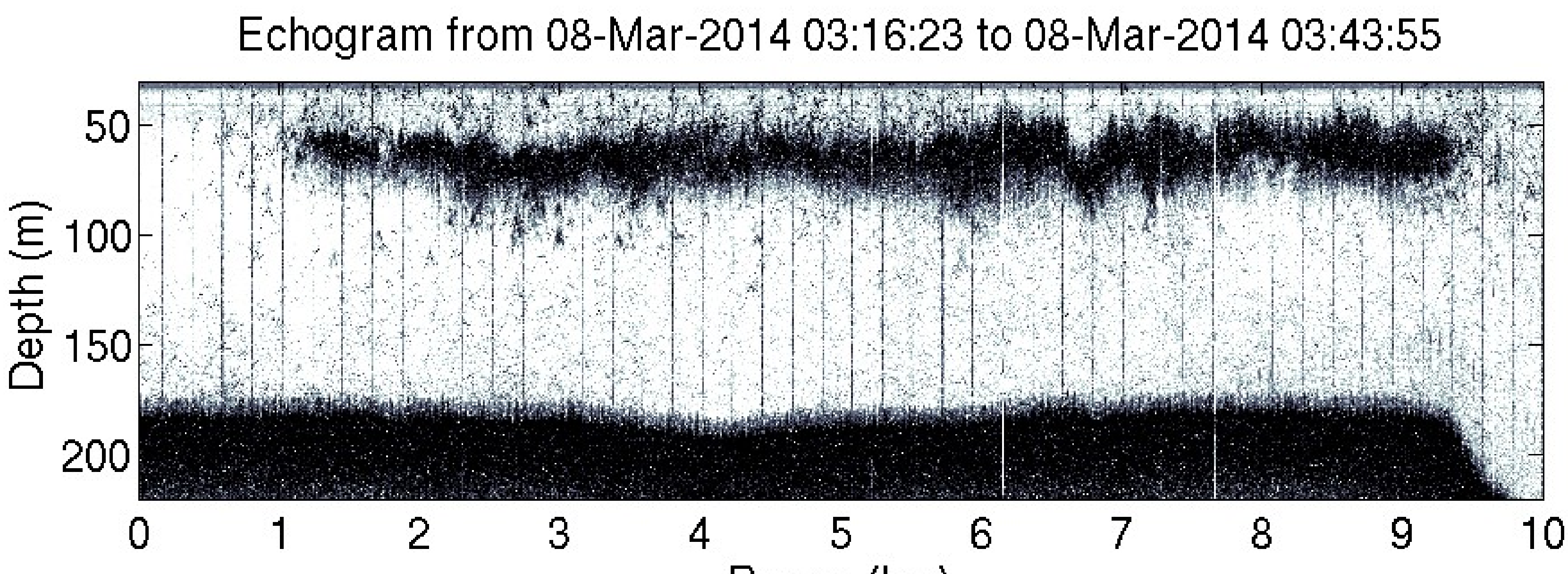

Consistency between OAWRS imaging and vertical echosounder measurement

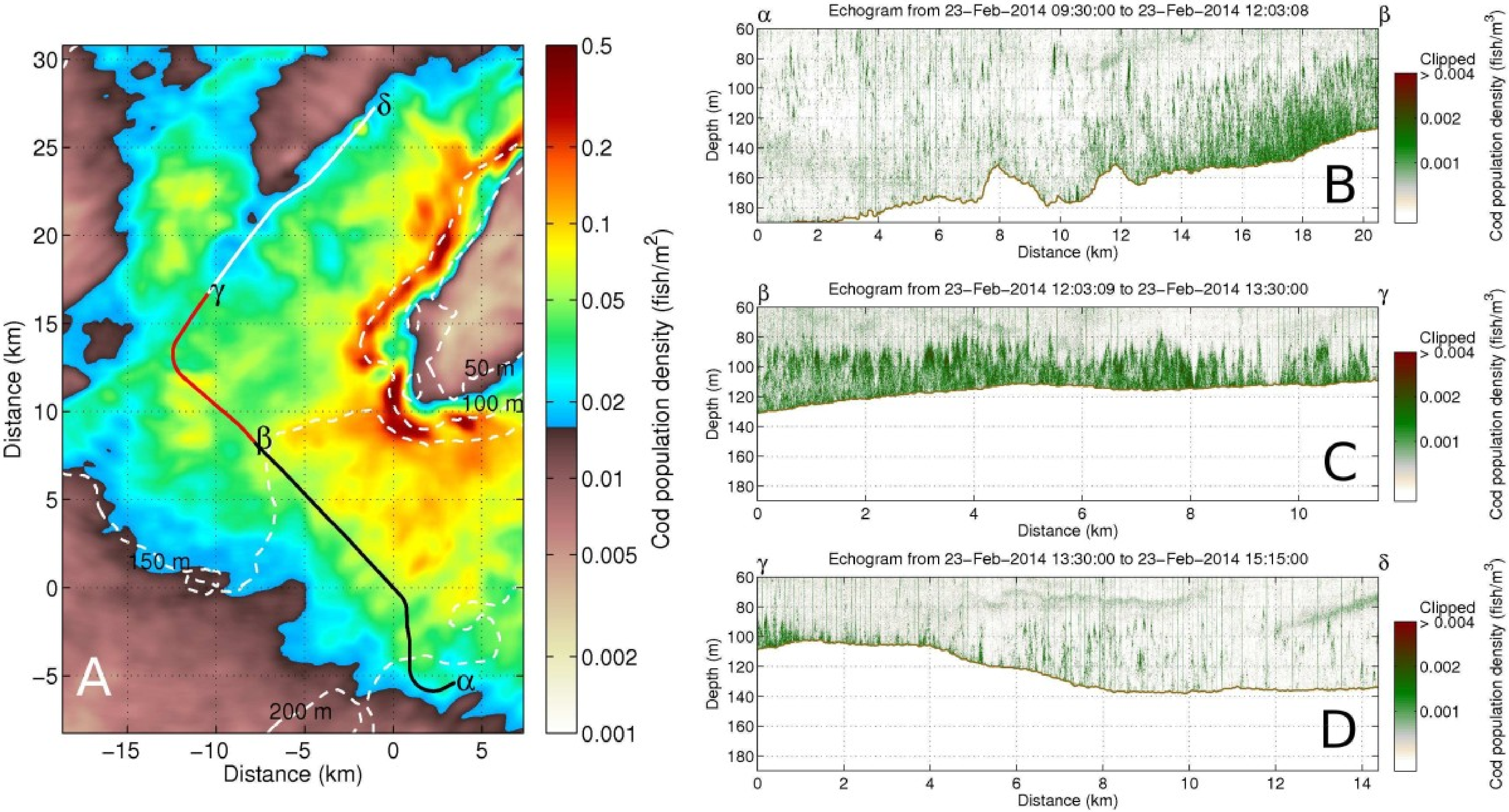

Consistency between OAWRS imaging and vertical echosounder measurement

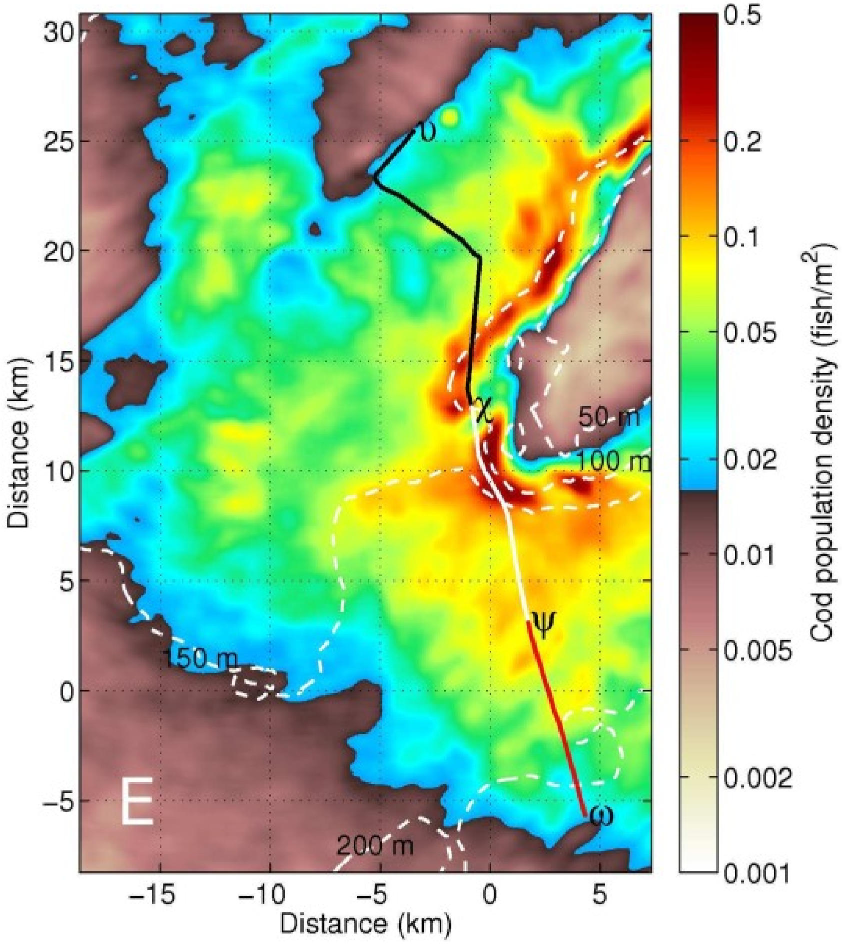

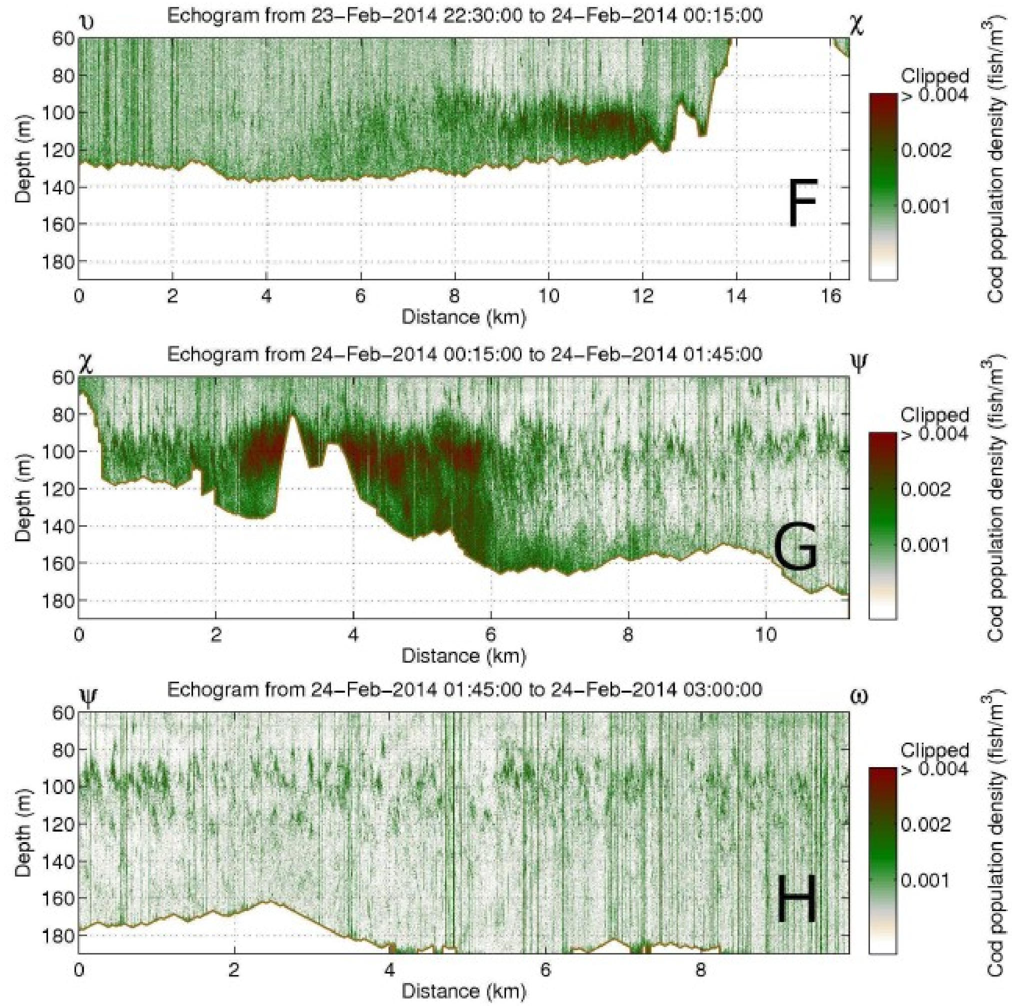

Consistency between OAWRS imaging and vertical echosounder measurement

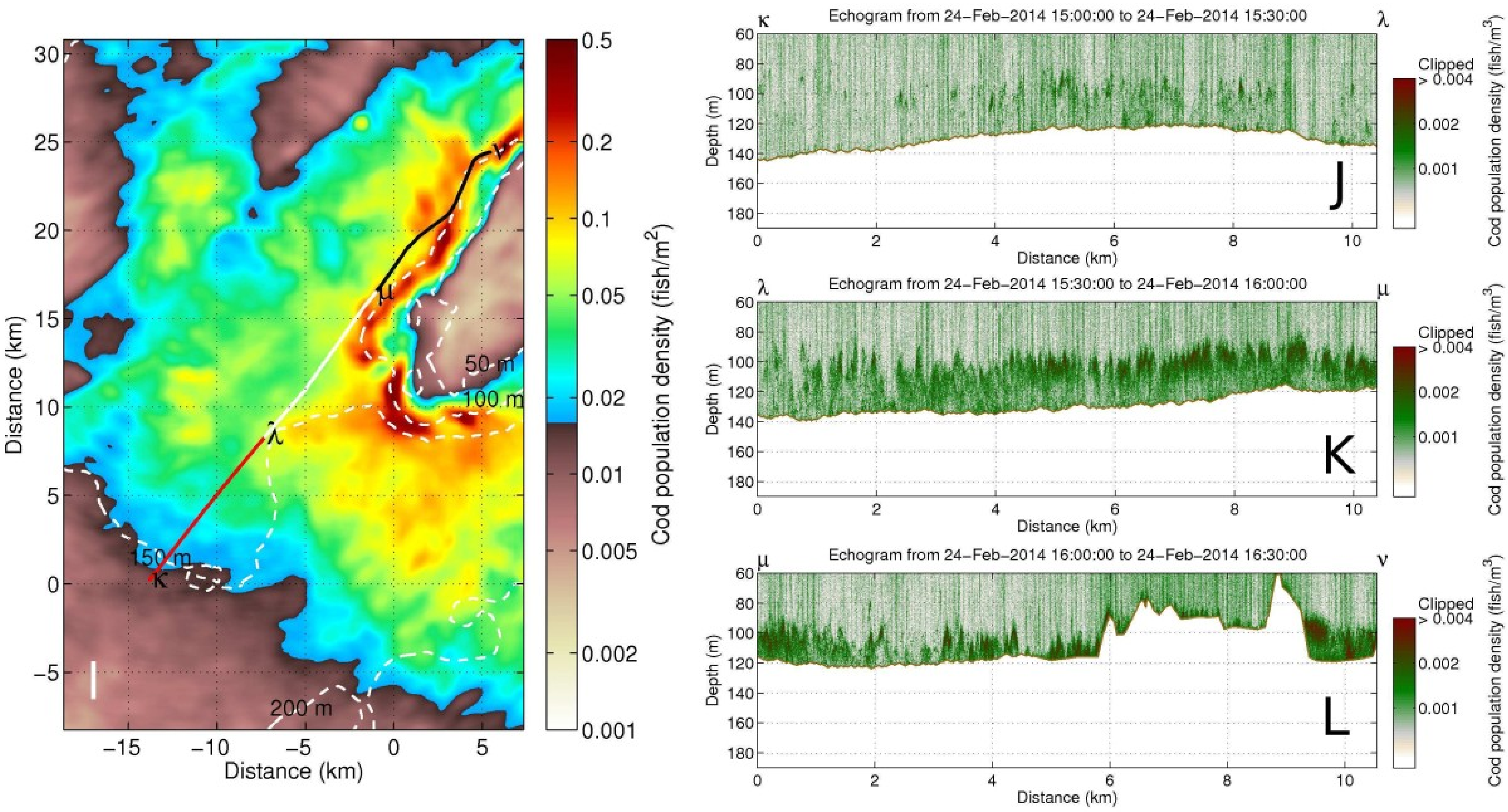

TORSKEPRIS 2014 –2015

Gjennomsnitt NRL 2014-2015 u/15 m

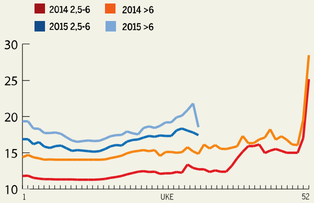

GJENNOMSNITTLIG PRIS ALLE SONER

Pris gjelder største størrelse

	Torsk >6 pris (SUH)	Torsk 2,5-6 pris (SUH)	Hyse pris (SUH)	Sei pris(SUH)
Øst-Finnmark	19,77	18,61	13,67	0
Vest-Finnmark	24,00	19,77	12,98	10,92
Troms	16,33	15,68	12,64	10,66
Vesterålen	17,05	15,99	14,81	11
Lofoten	18,69	18,36	11,33	11,12
Øvrig Nordland	16,25	16,07	14,14	11,82
Trøndelag&Nordmøre	16,74	15	10,98	11,1
Totalt	21,87	17,84	13,09	10,79

Kvantum torsk, hyse og sei

Tonn

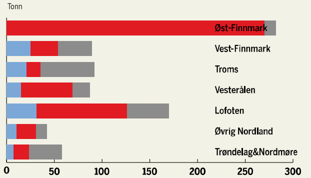

LEVERT KVANTUM I TONN

fartøy under 15 meter

	Torsk	Hyse	Sei	Totalt
Øst-Finnmark	37	136	6	179
Vest-Finnmark	20	11	15	46
Troms	10	10	163	183
Vesterålen	8	62	14	85
Lofoten	18	93	19	130
Øvrig Nordland	5	16	4	25
Trøndelag&Nordmøre	7	13	31	50
Total	106	340	252	698

ANTALL FARTØY

under 15 meter i fiske

	Antall Fartøy	Fangstrater i tonn
Øst-Finnmark	53	3,38
Vest-Finnmark	26	1,77
Troms	50	3,66
Vesterålen	45	1,87
Lofoten	55	2,36
Øvrig Nordland	21	1,19
Trøndelag&Nordmøre	70	0,73
Total	320	

FANGST PER REDSKAPSGRUPPE

Tonn

	Torsk	Hyse	Sei	Totalt
Autoline	33	43	2	78
Garn	18	15	48	82
Juksa	11	1	48	60
Line	29	188	6	224
Not	0	0	145	145
Snurrevad	14	93	3	110
Teiner	0	0	0	1
Totalt	106	340	252	698

Kilde: Norges Råfisklag

SAMARBEIDER: Nicholas Markis (t.h) og Olav Rune Gode samarbeider om utvikling av en sonar som kan se 40 kilomer fra båten. Her sammen med Gavin Macaulay (i midten) på tokt utenfor USAs østkyst.
ALLE FOTO: MASSACHUSETTS INSTITUTE OF TECHNOLOGY (MIT)

Ny sonar kan revolusjonere fiskeletingen

FORSKNING

Havforskere har tatt i bruk ny sonarteknologi som kan se fisk opp til 40 kilometer fra båten. – Revolusjonerende, mener fiskerne.

Det er den amerikanske havforskeren og professoren Nicholas Makris ved Massachusetts institute of technology (MIT) som har vært i Norge og samarbeidet med Olav Runde Godø i havforskningsinstituttet i videreutviklingen av sonaren for bruk i fiskeleiting.

Potensial

Sonaren er utviklet både for militære formål og for forskning, men har hittil vært for dyr til å ta i kommersiell bruk. Markis anslår en kostnad på to millioner dollar for den de har brukt, men mener den kan produseres billigere dersom den settes i kommersiell produksjon.

– Teknologien har vært brukt for å finne ubåter, sier Markis som har samarbeidet med Godø nå i flere år for videreutvikling av teknologien for bestandsberegninger av fisk.

– Sonaren egner seg godt til kartlegging av gytebestander, siden den kan beregne hva som er i en stim som kan være så langt vekke som 30 - 40 kilometer, sier Godø som ser stort potensial i å bruke et slikt verktøy i bestandsberegningen.

De viser til en slik erfaring i et tokt de hadde utafor Andenes i fjor, der de fra stor avstand så en stor fiskekonsentrasjon stå i eggakanten.

– Anslagsvis kan vi dekke 90-95 prosent av gytebestandene med denne teknologien, sier Godø, men legger til at det vil ta tid å komme så langt at metoden kan erstatte eksisterende metoder. Den nye metoden må først avstemmes med de gamle metodene. Noe som er særlig viktig for å beholde tidsseriene disse har bygget opp, viser han til.

Sparer gangtid

I forskningen vil bruken av en slik sonar spare forskerne for gangtid. Den sender signaler ut i alle retninger samtidig, og dekker et langt større område. Normal rekkevidde for en sonar brukt i bestandsberegning er 1-2 kilometer. Denne når opp til 50 kilometer, men kan brukes med stor treffsikkerhet på 30-40 kilometer.

– En sonar som når ti ganger lenger, dekker ti tusen ganger så stort areal, sier Makris, som kan vise til forsøk gjort både i norske farvann og i amerikanske.

– Det eneste problemet er at fiskestimene er så langt borte at det tar lang tid å komme dit, for et forskningsfartøy som skal ta prøver, sier han.

Gode ser fordeler også knyttet til at beregningene kan bli mindre utsatt for variasjoner i toktdataene.

– I dag ser vi store variasjoner i dataene om det er natt eller dag, og i forhold til ut- og innvandring i løpet av sesongen. Slike feil kan i stor grad elimineres med den teknologien som denne sonaren representerer, sier han.

Effektiv leting

For fiskeflåten vil bruk av en slik sonar spare fartøyene for mye tid i å lete etter fiskestimer som er av en stor nok størrelse til å fiske på. Det vil i neste omgang også kunne spare fiskerne for utgifter til drivstoff, ved at det de kan gå rettere på fiskestimene.

De to forskerne sammenligner sonaren med en værradar som ser skyene på lang avstand og kan følge bevegelsene til skyene.

– Den er som værradaren i omfang, men som ekkoloddet i presisjon, sier Makris.

– Og den gir oss et bilde av hva som er i hele rommet, der vi tidligere bare kunne se gjennom et nøkkelhull, sier Godø, som illustrasjon på mulighetene med en slik sonar.

> **En sonar som når ti ganger lenger, dekker ti tusen ganger så stort areal.**
>
> Nicholas Makris ved Massachusetts institute of technology (MIT)

Se helheten

At teknologien gir forskerne mulighet til å se en større helhet, gjør at de fra å kunne studere fisken på individnivå og stimnivå, kan se hvordan fisk fordeler seg horisontalt i vannsøylen i hele området som sonaren dekker.

Det som gjør et slikt syn mulig er at sonaren sender lydbølger med mye lavere frekvens som rekker mye lengre ut enn dagens sonarer gjør. Sonaren kan sende lyd så lavt som på 400 hertz, men har sendt på 800 - 900 hertz i forsøkene de har gjort i norsk sone.

– Det er samme teknikk som hvalene bruker, når de kommuniserer på tvers av Atlanterhavet, viser Godø til.

Sonaren sender lydbølgene med 70 sekunders mellomrom, nok til at de får ekkoene tilbake 50 kilometer unna, før de forstyrres av neste lydpuls.

Videre forskning

Den videre forskningen vil være avhengig av hvilket behov det vil være for en slik sonar i forskningen og i fiskeleting. De to forskerne er i ferd med publisere fra undersøkelsen i 2014 , og vil trolig ikke gjøre noe nytt forsøk før i 2017 eller 2018.

– Det tar seks måneder å ordne utstyret, og ett år å planlegge, slik at nye forsøk må planlegges i god tid, sier Makris.

Gode viser til en samarbeidsavtale HI har med Forsvarets Forskningsinstitutt (FFI).

– Men vi trenger å etablere en prosjektavtale mellom næring, HI og FFI for å sette sammen et effektivt arbeidsteam som kan løse utfordringen knyttet til en videreføring av arbeidet.

– Vi har nok midler som vi kan forske på i USA, men må se en anvendelse for sonaren før vi setter i gang med noe, sier Markis. Han og Godø arbeider nå med en vitenskapelig artikkel som de vil publisere i et anerkjent vitenskapelig tidsskrift, med resultatene fra toktene de har fra 2014.

nils.torsvik@fbfi.no
Tlf. 932 56 325

– Alle like forundret

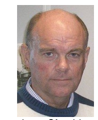

Lars Olav Lie

Fiskebåtreder Lars Olav Lie sier han knapt trodde sine øyne første gang han så resultatene fra den ny sonaren.

– Vi trodde ikke det var mulig. Vi hadde samlet skipperne i Lie-rederiet og alle var like forundret, sier han og kan ikke forestille seg hvilke muligheter en slik teknologi kan åpne for i fisket og forskning.

– I kolmulefiske kan fartøyene ligge og søke 40 kilometer rundt seg, der de i dag går med sonarer som maks når tre kilometer. Fiskerne kan også se hvor de skal nærme seg stimene, slik at mye tid kan spares i lete og fangstfasen, mener han. I forskningen mener han en slik sonar vil kunne gi et langt mer sannferdig bilde av hva som er i havet.

– I kartleggingen av nvg-sild kunne en slik sonar sett hele bildet, der forskerne i dag bare ser hva som er på ekkoloddet under fartøyet. Sonaren koster mye, men dette vil vi ha så mye igjen for at kostnaden står i forhold til besparelsene, sier han.

Lie fikk kjennskap til den nye sonaren for et par år siden, og har siden sett at den kan ha stor verdi for fiskeflåten dersom det utvikles en slik til kommersiell bruk. En kostnad på to millioner dollar, tilsvarende nær 17 millioner norske kroner, mener han ikke er avskrekkende når det måles mot besparelsene, både i tid og drivstoff.

Han mener det også bør settes i gang et forskningsprosjekt for utvikling av en slik sonar til kommersiell bruk, samt at norske forskningsfartøyer må få slike sonarer.

– Forskerne kan senke soneren ned i ulike skikt og få en totaloversikt over hvor mye fisk som står i stimene de måler. Dette bør Forskningsrådet bevilge penger til straks, mener han.

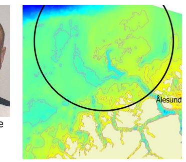

STORT OMRÅDE: Området sonaren kan kartlegge vil dekke store deler av området utenfor Ålesund.

Senator Kerry and Elected Officials Meet OAWRS Scientists Requests OAWRS Be Used To Assess Cod Populations

Hearing Before the Subcommittee on Oceans, Atmosphere, Fisheries, and Coast Guard, One Hundred Twelfth Congress, First Session US Senate Committee on Commerce, Science, and Transportation, March 8 2011; Technical Report; United States Senate, Govt. of United States: Washington, DC, USA, 2011.

Kerry, J. Following Field Hearing, Kerry Presses Urgent Next Steps to Aid Fishermen; Press Release: Washington, D.C., USA, 2011.

Kerry, J. Kerry Urges New Cod Assessment, Preparations for Economic Relief ; Press Release: Washington, D.C., USA, 2011.

Massachusetts State passes a bill to fund OAWRS experiment to help alleviate fisheries crisis, Spring 2012.

Senator Kerry meets Head of NOAA, Undersecretary of Commerce, to discuss OAWRS experiment in New England Spring 2012.


OAWRS in the Gulf of Maine and Georges Bank, Autumn 2006
Research Vessel (RV) Oceanus: OAWRS Receiver Ship
Towed Receiver Array
Fish Groups

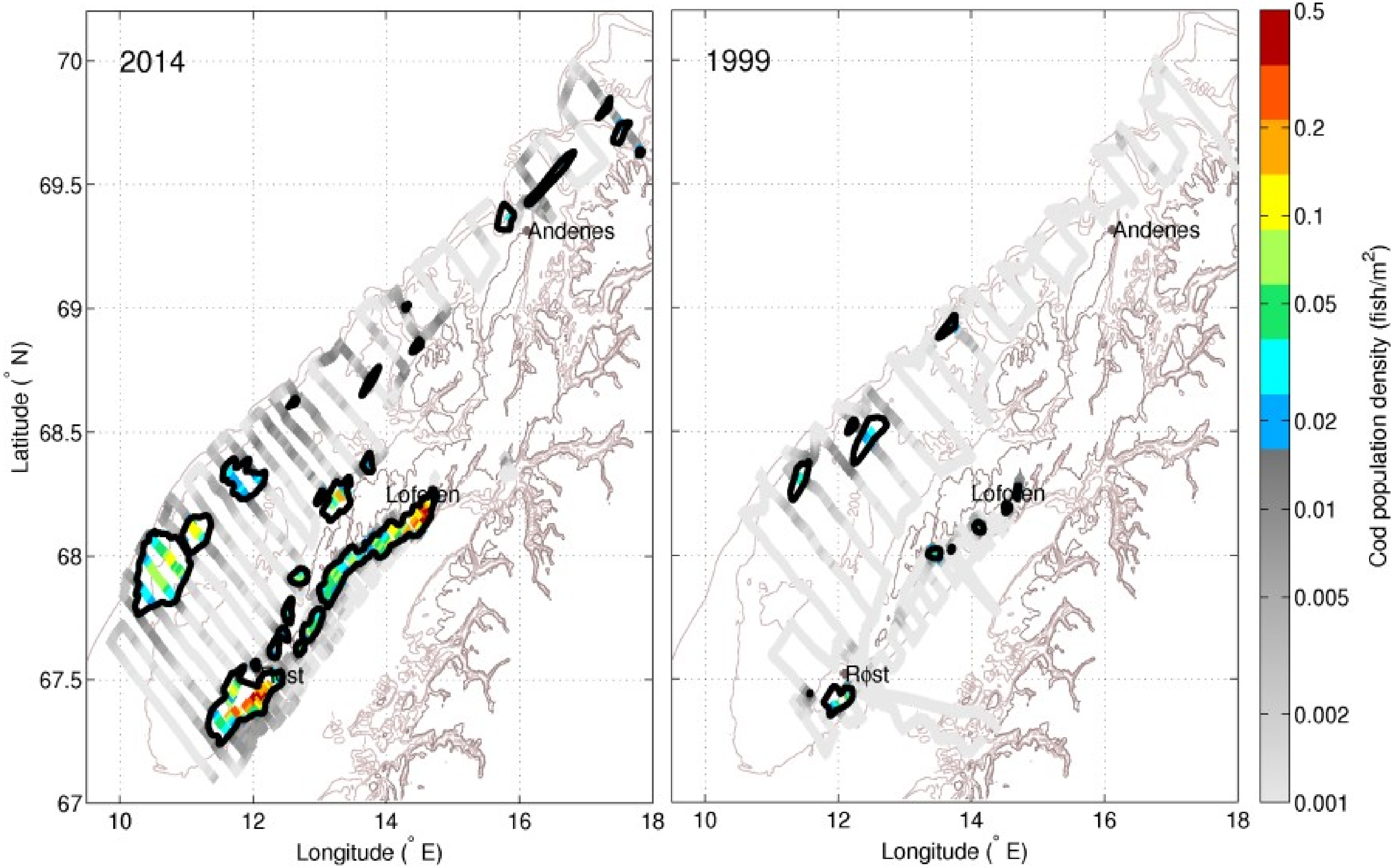

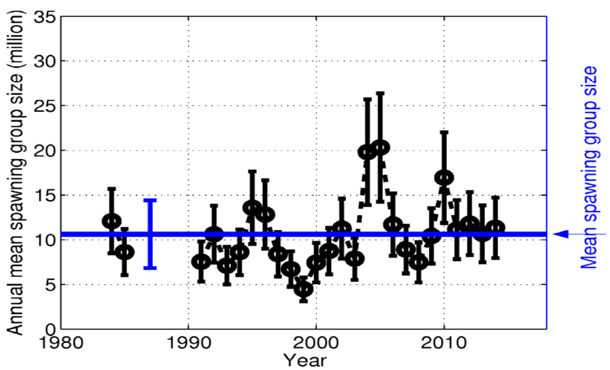

- Discrete cod spawning groups detected in 3 decades of line transect surveys and enumerated using group structural information obtained by OAWRS
- Mean annual Atlantic cod spawning group population in the Northeast arctic spawning ground is 10.6 million with standard deviation of 36 % of the mean.

Spawning Atlantic Cod Group Size Distribution

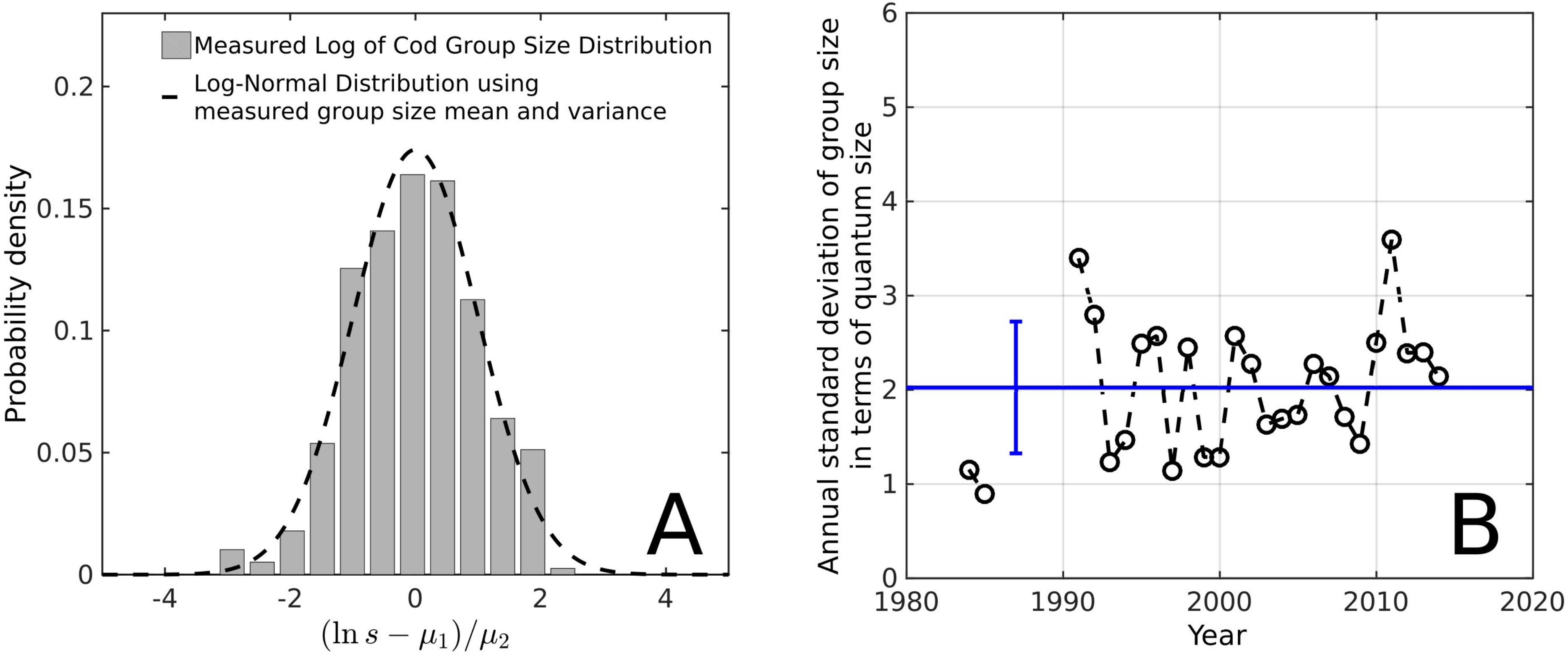

- Cod spawning group size in the Northeast Arctic spawning ground is consistent with a log-normal distribution
- Measured annual standard deviation of cod spawning group size is stable at two times the mean group size over the past three decades

Total Cod Spawning Population Decline to Within a Standard Deviation of Mean Cod Spawning Group Population

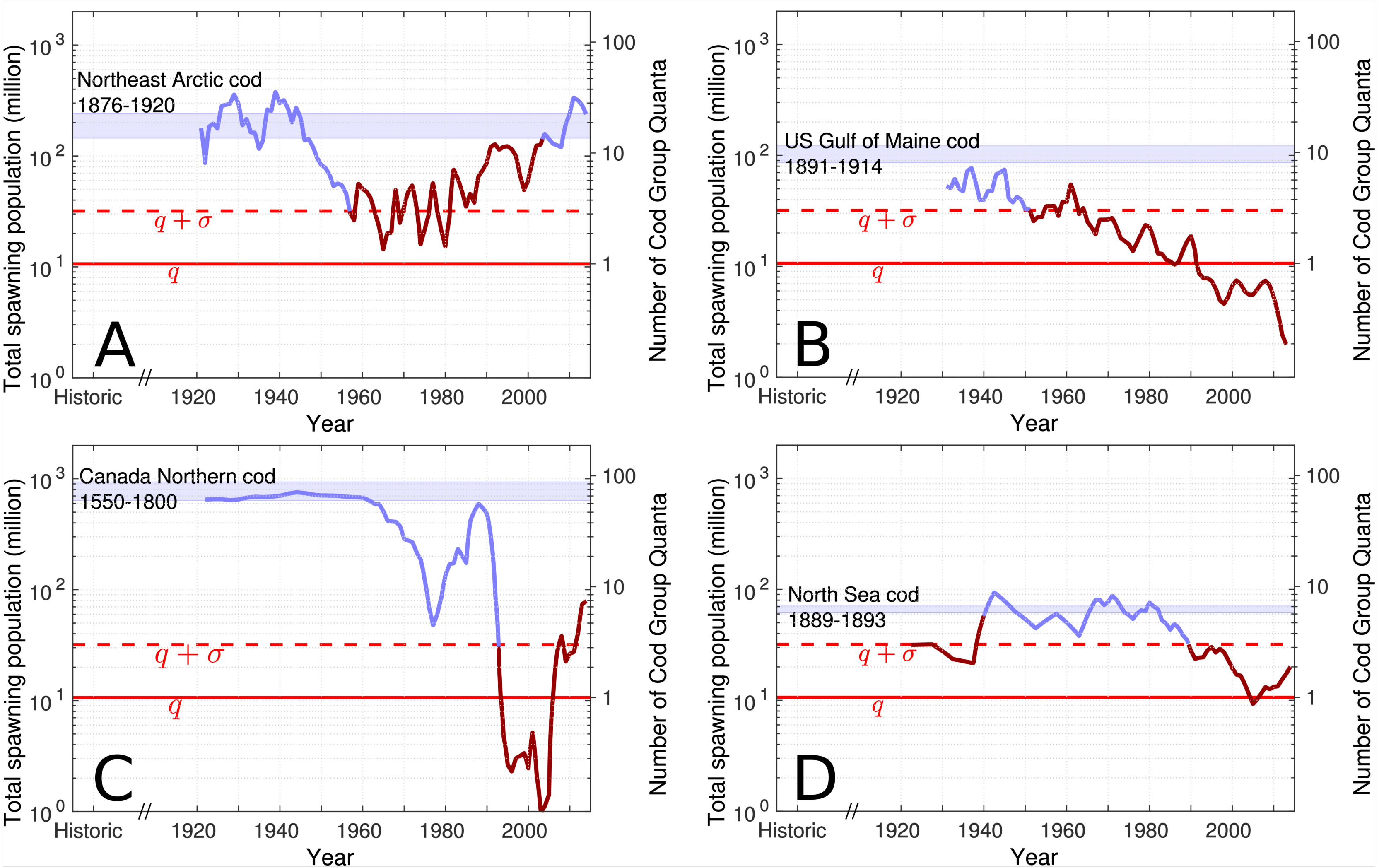

- Large differential between pre-industrial total Atlantic cod spawning population and mean cod spawning population
- Recovery to preindustrial total spawning population has not yet occurred or required decades once total spawning population declines to within a standard deviation of the mean cod spawning group population

Mean Daily Spawning Group Size of Atlantic Herring

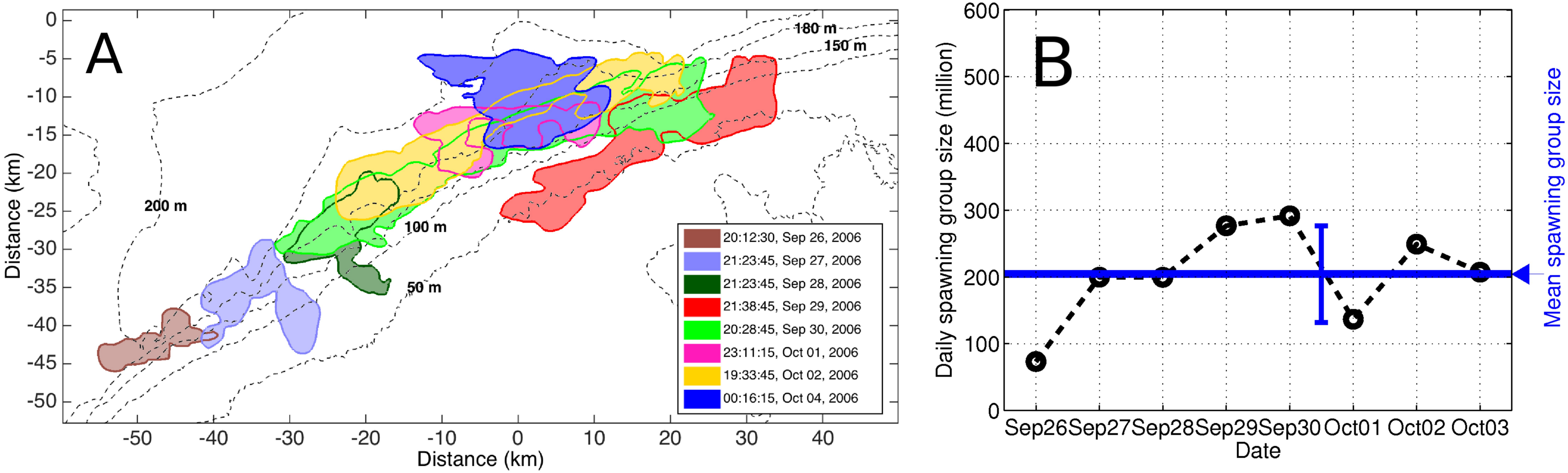

- Discrete herring spawning groups detected during the 8-day peak spawning period on the northern flank of Georges Bank
- Mean annual Atlantic herring spawning group population in Georges Bank spawning ground is 204 million with standard deviation of 35 % of the mean
- Summing the spawning group populations measured in a single instantaneous OAWRS image per day over the 8-day peak spawning period enabled accurate enumeration of the entire Georges Bank herring spawning population to within 7 percent of the independent NOAA estimate for 2006

Total Herring Spawning Population Decline to Within a Standard Deviation of Mean Herring Spawning Group Population

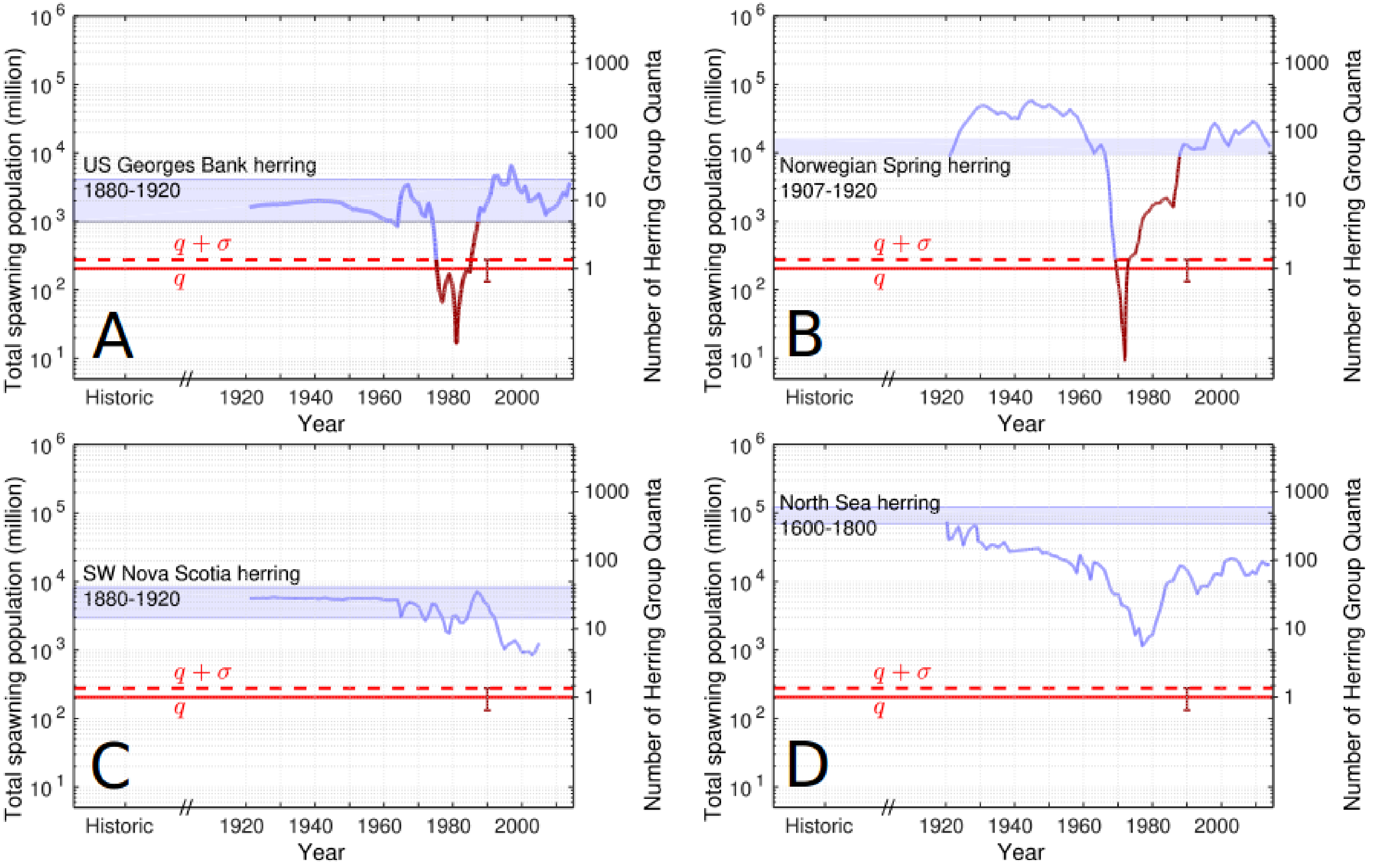

- Large differential between pre-industrial total Atlantic herring spawning population and mean herring spawning population
- Recovery to preindustrial total spawning population required decades once total spawning population declines to within a standard deviation of the mean cod spawning group population

Correcting for Attenuation Through Fish Shoals in OAWRS

Attenuation Estimated for Fish Shoals in other Regions Consistent with Observations

Environment/Species	Center Frequency	Typical Areal Density	Water Depth	Shoal Width or Transect	Shoal Depth	Shoal Vertical Thickness	Neutral Buoyancy Depth	Two Way Attenuation
New York Area herring	415 Hz	0.5 fish/m²	90 m	3 km	85 m	10 m	17 m	**0.2 dB**
Maine herring	950 Hz	2 fish/m²	200 m	2 km	150 m	30 m	82 m	**0.5 dB**
Nordic cod	955 Hz	0.01 fish/m²	100 m	10 km	75 m	50 m	75 m	**2 dB**

New York Area herring (2003)

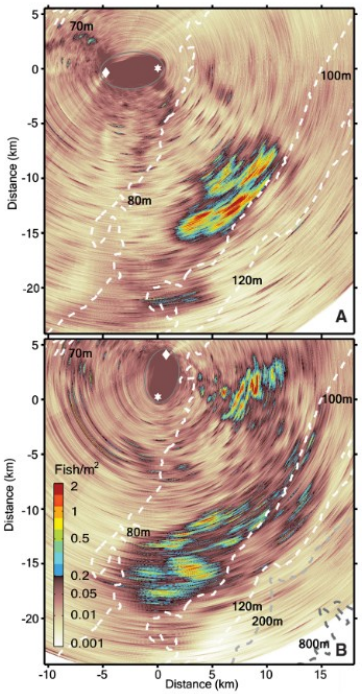

Gulf of Maine herring (2003)

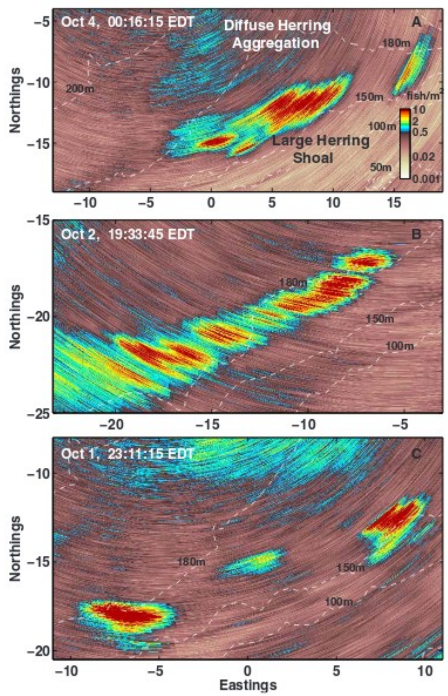

Nordic cod (2014)

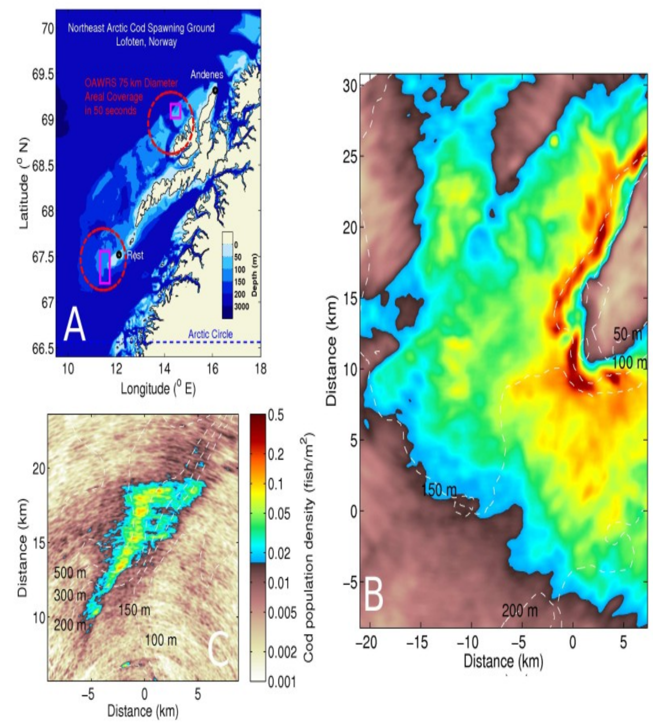

Attenuation due to Forward Propagation through Fish Shoals

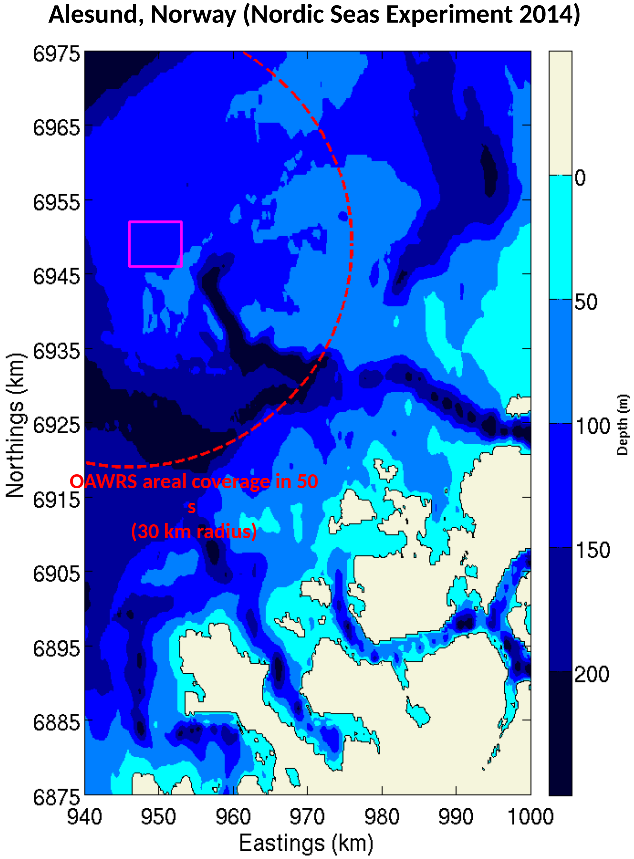

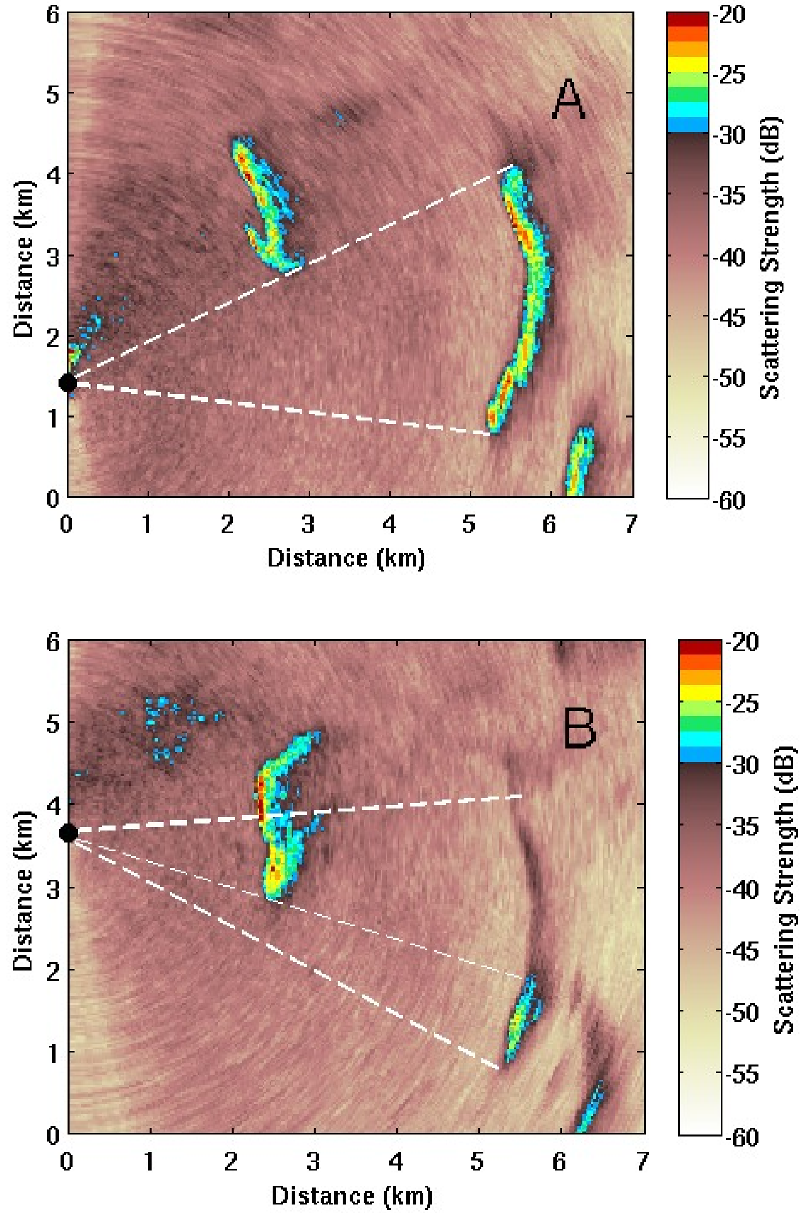

- 8.5 dB two-way attenuation is observed.

Attenuation due to Forward Propagation through Fish Shoals

Single scattering

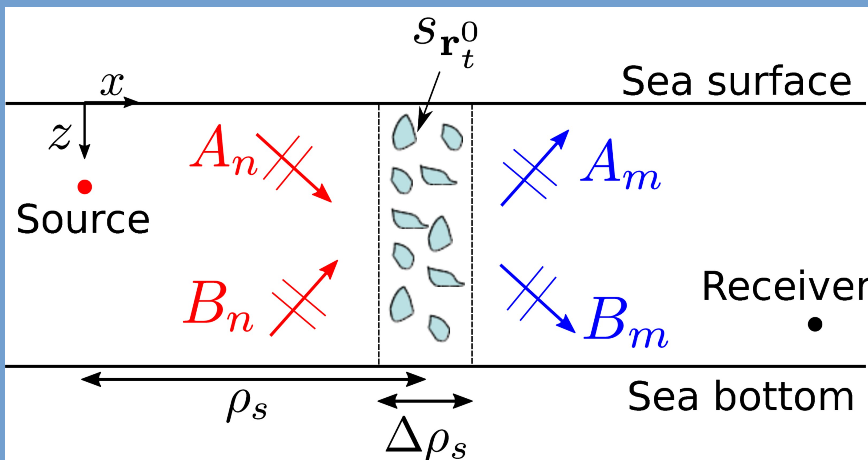

Multiple scattering by marching through differential slab elements

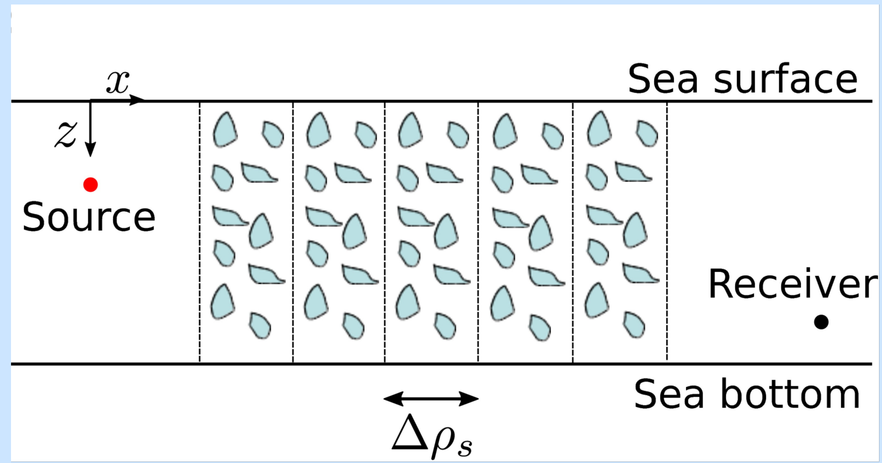

Difference equation

$$\langle \Phi_s^{(n)}(\mathbf{r}|\mathbf{r}_0; \Delta\rho_s(\rho_s))\rangle = \Delta\langle \Phi_T^{(n)}(\mathbf{r}|\mathbf{r}_0)\rangle = \langle \Phi_T^{(n)}(\mathbf{r}|\mathbf{r}_0)\rangle i\nu_n(\rho_s)\Delta\rho_s,$$

Integral equation

$$\int_{\psi_i^{(n)}}^{\langle\psi_T^{(n)}\rangle} \frac{d\langle \Phi_T^{(n)}(\mathbf{r}|\mathbf{r}_0)\rangle}{\langle \Phi_T^{(n)}(\mathbf{r}|\mathbf{r}_0)\rangle} = i\int_0^{\rho} \nu_n(\rho_s)d\rho_s,$$

Mean total field

$$\langle \Phi_T(\mathbf{r}|\mathbf{r}_0)\rangle = \sum_n \Phi_i^{(n)}(\mathbf{r}|\mathbf{r}_0)\, e^{i\int_0^{\rho}\nu_n(\rho_s)d\rho_s} \quad [1]$$

- Variance of the scattered field for fish shoals is negligible

[1] Ratilal, P. and Makris, N.C., 2005. Mean and covariance of the forward field propagated through a stratified ocean waveguide with three-dimensional random inhomogeneities. The Journal of the Acoustical Society of America, 118(6), pp.3532-3559.

Correcting for Attenuation

Approach:

- Step 1: Determine attenuation from first range step from estimated target strength and population density
- Step 2: Correct for attenuation at next range and repeat Step 1 at this range
- Iterate

$$I = I_0 e^{-\int_0^r \sigma(r') n_V(r') dr'}$$

$$\Delta L \equiv 10\log_{10}(I_0) - 10\log_{10}(I)$$

$$\Delta L = 10\log_{10}(e)\sigma\frac{1}{D}\int_0^r n_A(r')dr'$$

$$n_{A,corrected} = n_{A,uncorrected} + \Delta L$$

$$n_{A,corrected}(r) = n_{A,uncorrected}(r) + 10\log_{10}(e)\sigma\frac{1}{D}\int_0^r n_{A,corrected}(r')dr'$$

Uncorrected scattering strength

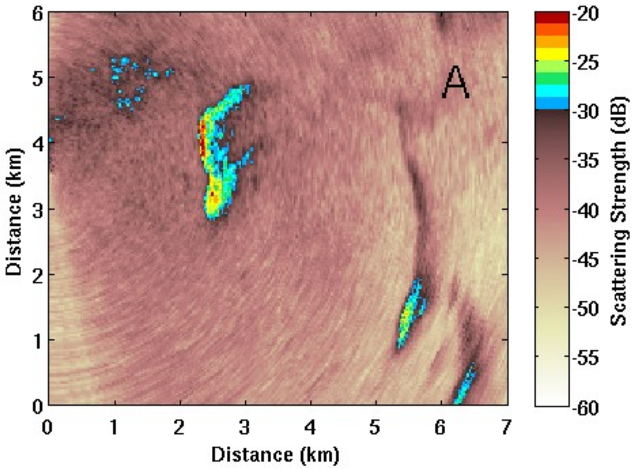

Corrected scattering strength

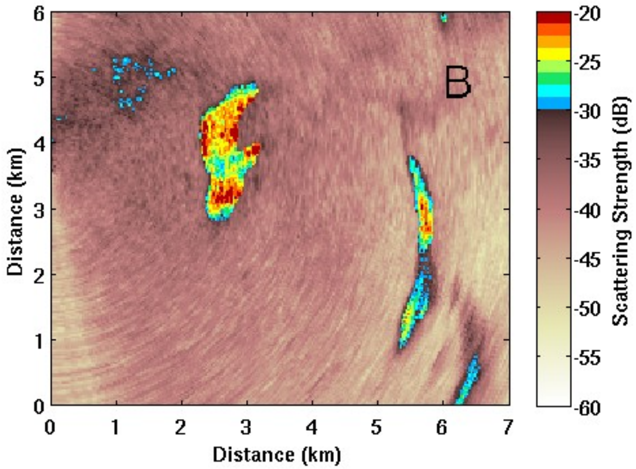

- The corrected scattering strength matches the unattenuated scattering strength of the same shoal to within 1.1 dB

Maximum-Likelihood Deconvolution of Beamformed Images with Signal-Dependent Speckle Fluctuation from Gaussian Random Fields: With Application to Ocean Acoustic Waveguide Remote Sensing (OAWRS)

Maximum Likelihood (ML) Deconvolved Beamforming

Standard statistical beamforming models assumes deterministic signal in additive noise. For ocean sensing cases, the signal is typically randomized and follows Circular Complex Gaussian Random (CCGR) statistics by the central limit theorem [1].

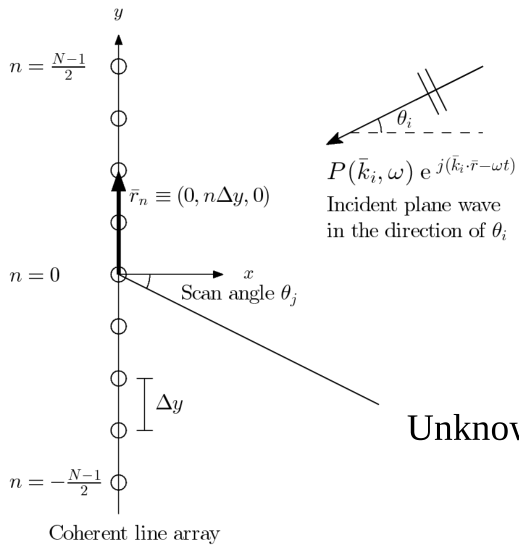

Incident plane wave: $P_i(\bar{r},t) = P(\bar{k}_i,\omega) e^{j(\bar{k}_i \cdot \bar{r} - \omega t)}$

Beamformed intensity measurement at θ_j is given by:

$$W_j = W(\theta_j,\omega) = \left| \sum_{i=1}^{M} P(\bar{k}_i,\omega) B(\sin\theta_j - \sin\theta_i,\omega) \right|^2$$

The expected beamformed intensity vector is given by:

$$\sigma = \mathbb{B}\mathbf{S}$$

Measured beamformed intensities $\boldsymbol{\sigma}$: $\langle W_j \rangle$

Unknown incident plane wave intensities $\mathbf{S}$: $S_i = \langle P(\bar{k}_i,\omega) P^*(\bar{k}_i,\omega) \rangle$

Known beam pattern $\mathbb{B}$: $\mathbb{B}_{ij} = | B_{ij} |^2 = | B(\sin\theta_j - \sin\theta_i,\omega) |^2$

The conditional probability distribution for all measurements in vector **W** given **S** is the product of gamma distribution

$$P(\mathbf{W}|\mathbf{S}) = \prod_{j=1}^{J} \frac{\left[\frac{\mu_j}{\sigma_j(\mathbf{S})}\right]^{\mu_j} W_j^{\mu_j - 1} \exp\left[-\mu_j \frac{W_j}{\sigma_j(\mathbf{S})}\right]}{\Gamma(\mu_j)}$$

The log-likelihood function is:

$$\ln P(\mathbf{L}|\mathbf{S}) = \sum_{j=1}^{J} \mu_j \ln\left[\frac{\mu_j}{\sigma_j'(\mathbf{S})}\right] + \left[\frac{-\mu_j \exp(L_j)}{\sigma_j'(\mathbf{S})} + \mu_j L_j\right] - \ln\Gamma(\mu_j)$$

where $L_j = \ln(W_j / I_{ref})$

The maximum likelihood estimate (MLE) of **S** is given by:

$$\hat{\mathbf{S}} = \arg\max_{\mathbf{S}} [\ln P(\mathbf{L}|\mathbf{S})] = [\mathbb{B}\hat{d}_\sigma \mathbb{B}^T]^{-1} \mathbb{B}\hat{d}_\sigma \mathbf{W}$$

[1] N. C. Makris, "A foundation for logarithmic measures of fluctuating intensity in pattern recognition", *Optics Letters* **20**, 2012-2014 (1995).

Comparison of ML Deconvolved and Conventional Beamformed Areal Population Density of a Large Spawning Atlantic Herring Shoal

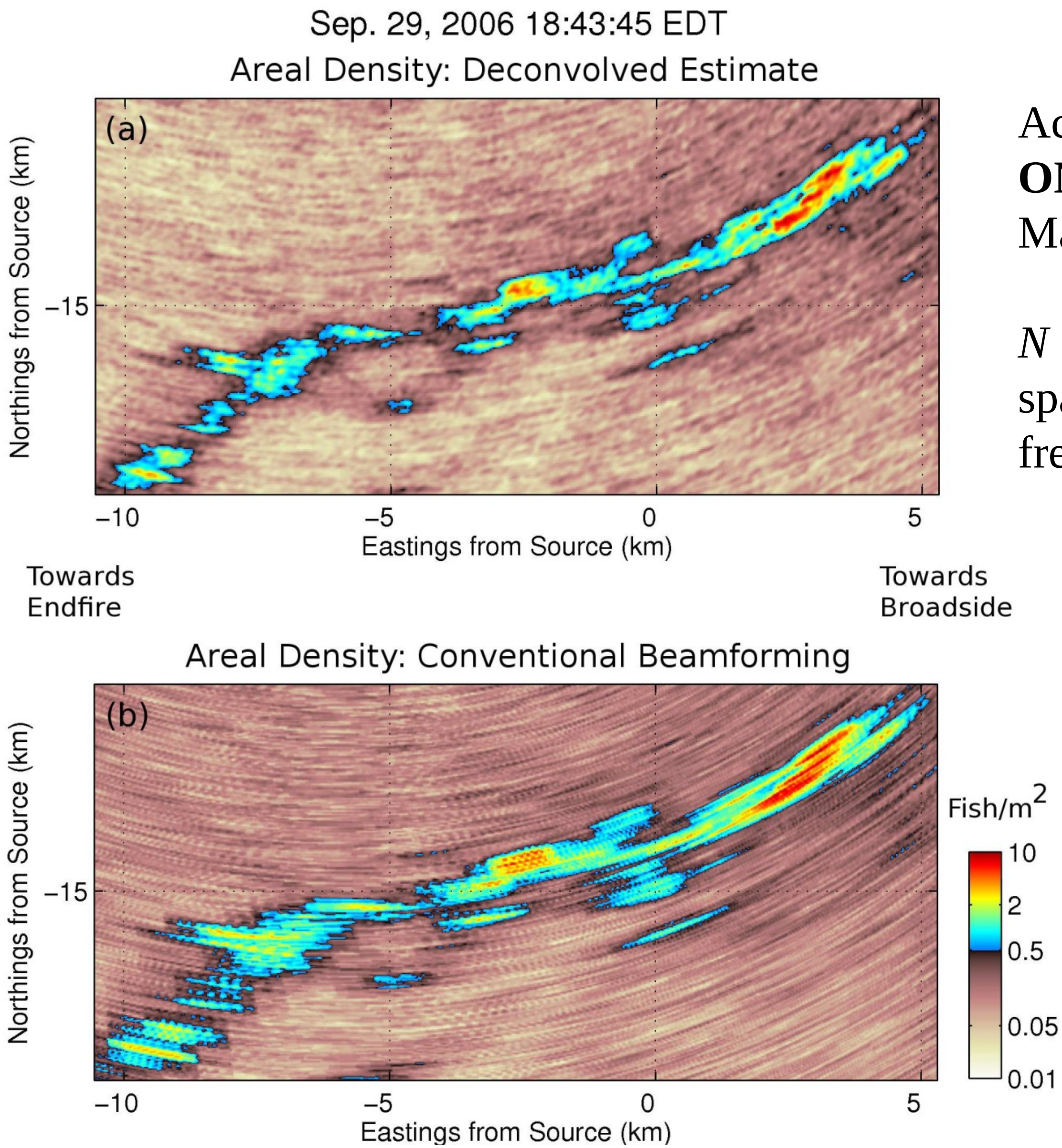

Acoustic data was acquired using the **ONR-FORA** array during the Gulf of Maine 2006 Experiment.

N = 64 receiver array elements are spaced 0.75 m apart with the sensing frequency at 950 Hz.

Angular resolution is improved by up to a factor of 2.

Cross-range resolution is improved by ~500 m at a range of 15 km away from the receiver

A. D. Jain and N. C. Makris, "Maximum Likelihood Deconvolution of Beamformed Images with Signal-Dependent Speckle Fluctuations from Gaussian Random Fields: With Application to Ocean Acoustic Waveguide Remote Sensing (OAWRS)", *Remote Sens.* **8**, 694 (2016).

Comparison of ML Deconvolved and Conventional Beamformed Areal Population Density of a Large Spawning Atlantic Herring Shoal (cont.)

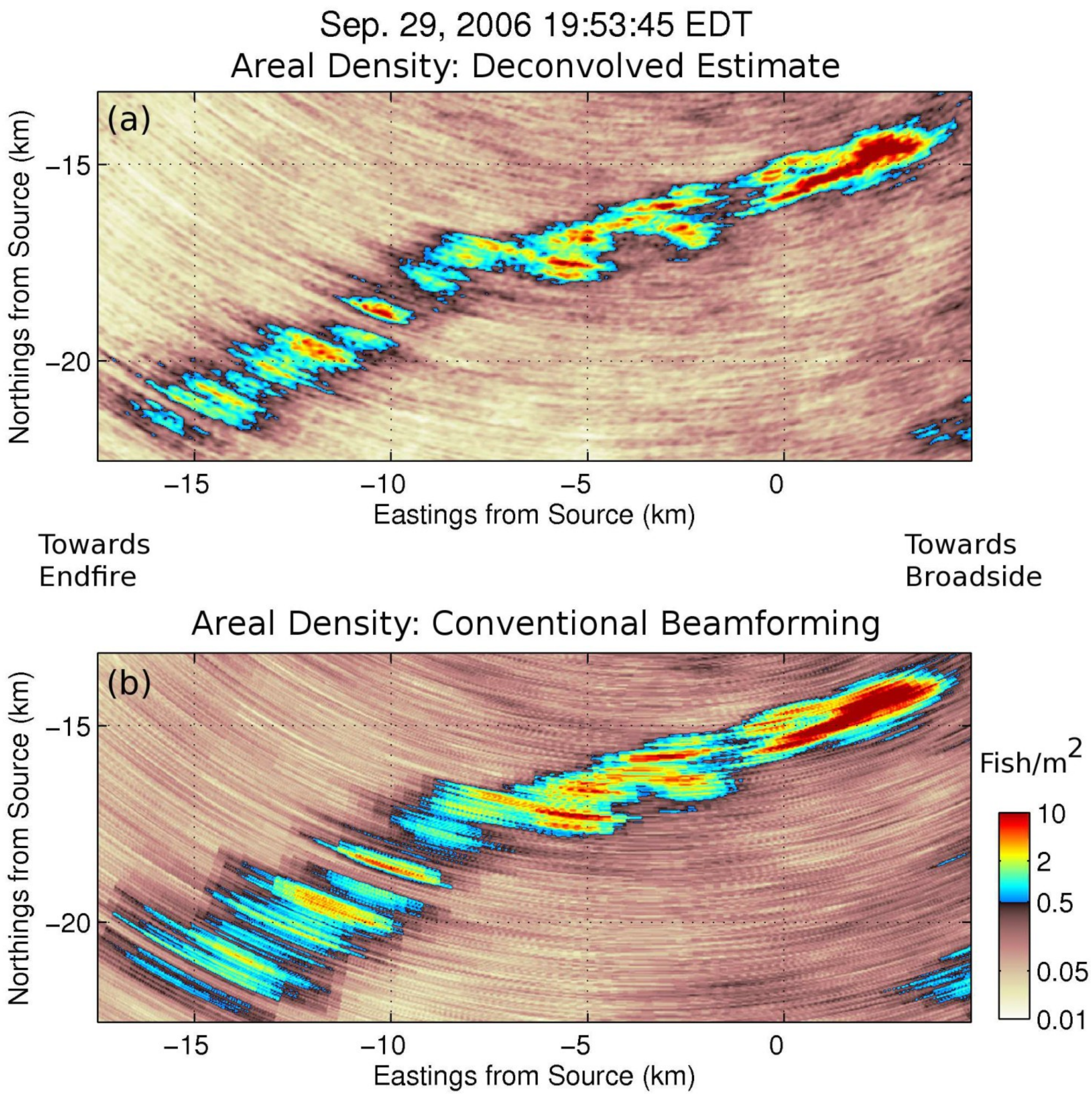

A. D. Jain and N. C. Makris, "Maximum Likelihood Deconvolution of Beamformed Images with Signal-Dependent Speckle Fluctuations from Gaussian Random Fields: With Application to Ocean Acoustic Waveguide Remote Sensing (OAWRS)", *Remote Sens.* **8**, 694 (2016).

Comparison of ML Deconvolved and Conventional Beamformed Areal Population Density of a Large Spawning Atlantic Herring Shoal (cont.)

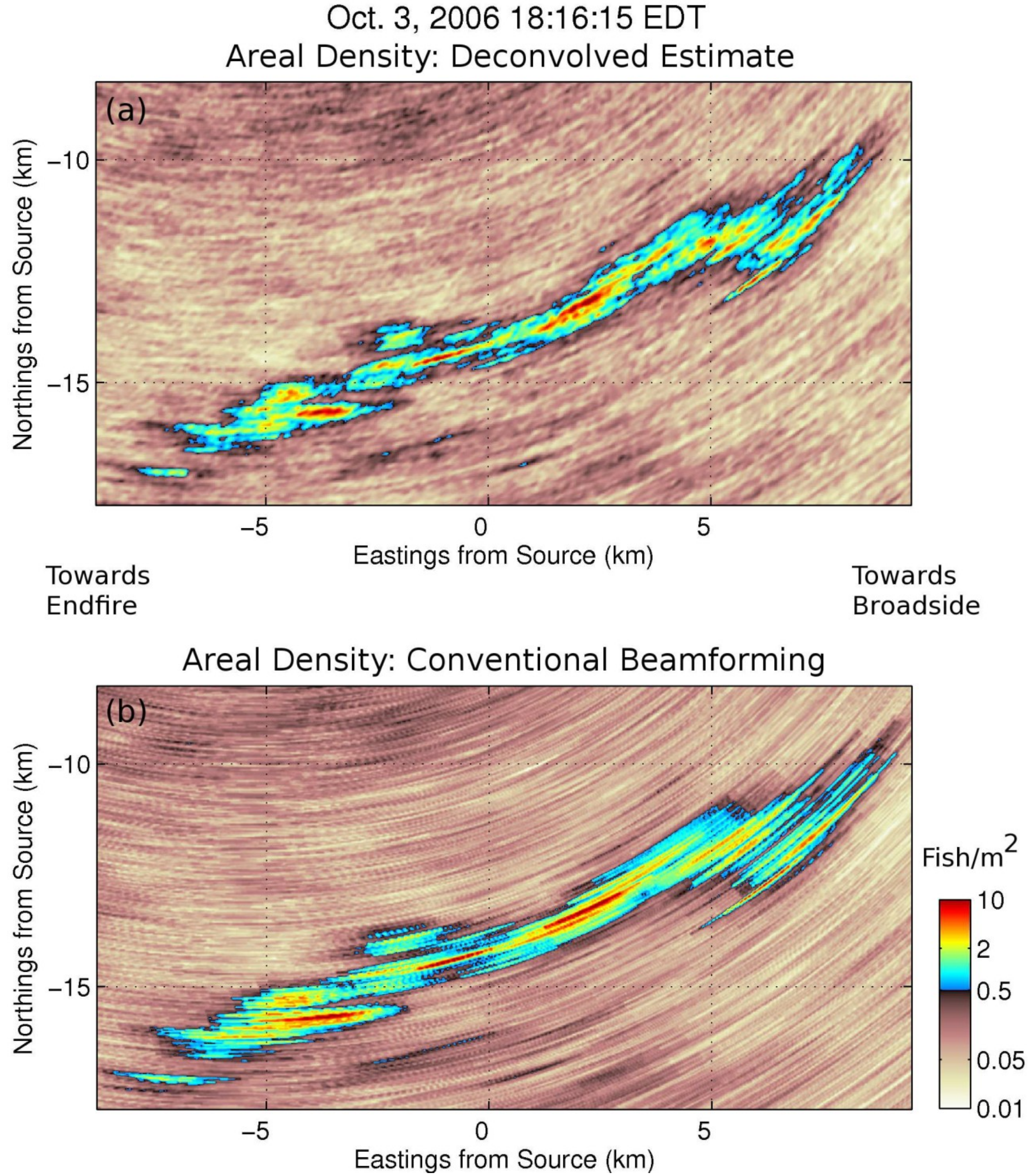

A. D. Jain and N. C. Makris, "Maximum Likelihood Deconvolution of Beamformed Images with Signal-Dependent Speckle Fluctuations from Gaussian Random Fields: With Application to Ocean Acoustic Waveguide Remote Sensing (OAWRS)", *Remote Sens.* **8**, 694 (2016).

Comparison of ML Deconvolved and Conventional Beamformed Areal Population Density of a Large Spawning Atlantic Herring Shoal (cont.)

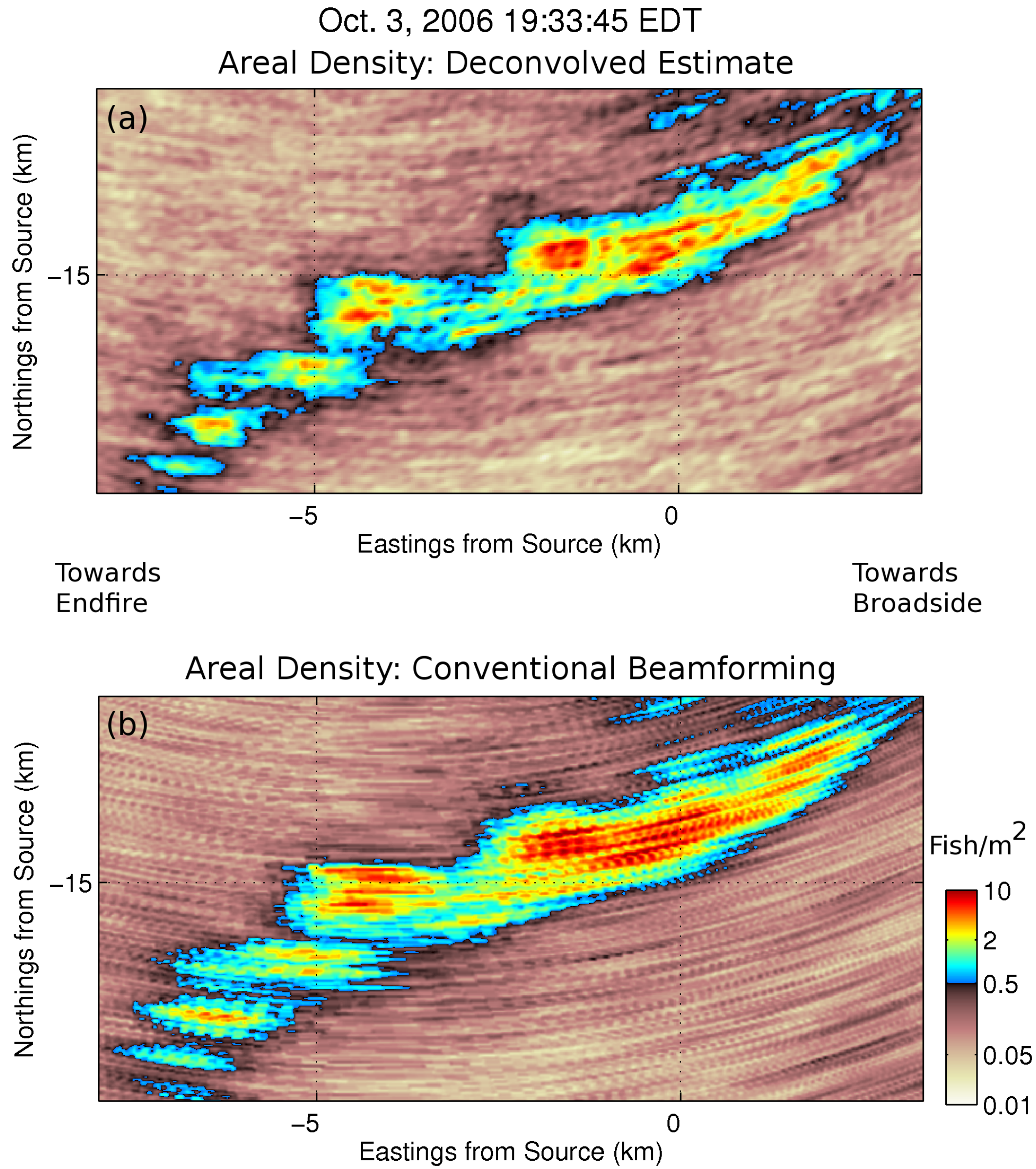

A. D. Jain and N. C. Makris, "Maximum Likelihood Deconvolution of Beamformed Images with Signal-Dependent Speckle Fluctuations from Gaussian Random Fields: With Application to Ocean Acoustic Waveguide Remote Sensing (OAWRS)", *Remote Sens.* **8**, 694 (2016).

Comparison of ML Deconvolved and Conventional Beamformed Areal Population Density of a Large Spawning Atlantic Herring Shoal (cont.)

Angular resolution is further improved by deconvolving [1] beamformed areal population density using a full nonuniformly-spaced multiple-nested array [2,3].

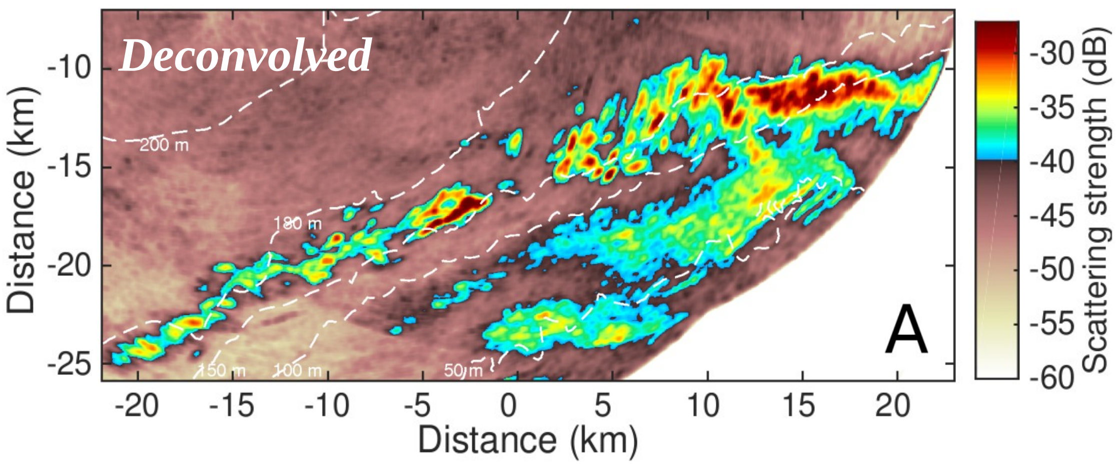

N = 128 receiver array elements with inter-element spacing varying from 0.375 m to 1.5 m is used for beamforming followed by deconvolution. The total length of the array is 94.5 m.

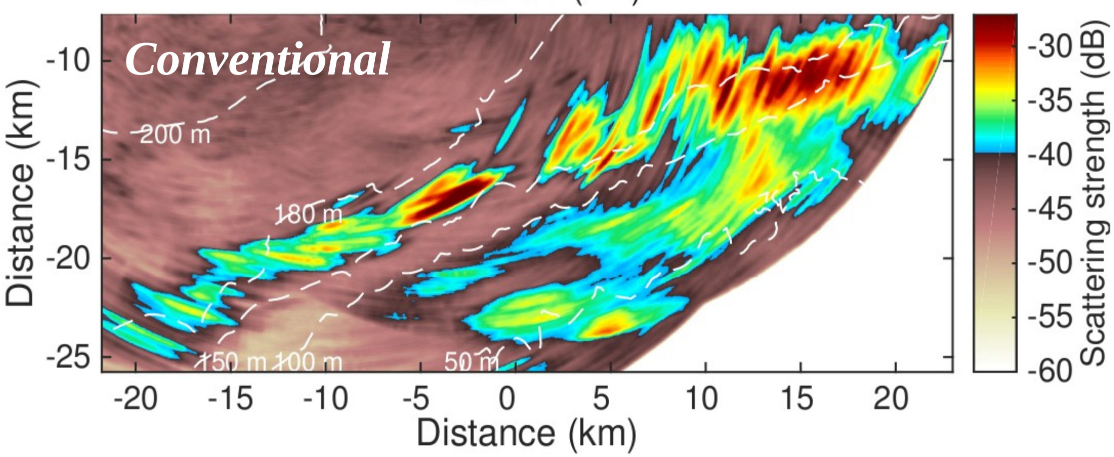

N = 64 receiver array elements are spaced 0.75 m apart with a total length of 47.25 m.

[1] A. D. Jain and N. C. Makris, “Maximum Likelihood Deconvolution of Beamformed Images with Signal-Dependent Speckle Fluctuations from Gaussian Random Fields: With Application to Ocean Acoustic Waveguide Remote Sensing (OAWRS)”, Remote Sensing, 8, 694 (2016).

[2] D. Wang and P. Ratilal, “Angular Resolution Enhancement Provided by Nonuniformly-Spaced Linear Hydrophone Arrays in Ocean Acoustic Waveguide Remote Sensing,” Remote Sensing, 9(10), 1036 (2017).

[3] D. H. Yi, Z. Gong, J. M. Jech, P. Ratilal, and N. C. Makris, "Instantaneous 3D Continental-Shelf Scale Imaging of Oceanic Fish by Multi-Spectral Resonance Sensing Reveals Group Behavior during Spawning Migration," Remote Sens. 10(1), 108, (2018).

Instantaneous 3D Continental-Shelf Scale Imaging of Oceanic Fish by Multi-Spectral Resonance Sensing

Instantaneous 3D Continental-Shelf Scale Imaging of Oceanic Fish by Multi-Spectral Resonance Sensing

D.H. Yi, Z. Gong, J.M. Jech, P. Ratilal, and N.C. Makris, “Instantaneous 3D continental-shelf scale imaging of oceanic fish by multi-spectral resonance sensing reveals group behavior during spawning migration,” Remote Sens. 10, 108 (2018).

Spawning migration of Georges Bank herring, 29 September 2006, Northern flank of the Georges Bank

- Large herring groups were observed during an upslope migration towards spawning grounds.
- Herring begin shoal formation at locations with seafloor depth ~140 m to 180 m.
- Subsequently migrate towards spawning grounds at approximately 50 m depth.

Migration of shoal over four instantaneous OAWRS images

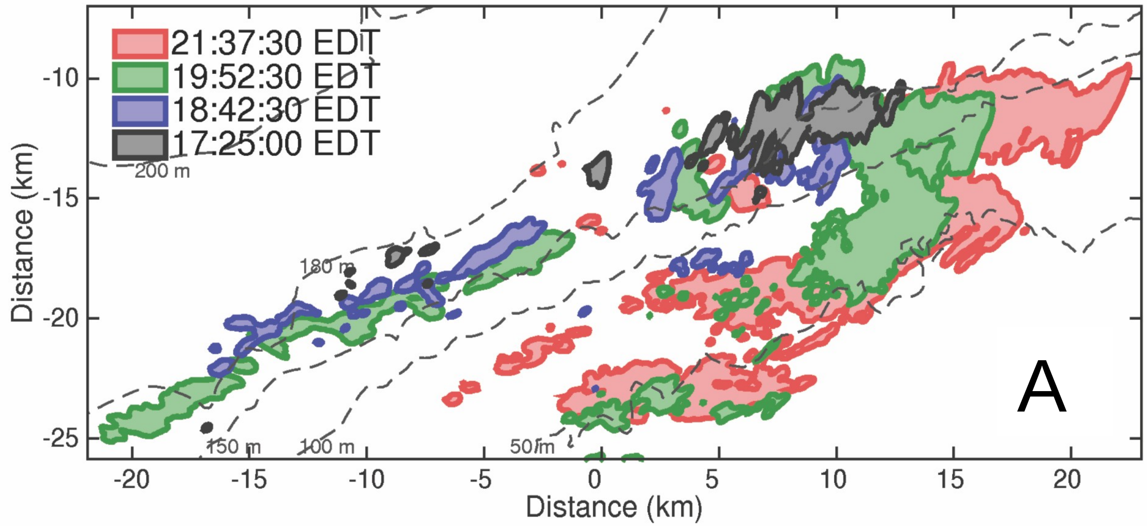

Maximum Scattering Strength during migration

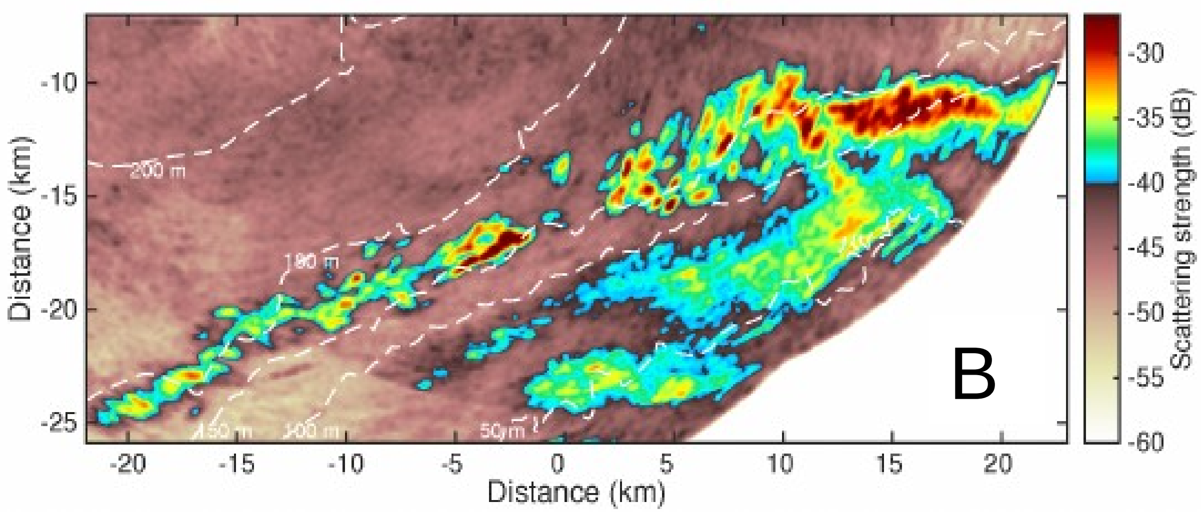

Herring swimbladder resonance peak shift in space is captured by multi-spectral sensing with OAWRS during spawning migration

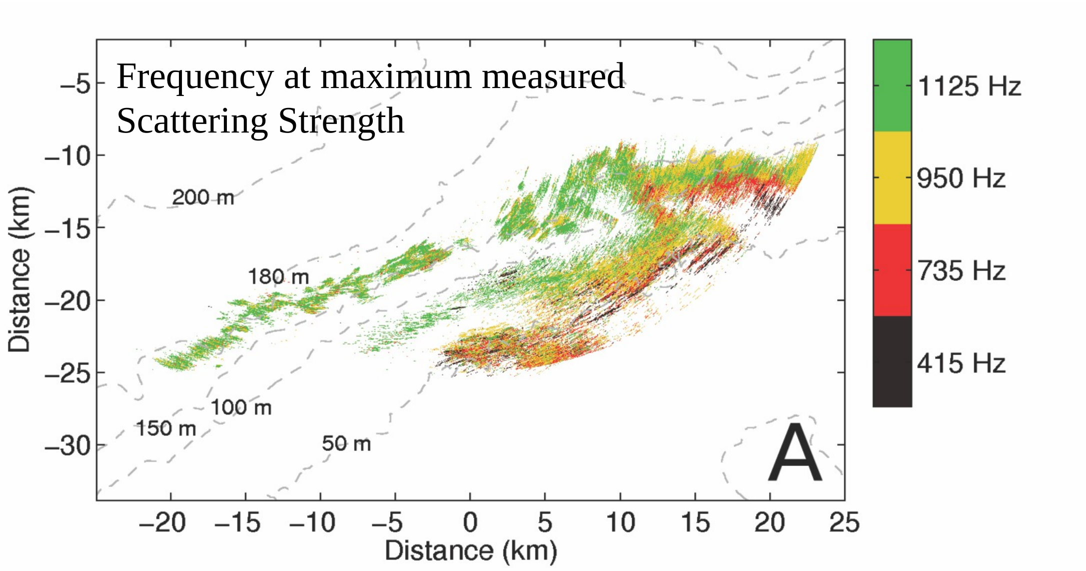

- Frequency at which maximum acoustic scattering occurs decreases with decreasing seafloor depth.

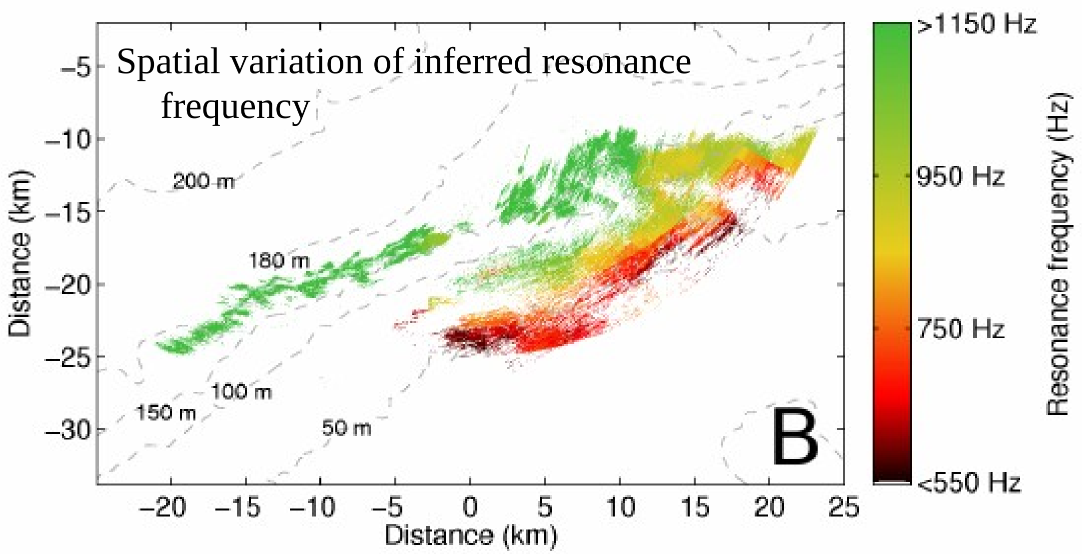

- Measured shift consistent with theoretically expected shift in resonance frequency for shallower fish groups due to swimbladder expansion. Fish shoal depth can then be inferred.

Variation in the frequency response of fish shoal scattering as a function of seafloor depth

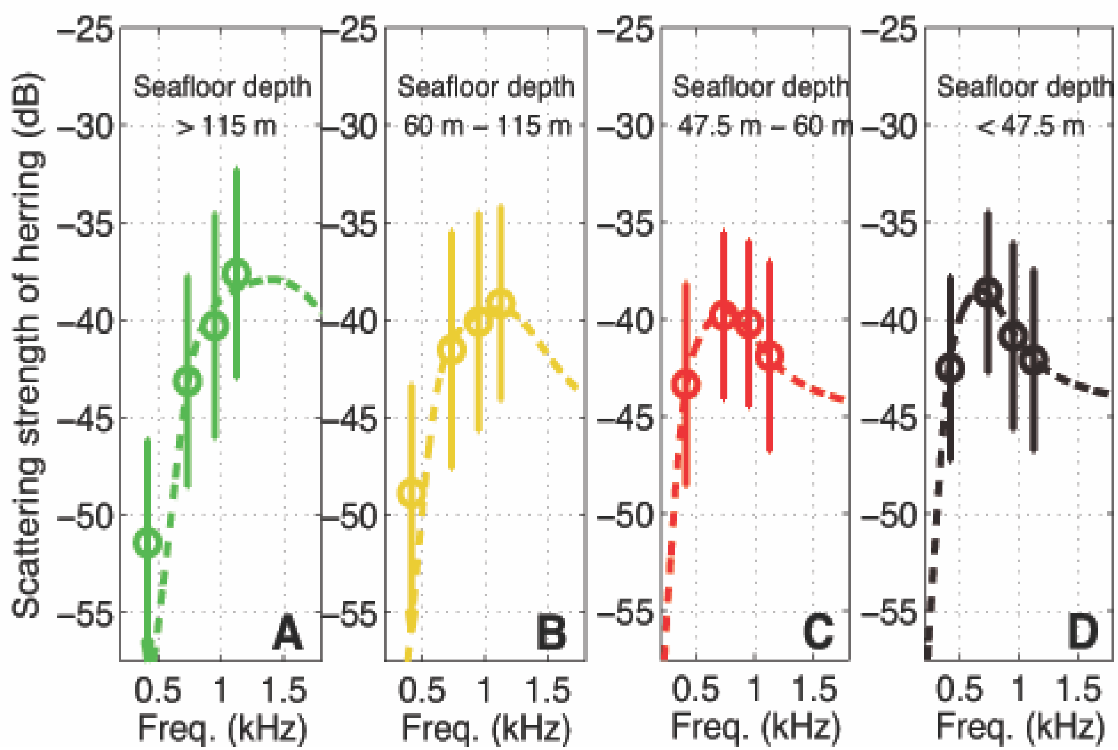

- Resonance peak of herring scattering consistently shifts from frequencies higher than 1125 Hz to lower than 735 Hz with decreasing seafloor depths.
- Measured frequency response below resonance has rapid roll-off roughly 15-20 dB/octave consistent with theoretically expected sub-resonance behavior.
- Resonance peak moves to within the available frequency band of the measured data for shallower fish shoal depths.

Inferring herring group parameters

The expected Scattering Strength SS^{model} of herring group in a uniformly-distributed vertical layer with mean shoal depth z_0, shoal thickness H, neutral buoyancy depth z_{nb}, and areal population density n_A at frequency f is determined as

$$SS^{model}(z_0, H, z_{nb}, n_A, f_j) = 10\log_{10}\left(\frac{1}{H}\int_{z_0-H/2}^{z_0+H/2}\int_l \left|\frac{S(z, z_{nb}, l, f)}{k}\right|^2 g(l)\,dl\,dz\right) + 10\log_{10} n_A$$

where S is the far-field scatter function of a single herring, k is the acoustic wavenumber, l is the fork length of herring, $g(l)$ is the truncated Gaussian probability distribution, and z is the herring depth.

Herring group parameters such as mean depth z_0, shoal thickness H, neutral buoyancy depth z_{nb}, and areal density n_A are then inferred by minimizing the magnitude of the 4-dimensional cost function

$$\Delta(z_0, H, z_{nb}, n_A) = -\sum_{k=1}^{N}\sum_{j=1}^{N_f}\frac{1}{2\sigma_j^2}\left(SS_{jk}^{data} - SS^{model}(z_0, H, z_{nb}, n_A, f_j)\right)^2$$

Inferred variation in herring shoal depth during spawning migration

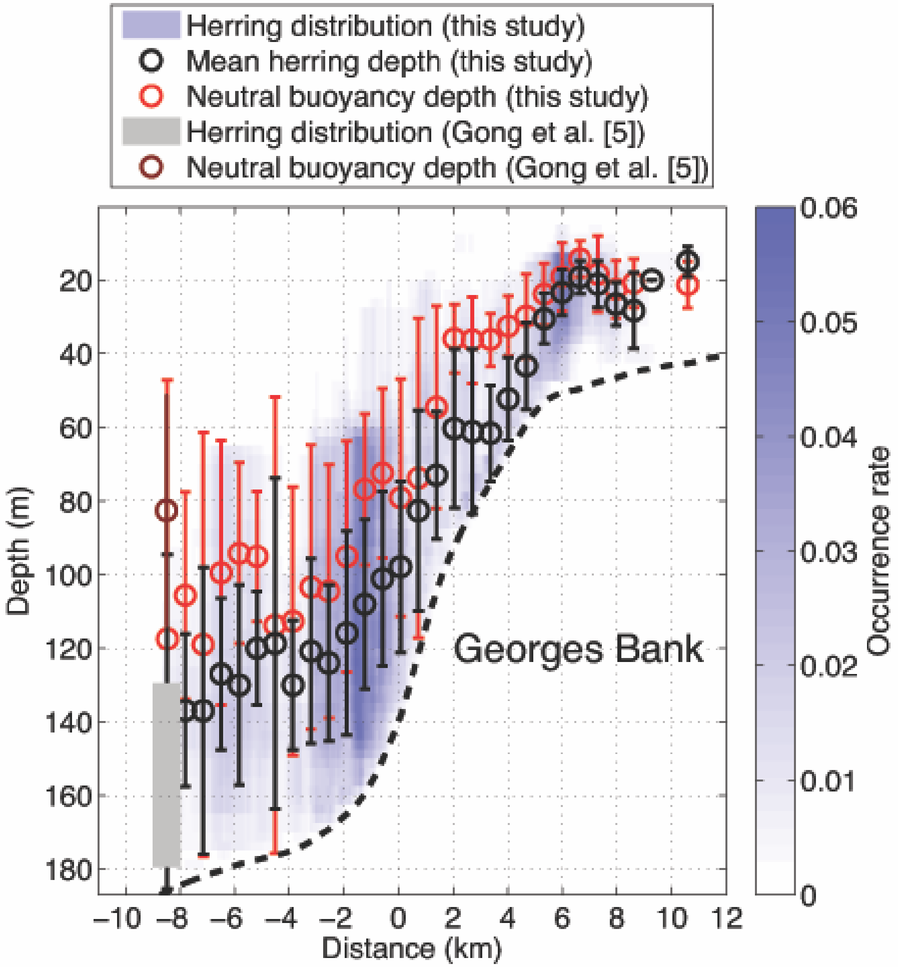

- Herring groups maintain near-bottom vertical distributions with negative buoyancy throughout the migration.

- Decrease in neutral buoyancy depth is consistent with previously observed gas release from herring in vertical migration.

3D distribution of herring shoal during spawning migration

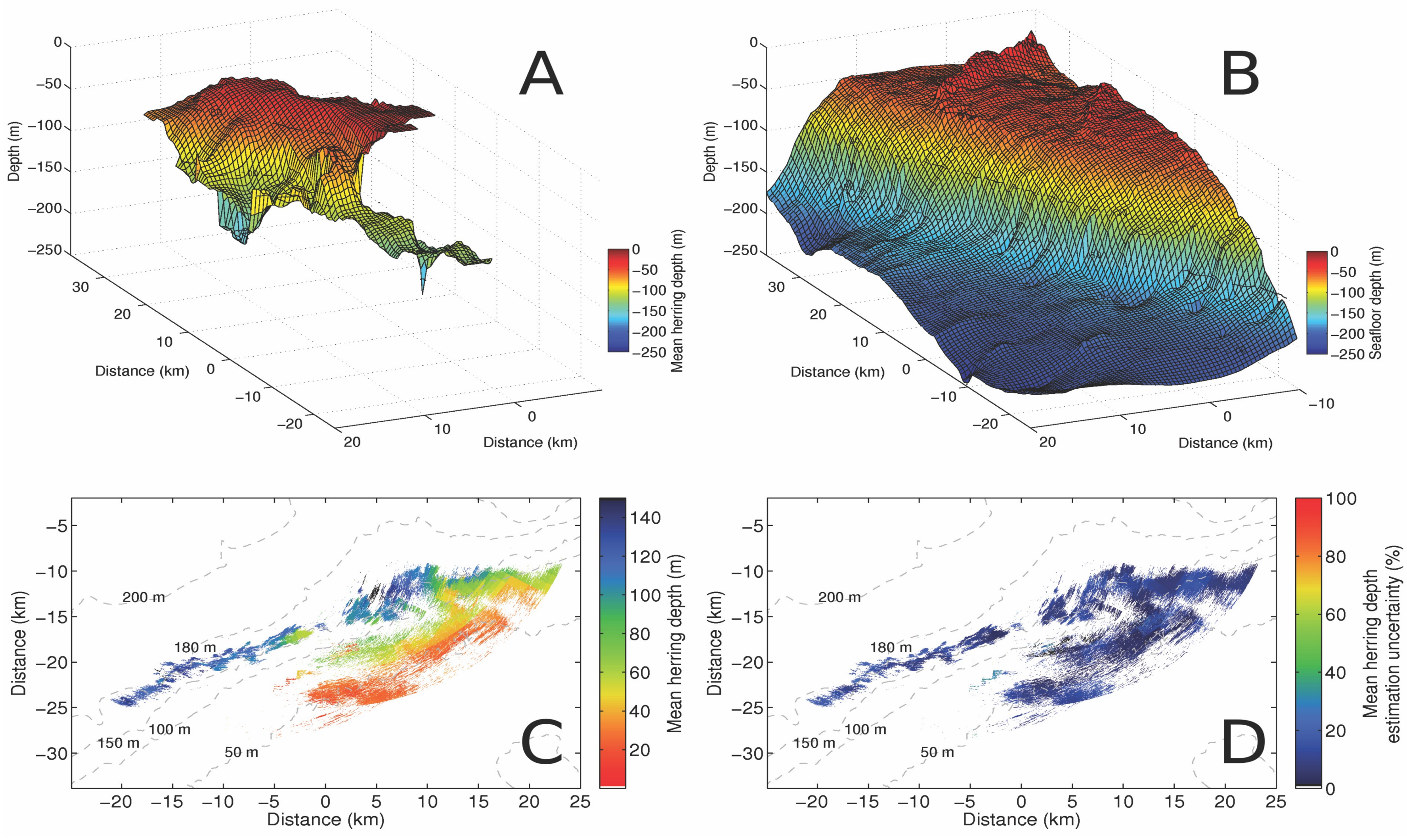

- 3D surface of mean herring group depth is determined from multi-frequency measurements.
- The mean herring group depth and the seafloor depth are found to be highly correlated (0.9 correlation coefficient) for migratory paths along the bathymetric gradient.

Acoustic Temporal Coherence After Propagation Through Time Varying Ocean Waveguides

Application to Active Sensing in an Ocean Waveguide

Coherence Time (τ_c) Determines Number of Samples for Variance Reduction [1]

Coherence Time Determines Pulse Compression Resolution Limits

Ocean Acoustic Waveguide Remote Sensing (OAWRS) system [2,3]

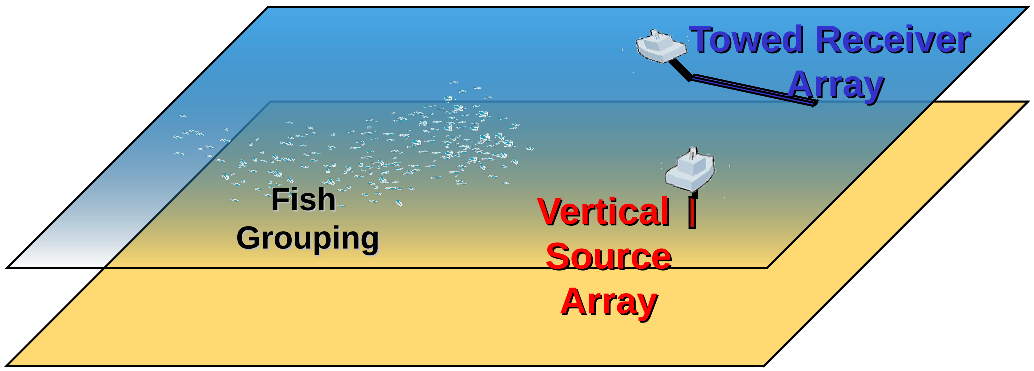

Matched filtering

Pulse compression: Higher range resolution and SNR

Requires τ_c on order of pulse time

Stationary averaging

Reduce the variance (speckle)

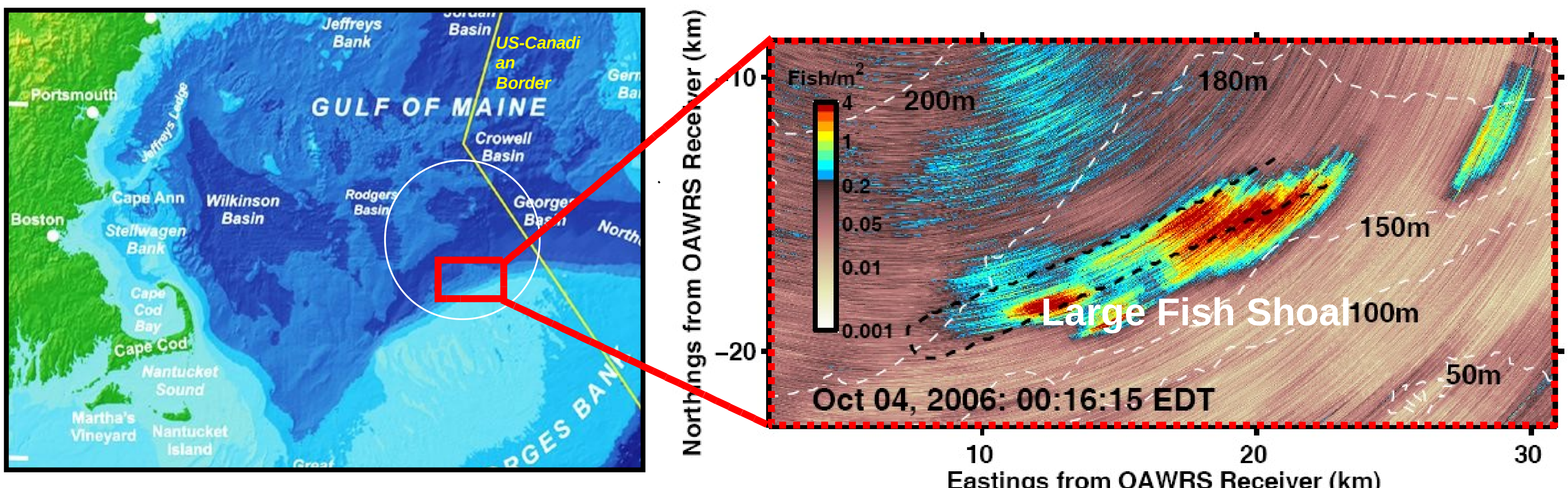

OAWRS Instantaneous Diameter 100 km [3]

OAWRS Instantaneous Image [3]

[1] Makris, N.C., 1996. The effect of saturated transmission scintillation on ocean acoustic intensity measurements. The Journal of the Acoustical Society of America, 100(2), pp.769-783.

[2] Makris et al, Science 2006 [3] Makris et al, Science 2009

Logarithmic (Decibel) Statistics of Gaussian Field Measurements

Makris JASA 1996

Intensity Measurement

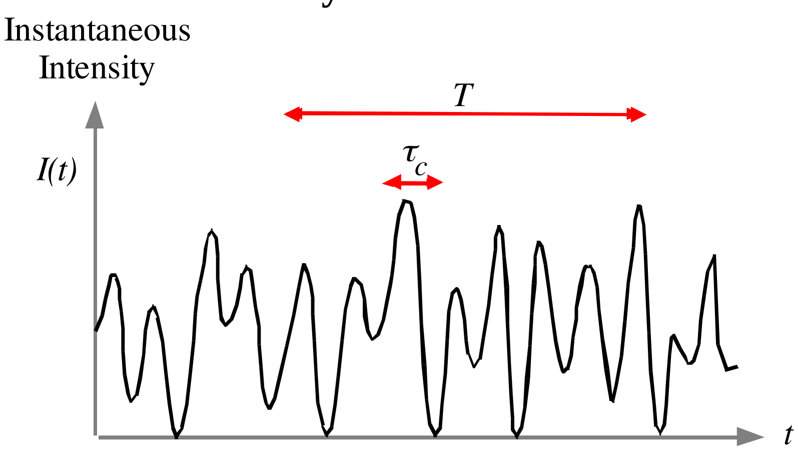

τ_c = Fluctuation Timescale = 1/Bandwidth

T = Measurement Time

$$W(t) = \frac{1}{T}\int_{t-T/2}^{t+T/2} I(t')dt' =$$ **Time Averaged Intensity**

$$\mu = \frac{\mathrm{Var}\left[I(t)\right]}{\mathrm{Var}\left[W(t)\right]}$$ = Time-Bandwidth Product

= Number of Independent Intensity Fluctuations in T

Logarithmic Intensity Measurement

$$L = \log\frac{W}{I_{ref}}$$

$$P(L) = \frac{\mu^\mu}{\Gamma(\mu)}\exp\left[\mu\left(L-\log\langle I\rangle\right)-\exp\left(L-\log\langle I\rangle\right)\right]$$

$$\langle L\rangle = \log\langle I\rangle + \psi(\mu) - \log\mu$$

where ψ is Euler's Psi Function

$$\sigma_L^2 = \zeta(2,\mu)$$ = ***Riemann's Zeta Function***

Decibel Mean and Standard Deviation

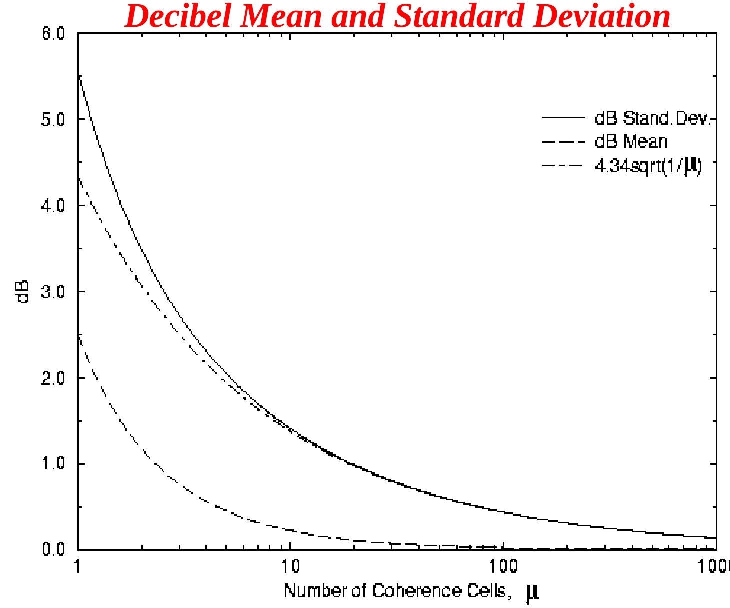

-Random Noise
-Transmission Scintillation
-Image Speckle Statistics

Passive OAWRS Sensing in Ocean Waveguide

Coherence Time (τ_c) Determines Number of Samples for Variance Reduction

Coherence Time Determines Coherent Processing Resolution Limits in Array Invariant, Matched Filter

Distributions of vocalizing humpback whales and spawning herring populations in Fall 2006 [1]

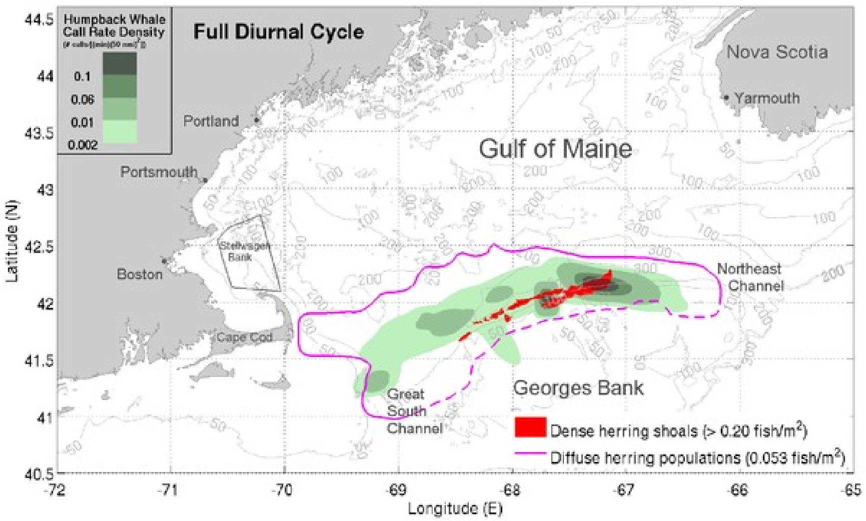

Full diel cycle distributions of marine mammal vocalizations and fish [2]

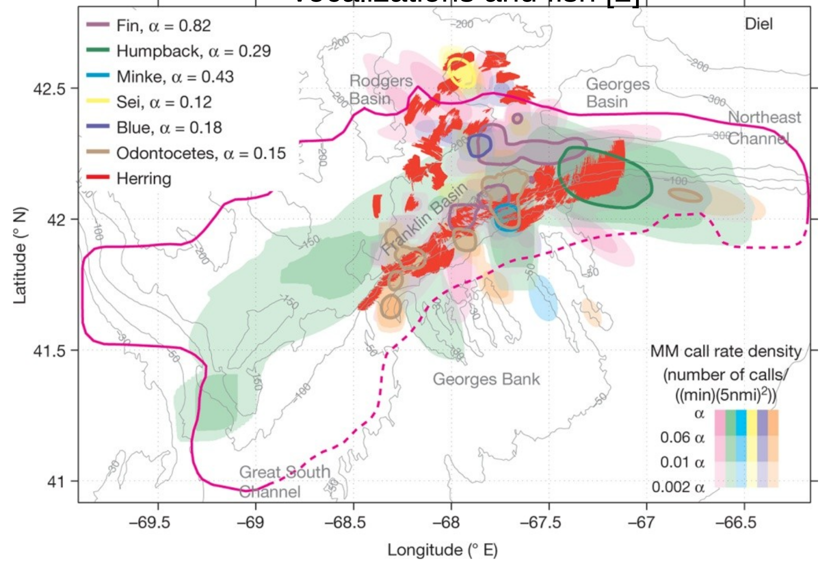

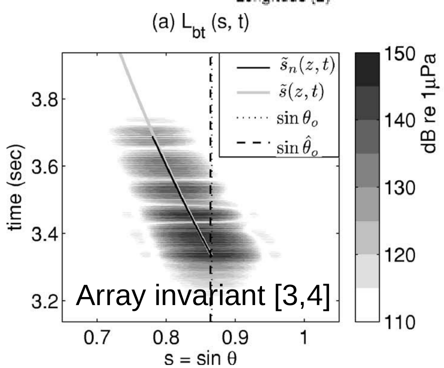

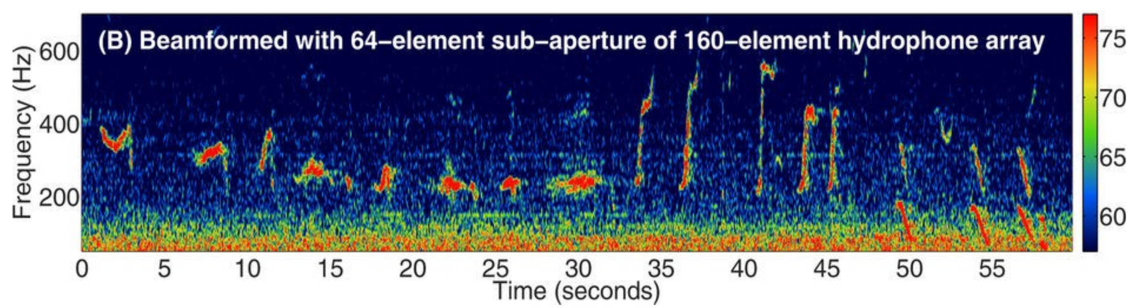

[1] Gong, Z., Jain, A.D., Tran, D., Yi, D.H., Wu, F., Zorn, A., Ratilal, P. and Makris, N.C., 2014. Ecosystem scale acoustic sensing reveals humpback whale behavior synchronous with herring spawning processes and re-evaluation finds no effect of sonar on humpback song occurrence in the Gulf of Maine in Fall 2006. PloS one, 9(10), p.e104733.

[2] Wang, D., Garcia, H., Huang, W., Tran, D.D., Jain, A.D., Yi, D.H., Gong, Z., Jech, J.M., Godø, O.R., Makris, N.C. and Ratilal, P., 2016. Vast assembly of vocal marine mammals from diverse species on fish spawning ground. Nature, 531(7594), p.366.

[3] Lee, S. and Makris, N.C., 2006. The array invariant. The Journal of the Acoustical Society of America, 119(1), pp.336-351.

[4] Gong, Z., Ratilal, P. and Makris, N.C., 2015. Simultaneous localization of multiple broadband non-impulsive acoustic sources in an ocean waveguide using the array invariant. The Journal of the Acoustical Society of America, 138(5), pp.2649-2667.

Underwater Communication Requires Temporal Coherence of the Acoustic Field in a Waveguide

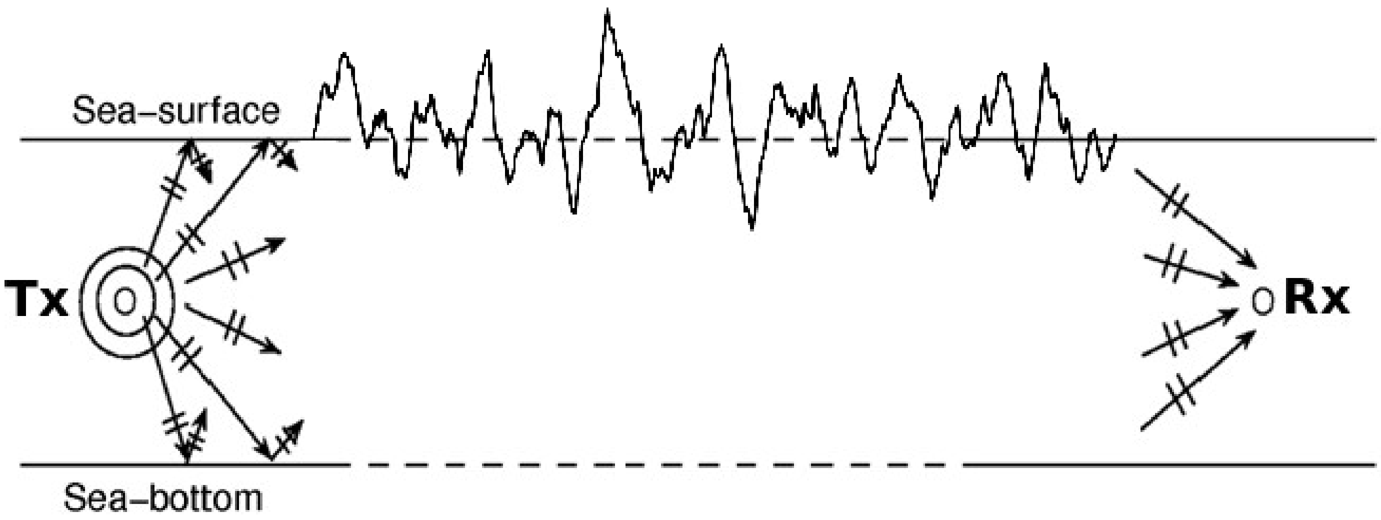

Estimation of channel coherence time is essential for efficient communication system design

- Temporal decorrelation of many time varying inhomogeneities is non-negligible at most operational frequencies
- Doppler shift and Doppler spread non-negligible at higher frequencies
- Temporal dispersion due to multi-modal propagation typically becomes an issue when range exceeds waveguide depth

Physical Processes Affecting Acoustic Propagation Through a Random Time Varying Ocean Waveguide

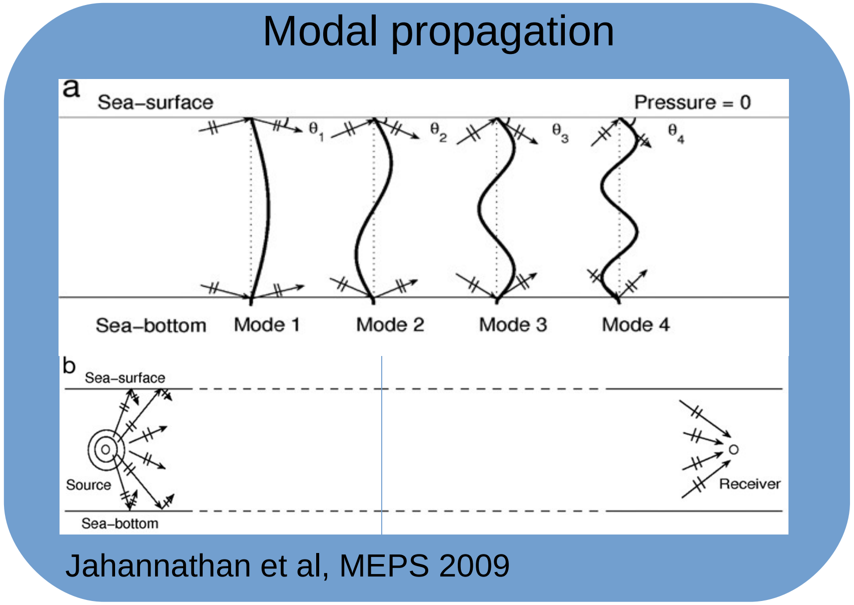

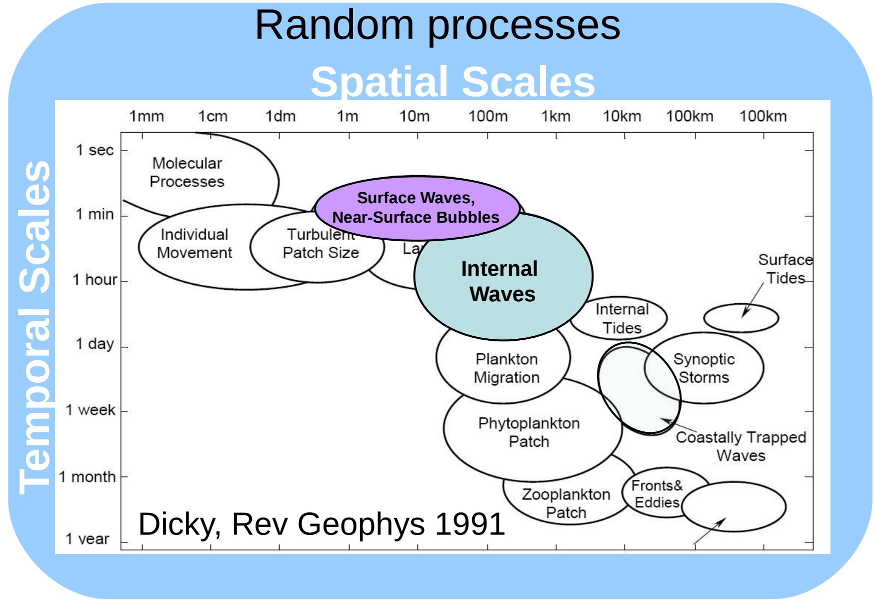

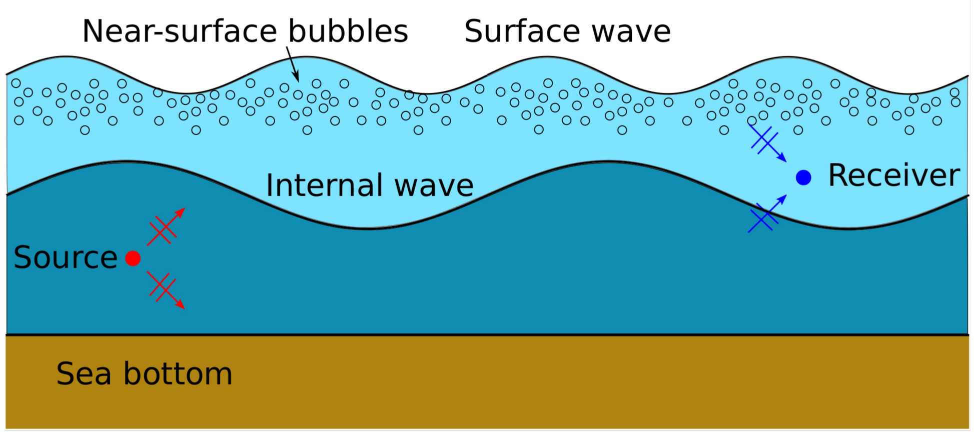

Stochastic Scattered Field from One Slab of Moving Inhomogeneities in a Waveguide

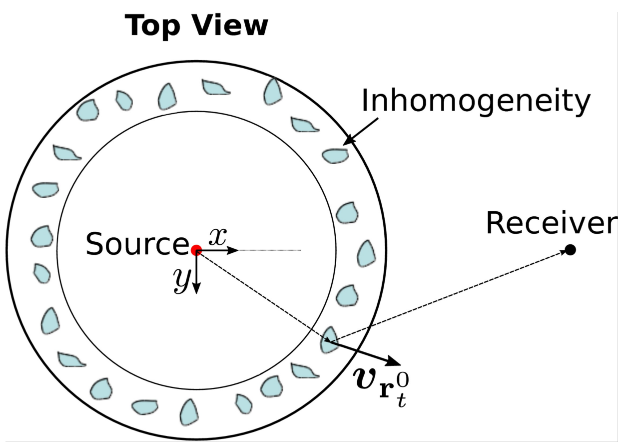

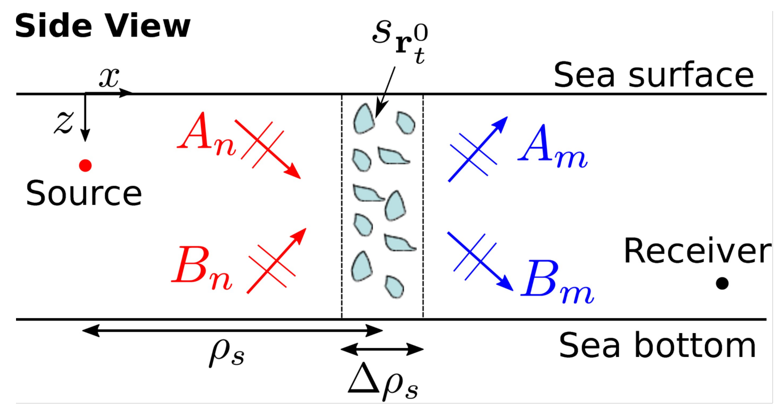

$$\Phi_s(\mathbf{r}|\mathbf{r}_0;\Delta\rho_s(\rho_s)) = \iiint_{\Delta V_s} d\mathbf{r}_t^0 \sum_n \sum_m e^{\;i\omega_{nm} t} \frac{(4\pi)^2}{k(\omega_{nm})}\left(1+\frac{v_{\mathbf{r}_t^0}}{C_m^g(\omega_{nm})}\cos\vartheta_{\mathbf{r}_t^0}\right)$$

Doppler effect enters here

$$\times \Big[A_n(\mathbf{r}_t^0-\mathbf{r}_0;\omega_i)\, s_{\mathbf{r}_t^0}\left(m_u(\omega_{nm}),\beta(\phi,\phi_{\mathbf{r}_t^0});n_d(\omega_i),\phi_{\mathbf{r}_t^0};\omega_{nm}\right) A_m(\mathbf{r}-\mathbf{r}_t^0;\omega_{nm})$$

$$- A_n(\mathbf{r}_t^0-\mathbf{r}_0;\omega_i)\, s_{\mathbf{r}_t^0}\left(m_d(\omega_{nm}),\beta(\phi,\phi_{\mathbf{r}_t^0});n_d(\omega_i),\phi_{\mathbf{r}_t^0};\omega_{nm}\right) B_m(\mathbf{r}-\mathbf{r}_t^0;\omega_{nm})$$

$$- B_n(\mathbf{r}_t^0-\mathbf{r}_0;\omega_i)\, s_{\mathbf{r}_t^0}\left(m_u(\omega_{nm}),\beta(\phi,\phi_{\mathbf{r}_t^0});n_u(\omega_i),\phi_{\mathbf{r}_t^0};\omega_{nm}\right) A_m(\mathbf{r}-\mathbf{r}_t^0;\omega_{nm})$$

$$+ B_n(\mathbf{r}_t^0-\mathbf{r}_0;\omega_i)\, s_{\mathbf{r}_t^0}\left(m_d(\omega_{nm}),\beta(\phi,\phi_{\mathbf{r}_t^0});n_u(\omega_i),\phi_{\mathbf{r}_t^0};\omega_{nm}\right) B_m(\mathbf{r}-\mathbf{r}_t^0;\omega_{nm})\Big]$$ [1-5]

Temporal correlation, strength of directional scatterers enters in $s_{\mathbf{r}_t^0}$ factors

[1] Ratilal, P. and Makris, N.C., 2005. Mean and covariance of the forward field propagated through a stratified ocean waveguide with three-dimensional random inhomogeneities. The Journal of the Acoustical Society of America, 118(6), pp.3532-3559.
[2] Chen, T., Ratilal, P. and Makris, N.C., 2005. Mean and variance of the forward field propagated through three-dimensional random internal waves in a continental-shelf waveguide. The Journal of the Acoustical Society of America, 118(6), pp.3560-3574.
[3] Chen, T., Ratilal, P. and Makris, N.C., 2008. Temporal coherence after multiple forward scattering through random three-dimensional inhomogeneities in an ocean waveguide. The Journal of the Acoustical Society of America, 124(5), pp.2812-2822.
[4] Gong, Z., Chen, T., Ratilal, P. and Makris, N.C., 2013. Temporal coherence of the acoustic field forward propagated through a continental shelf with random internal waves. The Journal of the Acoustical Society of America, 134(5), pp.3476-3485.
[5] Lai, Y.S. and Makris, N.C., 2003. Spectral and modal formulations for the Doppler-shifted field scattered by an object moving in a stratified medium. The Journal of the Acoustical Society of America, 113(1), pp.223-244.

Mean Forward Field Including Multiple Scattering Effect

Single scattering

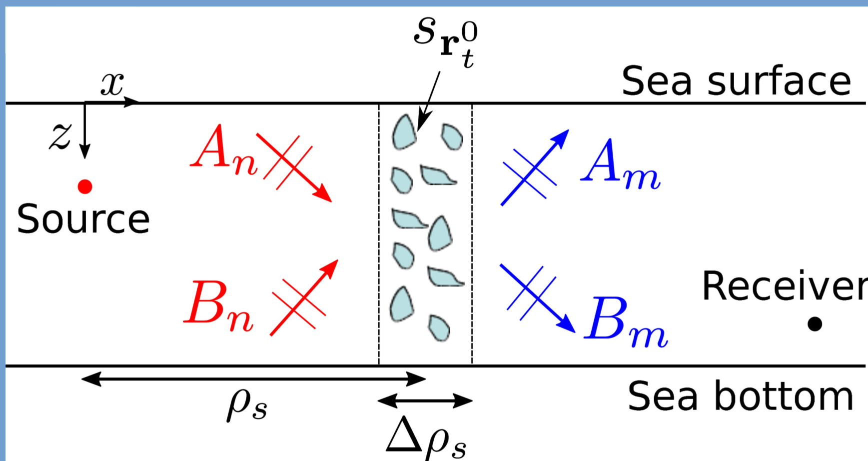

Multiple scattering by marching through differential slab elements

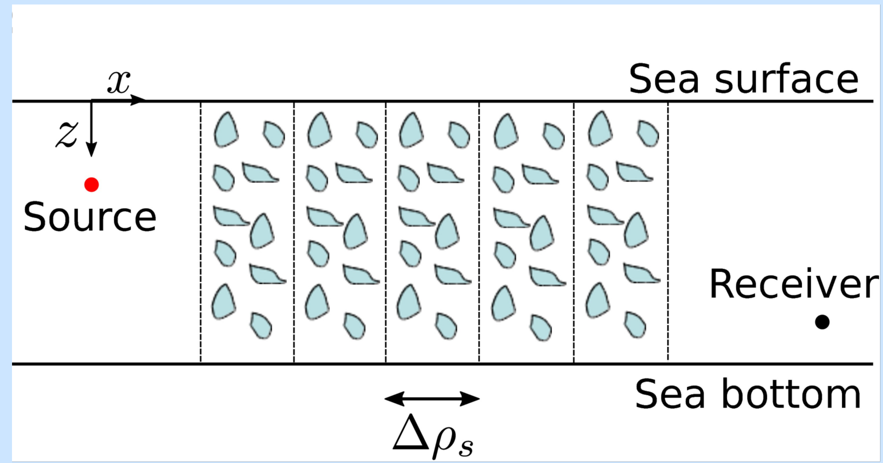

Difference equation

$$\langle \Phi_s^{(n)}(\mathbf{r}|\mathbf{r}_0; \Delta\rho_s(\rho_s))\rangle = \Delta\langle \Phi_T^{(n)}(\mathbf{r}|\mathbf{r}_0)\rangle = \langle \Phi_T^{(n)}(\mathbf{r}|\mathbf{r}_0)\rangle i\nu_n(\rho_s)\Delta\rho_s,$$

Integral equation

$$\int_{\psi_i^{(n)}}^{\langle\psi_T^{(n)}\rangle} \frac{d\langle \Phi_T^{(n)}(\mathbf{r}|\mathbf{r}_0)\rangle}{\langle \Phi_T^{(n)}(\mathbf{r}|\mathbf{r}_0)\rangle} = i\int_0^{\rho} \nu_n(\rho_s)d\rho_s,$$

Mean total field

$$\langle \Phi_T(\mathbf{r}|\mathbf{r}_0)\rangle = \sum_n \Phi_i^{(n)}(\mathbf{r}|\mathbf{r}_0)\, e^{i\int_0^{\rho}\nu_n(\rho_s)d\rho_s}$$ [1]

$\nu_n(\rho_s) \propto s_{\mathbf{r}_t^0}$: Modal complex wavenumber change → dispersion and attenuation

[1] Ratilal, P. and Makris, N.C., 2005. Mean and covariance of the forward field propagated through a stratified ocean waveguide with three-dimensional random inhomogeneities. The Journal of the Acoustical Society of America, 118(6), pp.3532-3559.

Spatial-Temporal Covariance of the Forward Field After Multiple Scattering Through a Random Waveguide

- Temporal correlation of the forward field

$$\mathrm{Corr}_{\Phi_T,\Phi_T}(\mathbf{r},\tau|\mathbf{r}_0) = \langle \Phi_T(\mathbf{r},t|\mathbf{r}_0)\Phi_T^*(\mathbf{r},t'|\mathbf{r}_0)\rangle$$

$$= \sum_n \left|\Phi_i^{(n)}(\mathbf{r}|\mathbf{r}_0)\right|^2 e^{\int_0^\rho 2\Im\{\nu_n(\rho_s)\}d\rho_s} e^{\int_0^\rho \mu_n(\rho_s,\tau)d\rho_s}$$

Attenuation in the forward field due to scattering

Temporal correlation of inhomogeneities affect acoustic temporal correlation through this factor

- Doppler effects are not included in the previous work [1-4]. Doppler effects by moving inhomogeneities are now included in $\nu_n(\rho_s)$ and $\mu_n(\rho_s,\tau)$, and shown to be important at high frequencies.

- $\nu_n(\rho_s)$ and $\mu_n(\rho_s,\tau)$ are expressed in terms of the first two statistical moments of scatter function density of inhomogeneities
    - Surface waves: Small slope approximation ← Pierson-Moskowitz sea surface spectrum
    - Internal waves: Rayleigh-Born approximation ← Garret-Munk internal wave spectrum in shallow water
    - Air bubbles near surface: Damped-forced oscillator ←Measured bubble size spectrum and spatial distribution

[1] Ratilal, P. and Makris, N.C., 2005. Mean and covariance of the forward field propagated through a stratified ocean waveguide with three-dimensional random inhomogeneities. The Journal of the Acoustical Society of America, 118(6), pp.3532-3559.

[2] Chen, T., Ratilal, P. and Makris, N.C., 2005. Mean and variance of the forward field propagated through three-dimensional random internal waves in a continental-shelf waveguide. The Journal of the Acoustical Society of America, 118(6), pp.3560-3574.

[3] Chen, T., Ratilal, P. and Makris, N.C., 2008. Temporal coherence after multiple forward scattering through random three-dimensional inhomogeneities in an ocean waveguide. The Journal of the Acoustical Society of America, 124(5), pp.2812-2822.

[4] Gong, Z., Chen, T., Ratilal, P. and Makris, N.C., 2013. Temporal coherence of the acoustic field forward propagated through a continental shelf with random internal waves. The Journal of the Acoustical Society of America, 134(5), pp.3476-3485.

2D Vs 3D scattering effect on the forward field

Fresnel width or active region:

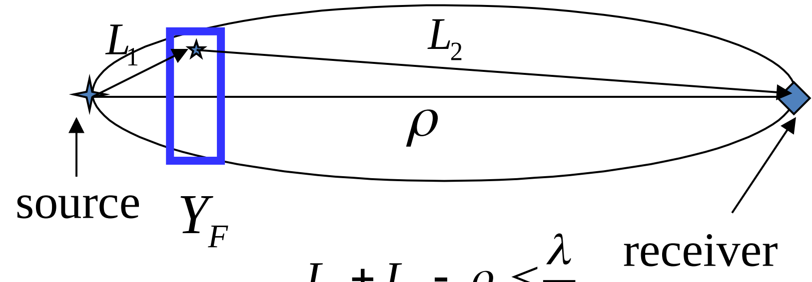

$$Y_F(\rho,\rho_s) \approx \sqrt{\frac{\lambda(\rho - \rho_s)\rho_s}{\rho}} \qquad Y_F(\rho,\rho/2) = \sqrt{\frac{\lambda\rho}{4}}$$

$$L_1 + L_2 - \rho \leq \frac{\lambda}{8}$$

2D scattering is applicable when $L_y > Y_F$

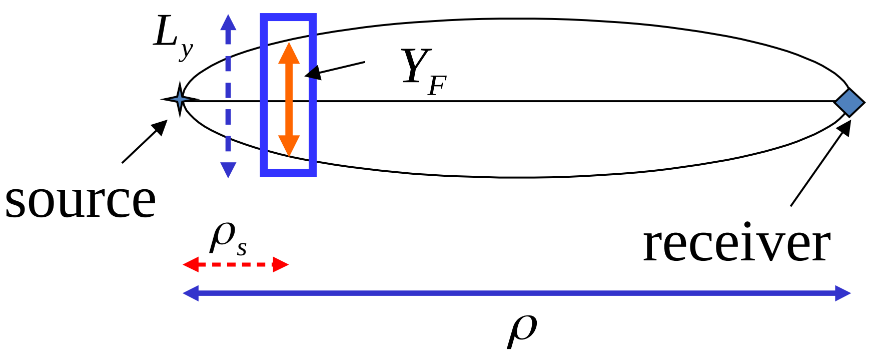

3D scattering is necessary when $L_y < Y_F$

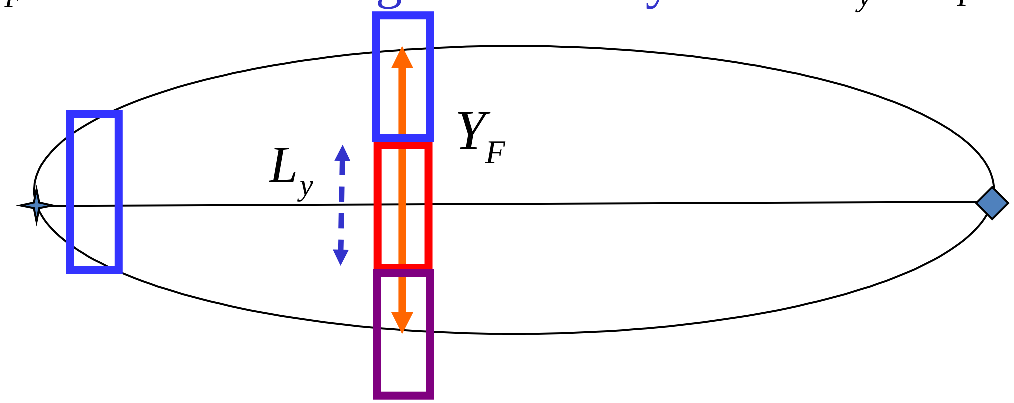

For acoustic frequency 415Hz and Ly=100m,

when source and receiver separation is 11km

$$Y_F = L_y$$

Previous results
Attenuation, Dispersion, Randomization
Internal waves in continental shelf
Classic Two Layer Ocean

Chen, Ratilal and Makris JASA 2005

Chen, Ratilal and Makris JASA 2005

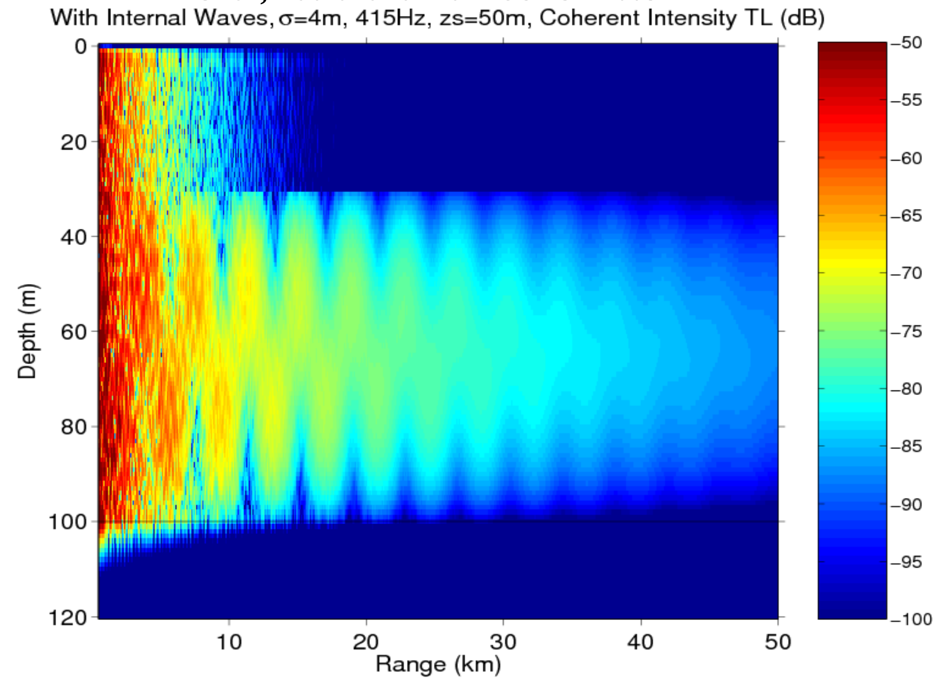

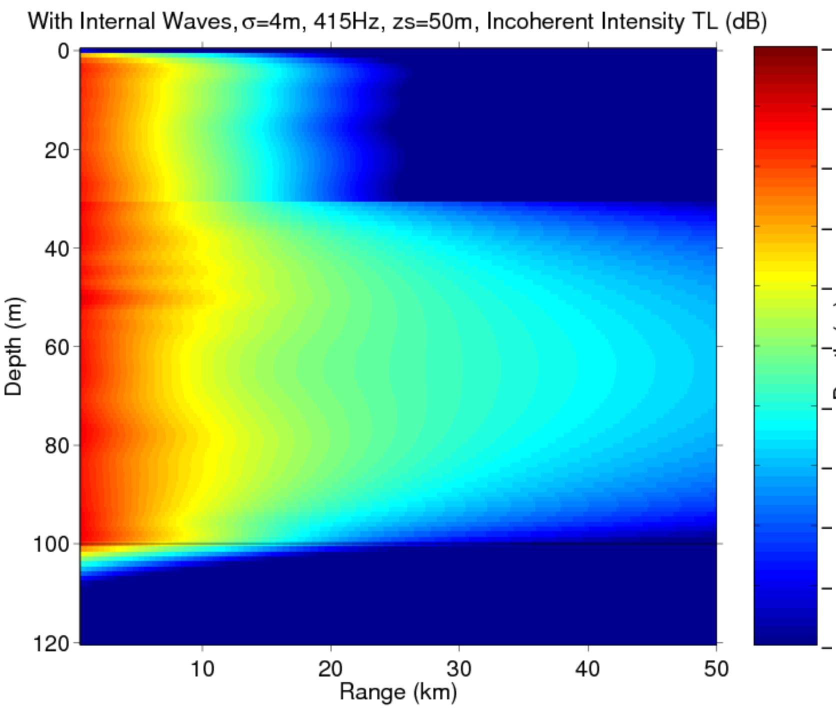

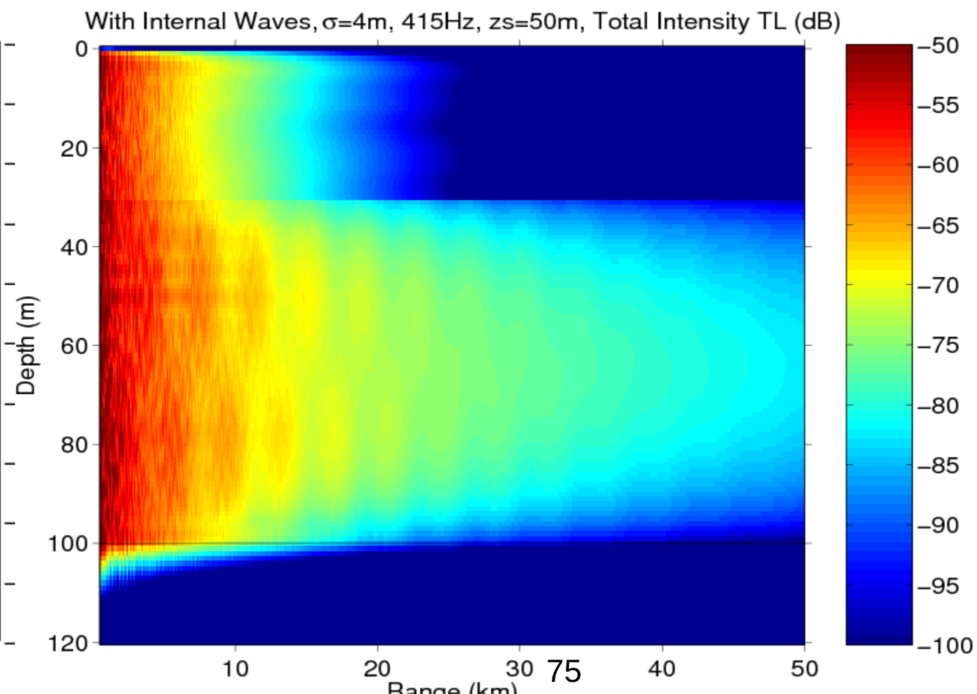

Previous Deep Ocean Results

Total acoustic power loss and temporal coherence after long range propagation through random internal waves

Chen, Ratilal and Makris JASA 2008

Deep Ocean Temporal coherence of internal waves

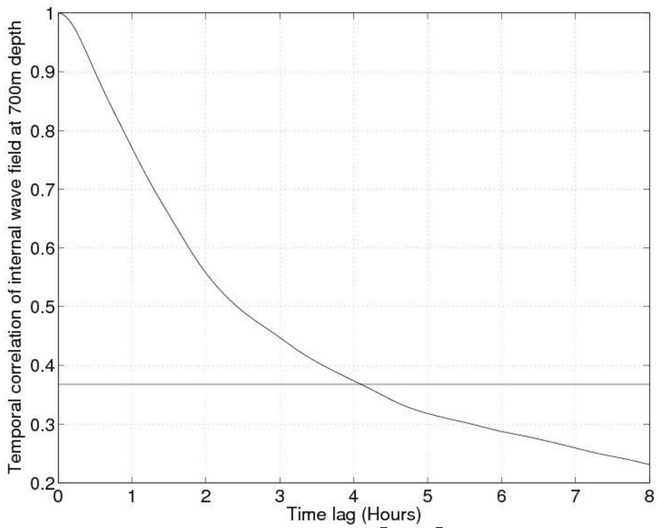

Acoustic Power Loss in Forward Propagation Consistent with classic measurements

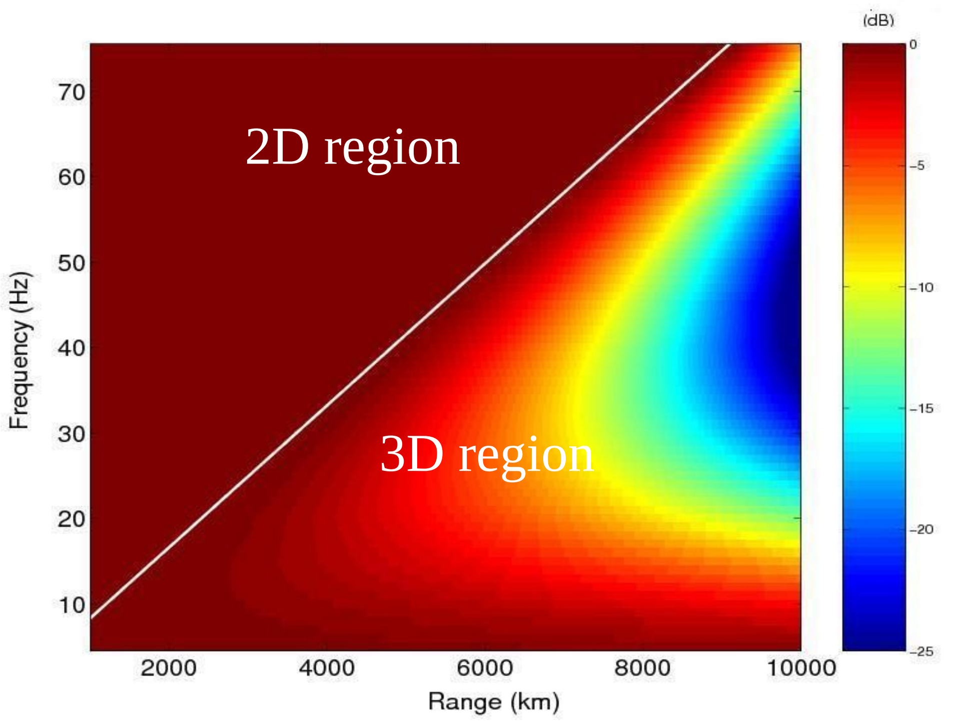

Deep Ocean Temporal coherence of acoustic field matches measurements

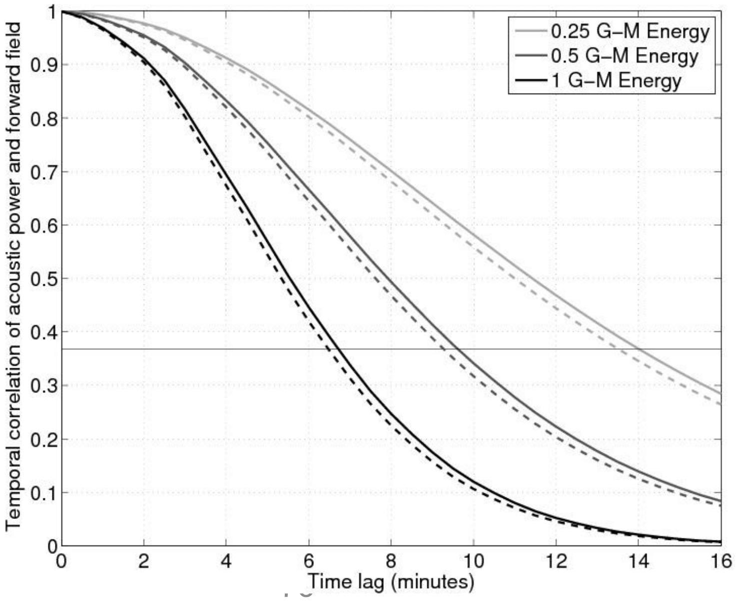

Previous Results: Power-law Range Dependence of Acoustic Temporal Coherence in *Continental-Shelf* Environments Matches Measurements

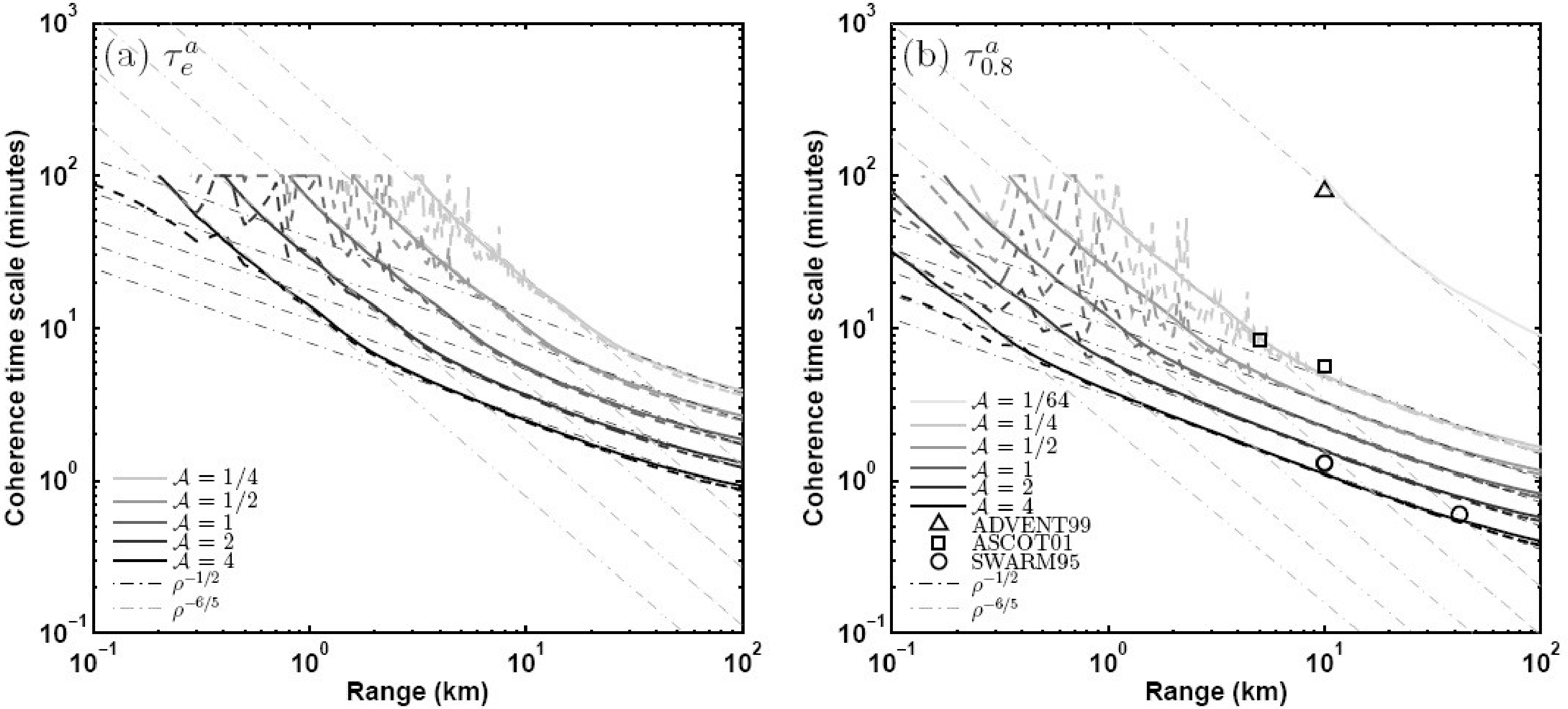

- Both E-folding t_e and $t_{0.8}$ follow a power-law of range to the -1/2 beyond moderate propagation ranges, which is consistent with the theory and measured data for both deep-ocean and shallow water environments.
- Simulation results fit well with a power-law of range to the -6/5 at short ranges
- Both the coherence time scale and the transitional range are inversely proportional to the internal wave energy level.

Z. Gong, T. Chen, P. Ratilal, and N. Makris. "Temporal coherence of the acoustic field forward propagated through a continental shelf with random internal waves," JASA, 134, 3476-3485, 2013.

Modeling Wind Generated Rough Sea Surface

- Scattered field by surface roughness is the scattered field by a rough surface subtracted by the scattered field by a flat surface
  - Mean surface roughness = 0 implies mean scattered field by surface roughness = 0.
  - Second moment of the bistatic scatter function density of surface roughness is calculated using small slope approximation of Voronovich

$$\sigma_{\mathrm{SSA}} = \frac{k_{sz}^2 k_{iz}^2}{(\pi V_z)^2} e^{-(V_z h_{\mathrm{rms}})^2} \iint d\mathbf{r}\; e^{i(\boldsymbol{\xi_i} - \boldsymbol{\xi_s})\cdot\mathbf{r}} \left(e^{(V_z h_{\mathrm{rms}})^2 R(\mathbf{r})} - 1\right)$$

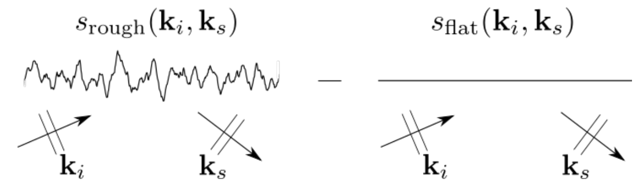

$\mathbf{V} = \mathbf{k_i} \quad \mathbf{k_s}$: Difference between incident and scattered wavenumber vectors

$\mathbf{k_i} = (\boldsymbol{\xi_i}, k_{iz})$: Incident wavenumber vector

$\mathbf{k_s} = (\boldsymbol{\xi_s}, k_{sz})$: Scattered wavenumber vector

$R(\mathbf{r})$: 2-D spatial correlation coefficient function of sea surface height

h_{rms}: Rms sea surface height

- Modal temporal covariance coefficient for surface inhomogeneities

$$\mu_n(\rho_s, \tau) = \sum_m \frac{1}{\xi_m} \left(1 + \frac{\bar{v}}{C_m^g}\right)^2 \frac{l_x(\rho_s)}{\xi_m} \frac{4\pi^2}{k(0)^2 d(0)^2} (1 + i\Re\{\xi_n \quad \xi_m\}\bar{v}\tau)\, C_{s,s}(\rho_s, m, n, \tau)$$

Complicated linear combination of covariances of surface scatter function density over double modal sum

Input to our model: Temporal covariance of bistatic scatter function density for surface roughness

$$\sigma_{\mathrm{SSA}}(m,n)R(\tau) = A_c \frac{\mathrm{Cov}_{s,s}(m,n,\tau)}{k(0)^2} \;\Rightarrow\; \mathrm{Cov}_{s,s}(m,n,\tau) = \frac{k(0)^2}{A_c}\sigma_{\mathrm{SSA}}(m,n)R(\tau)$$

Bistatic scattering cross section per unit area for surface roughness

Temporal correlation coefficient function of sea surface height

Coherence area of sea surface height

Modeling Wind Generated Rough Sea Surface

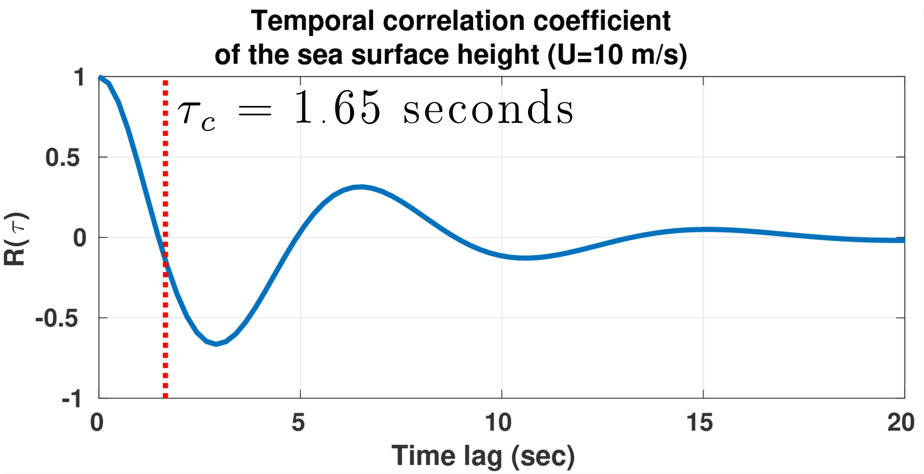

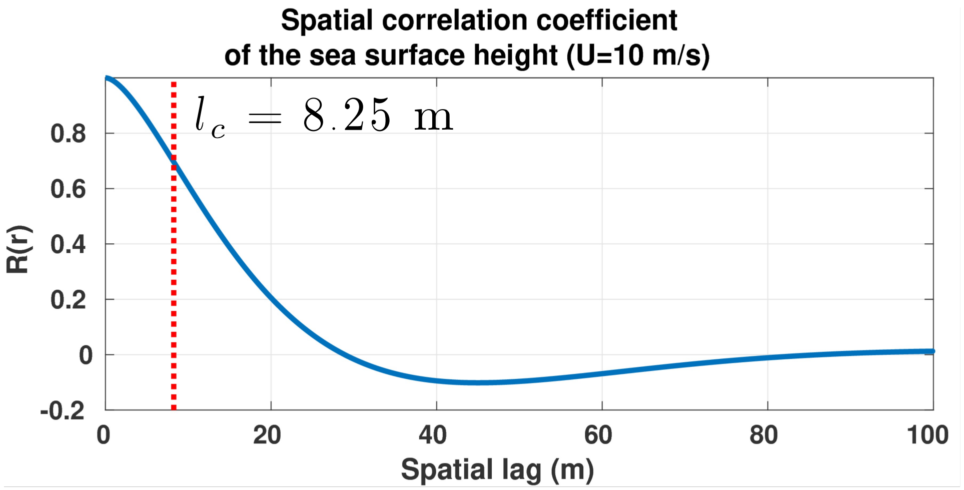

- Scattered field by surface roughness
  - Scattered field from a rough surface subtracted by scattered field from a flat surface
  - Modeled by small slope approximation
- Temporal and spatial coherent scales are calculated from Pierson-Moskowitz sea spectrum
- Much shorter coherent time scales than internal waves
- Much smaller coherent spatial scales than internal waves

Modeling Internal Waves

- Scatter function density of internal waves (Rayleigh-Born approximation)

$$s_{\mathbf{r}_t^0, t_t} = \frac{1}{A_c} \iint_{A_c} d\mathbf{u} e^{i(\boldsymbol{\xi}_i - \boldsymbol{\xi}) \cdot \mathbf{u}} \frac{k^3}{4\pi} \left[\Gamma_\kappa \left(\mathbf{u}, z_t^0, t_t \right) + \eta \left(\mathbf{k}, \mathbf{k_i} \right) \Gamma_d \left(\mathbf{u}, z_t^0, t_t \right) \right]$$ [1]

$\Gamma_\kappa \left(\mathbf{r}_t^0, t_t \right) \propto h \left(\mathbf{r}_t^0, t_t \right)$: Fractional compressibility difference

$\Gamma_d \left(\mathbf{r}_t^0, t_t \right) \propto h \left(\mathbf{r}_t^0, t_t \right)$: Fractional density difference

$h \left(\mathbf{r}_t^0, t_t \right)$: Waveheight of internal waves

$\eta \left(\mathbf{k}, \mathbf{k_i} \right)$: Cosine of angle between incident and scattered plane waves

- Modal temporal covariance coefficient for volume inhomogeneities

$$\mu_n(\rho_s, \tau) \propto \mathrm{Cov}_{s,s} \left(m, n, z_t^0, z_{t'}^0, \tau \right) \propto \mathrm{Cov}_{h,h} \left(z_t^0, z_{t'}^0, \tau \right)$$

$$\mathrm{Cov}_{h,h}(z_t^0, z_{t'}^0, \tau) = \sum_{j=1}^{J} \int_{-\infty}^{\infty} d^2k \ F_j \left(k^2 \right) W_j \left(k^2, z_t^0 \right) W_j \left(k^2, z_{t'}^0 \right) e^{-i\omega(k)\tau}$$

Garret-Munk internal wave spectrum modified to be consistent in continental shelf data (Yang and Yoo, IEEE 1999)

Internal wave mode function

[1] Chen, T., Ratilal, P. and Makris, N.C., 2005. Mean and variance of the forward field propagated through three-dimensional random internal waves in a continental-shelf waveguide. The Journal of the Acoustical Society of America, 118(6), pp.3560-3574.

Modeling Internal Waves

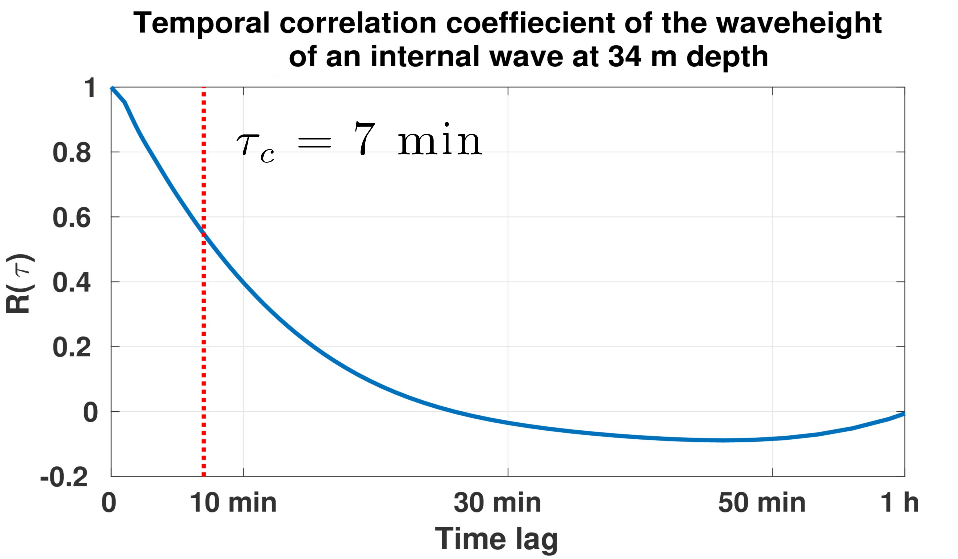

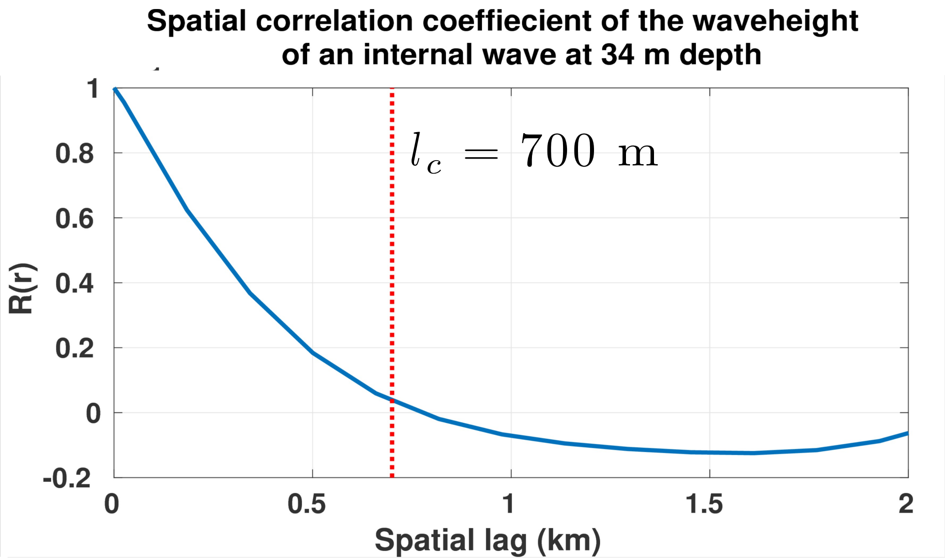

- Gravity waves that propagate through stratified density layers within water column
- Scatter function density is modeled by Rayleigh-Born approximation [1]
- Temporal and spatial coherent scales are calculated from Garret-Munk internal wave spectrum in shallow water (Yang and Yoo, IEEE 1999).
- Much longer coherent time scales than surface waves
- Much larger coherent spatial scales than surface waves

[1] Chen, T., Ratilal, P. and Makris, N.C., 2005. Mean and variance of the forward field propagated through three-dimensional random internal waves in a continental-shelf waveguide. The Journal of the Acoustical Society of America, 118(6), pp.3560-3574.

Modeling Near Surface Air Bubbles

- Scatter function of an air bubble is modeled as a damped-forced oscillator

$$S = \frac{ka\left(\frac{\omega_0^2}{\omega^2} - 1\right)}{\left(\frac{\omega_0^2}{\omega^2} - 1\right)^2 + \delta_{\text{tot}}^2} + i\frac{\delta_{\text{tot}}ka}{\left(\frac{\omega_0^2}{\omega^2} - 1\right)^2 + \delta_{\text{tot}}^2}$$

- Volume number density is calculated from measured bubble size spectrum $\mathrm{n_v} = \int n(a)da$

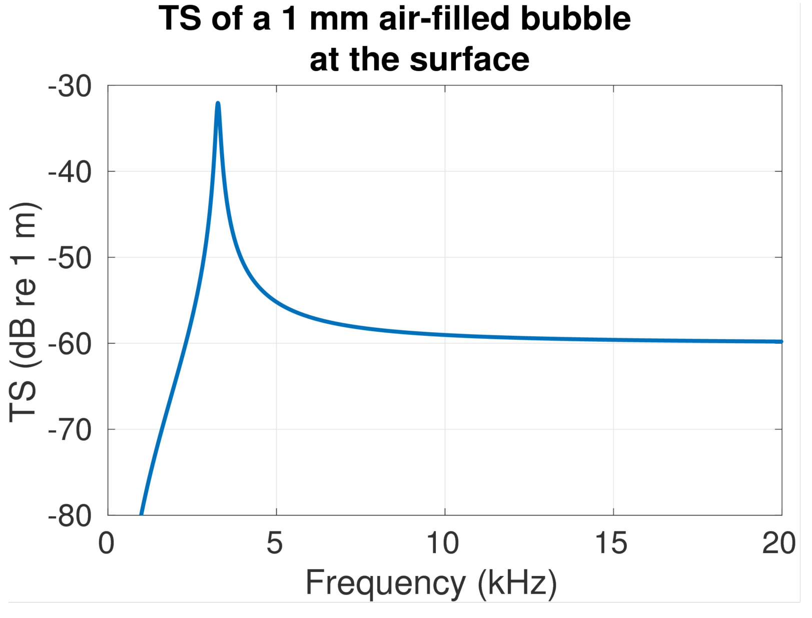

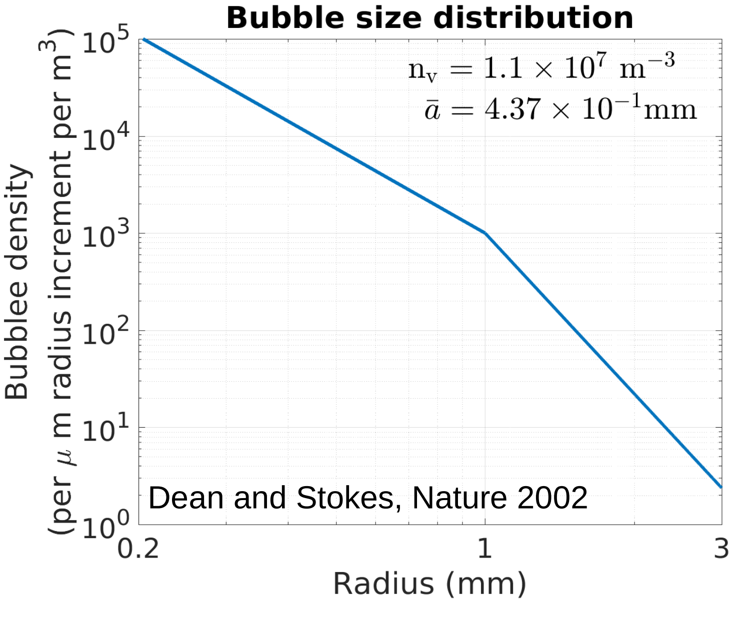

Example for Long Range Remote Sensing Applications: Comparison with Barents Sea, Low Frequency Data

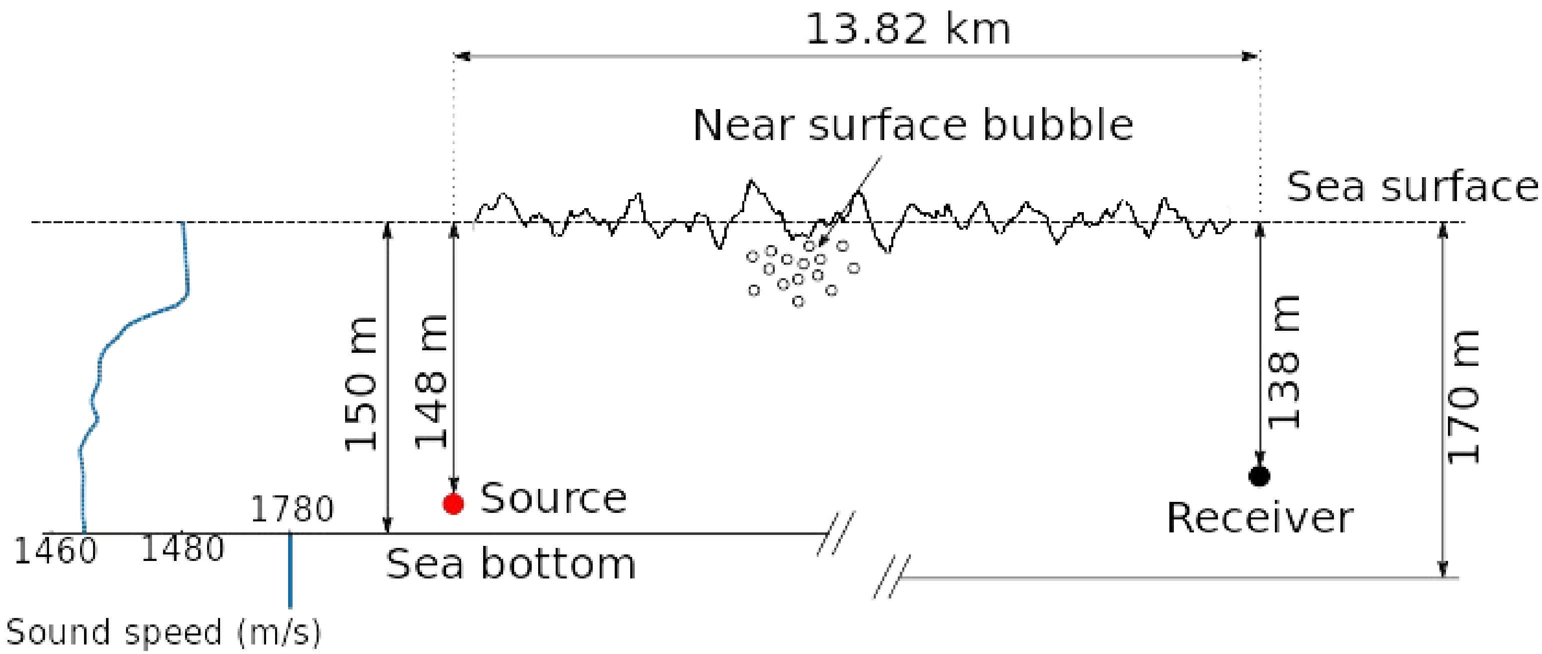

- Site: Barents Sea in October 1990 (Sazontov et al, IEEE OE 2002)
- Wind speed: 8-12 m/s (Sea state 4 - 5)
- Source: Generated a CW wave at 240 Hz
- Receiver: 30 minute recording

Analytic Acoustic Model Accurately Matches Data Requiring Only Three Parameters: Wind speed, bubble number density and internal wave energy, constrained by measurement

Transition Between Mechanisms of Temporal Decorrelation

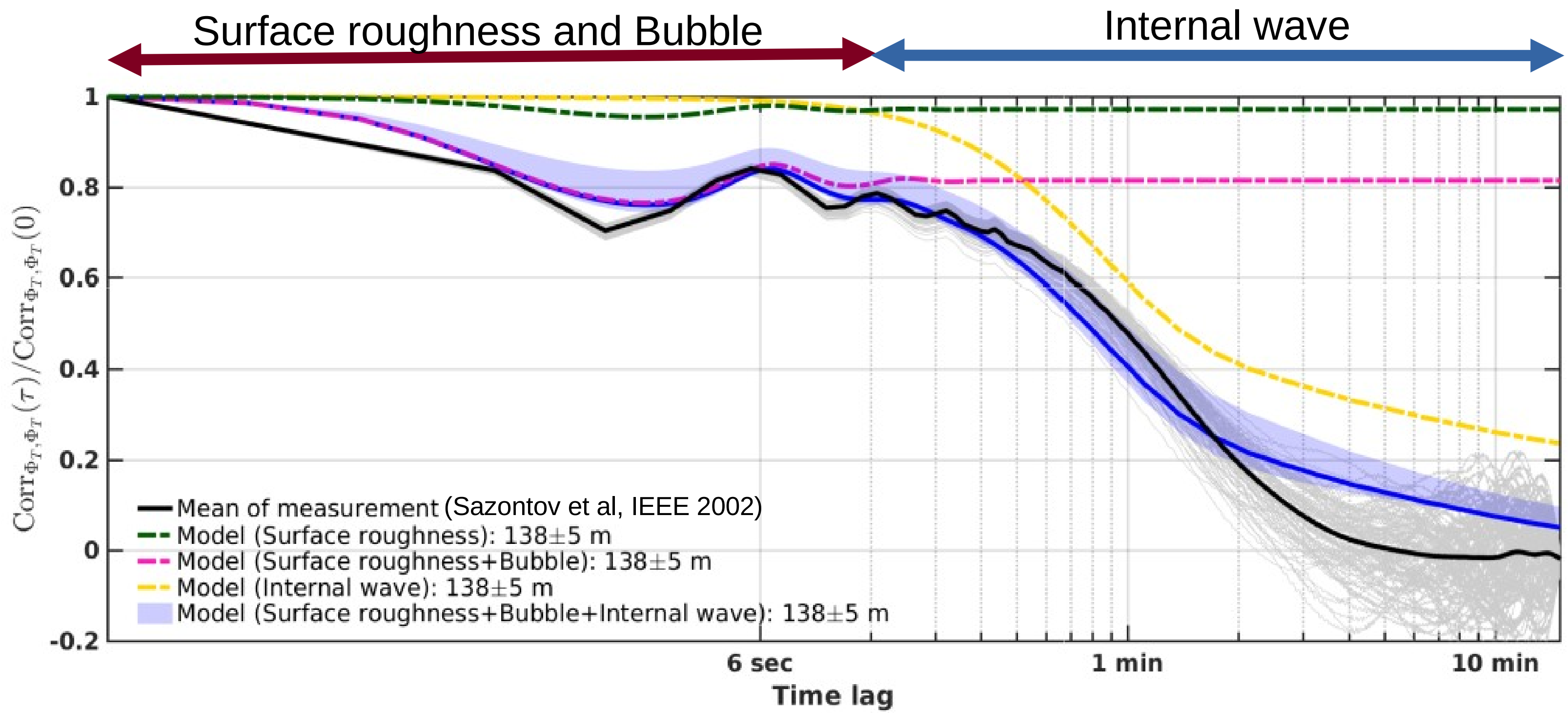

- Bubble volume number density ($n_V = 1.1 \times 10^7 \mathrm{m}^{-3}$)
- Internal wave energy density (E_0 = 250 J/m^2)
- Wind speed U = 10 m/s

Example for Underwater Communication Applications: Comparison with Gulf of Mexico, High Frequency Data

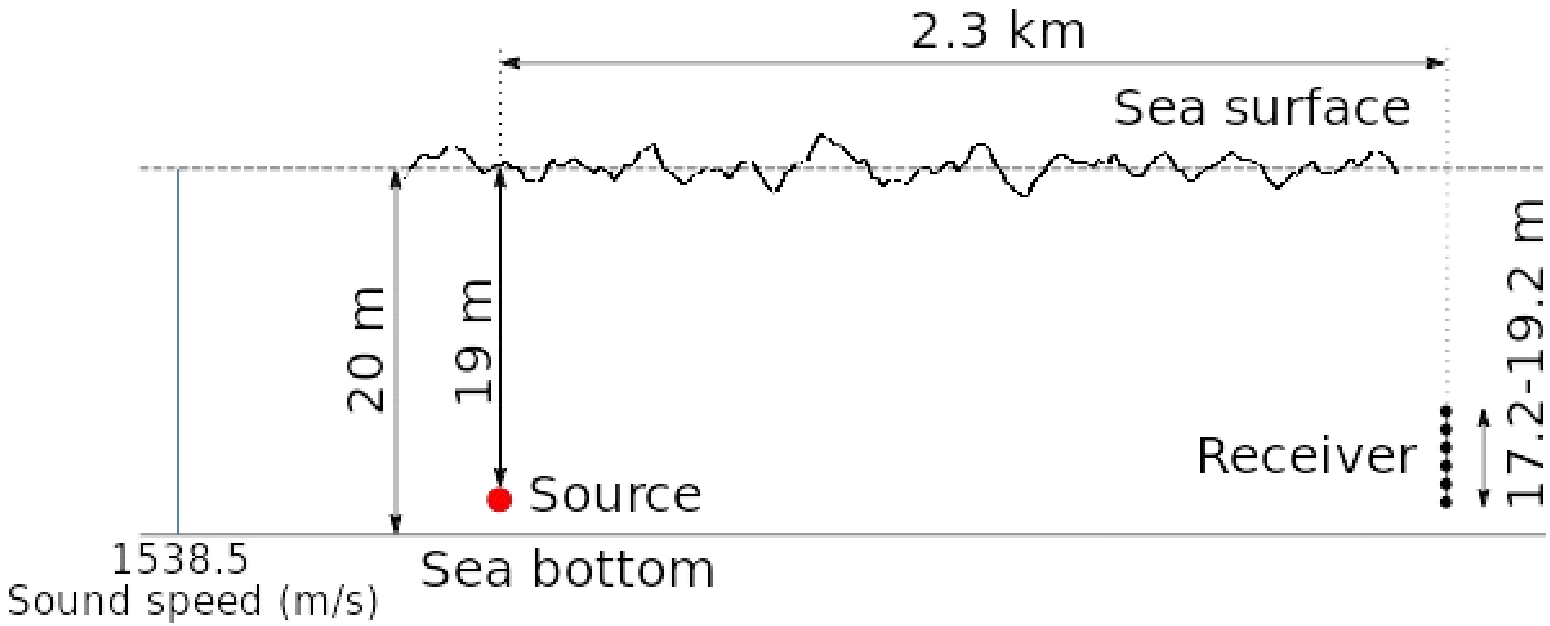

- Site: Coastal Waters of Gulf of Mexico (Yang, JASA 2012)
- Wind speed: 4-6 m/s

➡ negligible near-surface bubble effect

- Constant sound speed profile, shallow water depth

➡ negligible internal wave effect

- Source: Generated 25 second signal at 17±2 kHz

Analytical Acoustic Model Accurately Matches Data Requiring Only Two Parameters:

Wind speed and Mean Phase Velocity of Surface Waves

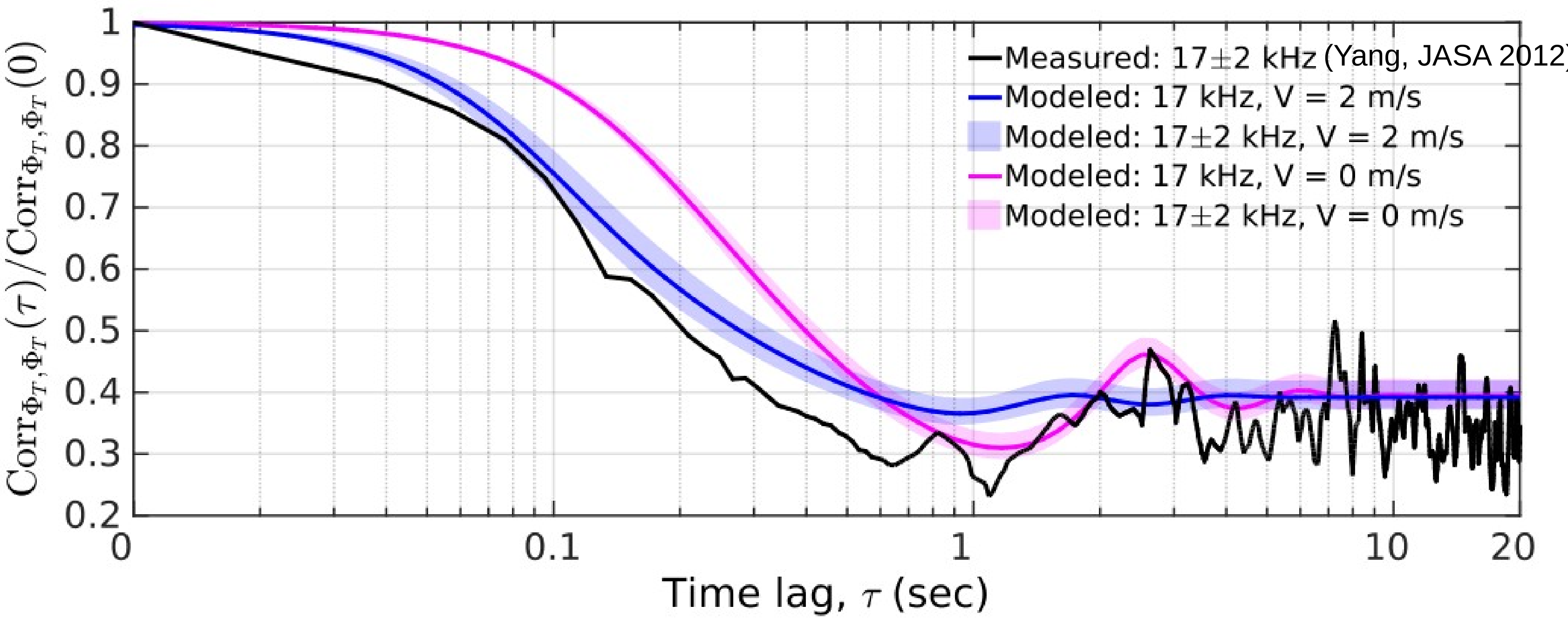

- Pierson-Moskowitz isotropic ocean wave spectrum at wind speed, U = 5 m/s
- Mean phase velocity of the surface waves, V = 2 m/s
- Doppler effect shortens the acoustic temporal coherence at typical underwater communication frequencies

Conclusions

Derived general analytical expressions: Mean and temporal covariance of the acoustic forward field through an ocean waveguide with moving random inhomogeneities that includes Doppler shift and spread, as a function of sea state, bubble density and internal wave energy.

Applied to surface and volume scatterers: Rough sea surface, bubbles, internal waves

Good agreement between modeled and measured temporal coherence of the acoustic forward field

Discovered transitions between temporal decorrelation mechanisms and showed that they are related to different phenomena, surface waves, bubbles and internal waves.

The model can be broadly used in sensing and communication applications in the ocean

Active Nonlinear Acoustic Sensing of an Object with Sum or Difference Frequency Fields

Nonlinear Interaction of Sound with Objects

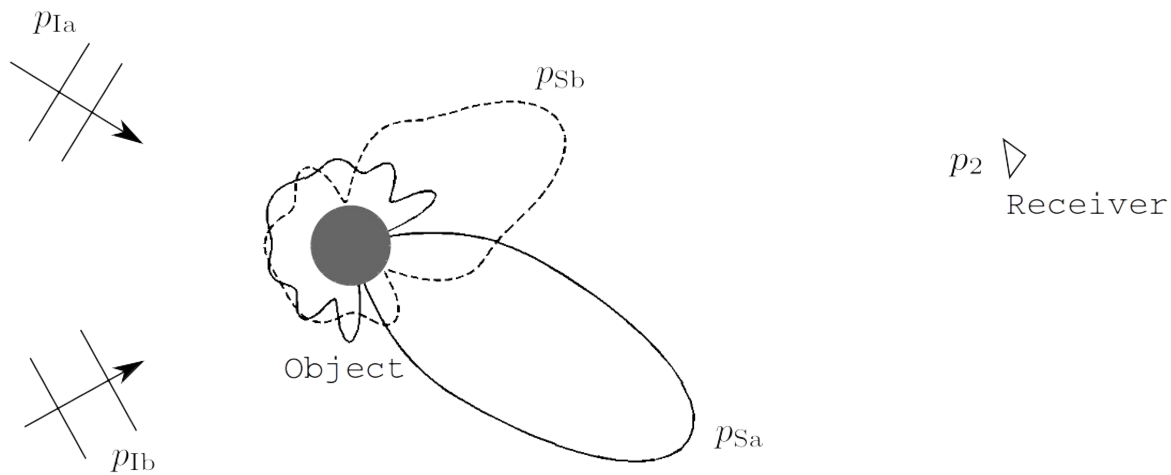

- Two incident waves $$p_{\mathrm{I1}} = p_{\mathrm{Ia}} + p_{\mathrm{Ib}}$$
- Two scattered waves $$p_{\mathrm{S1}} = p_{\mathrm{Sa}} + p_{\mathrm{Sb}}$$
- Total first order field $$p_1 = p_{\mathrm{Ia}} + p_{\mathrm{Ib}} + p_{\mathrm{Sa}} + p_{\mathrm{Sb}}$$

- Incident-incident (II), Scattered-Scattered (SS), Incident-Scattered (IS), Scattered-Incident (SI) interactions
- Second order scattering (S2)
- Total second order field $$p_2 = p_{\mathrm{II}} + p_{\mathrm{SS}} + p_{\mathrm{IS}} + p_{\mathrm{SI}} + p_{\mathrm{S2}}$$

Frequency Response Information about the Object

$$p_2 = p_{\mathrm{II}} + p_{\mathrm{SS}} + p_{\mathrm{IS}} + p_{\mathrm{SI}} + p_{\mathrm{S2}}$$

- p_{SS}, p_{IS}, and p_{SI} contain primary frequency response information about the object
- p_{S2} contains sum and difference frequency response information about the object
- p_{II} contains no information about the object
- A complete theory is necessary to understand the behavior of different mechanisms and to interpret the measurements

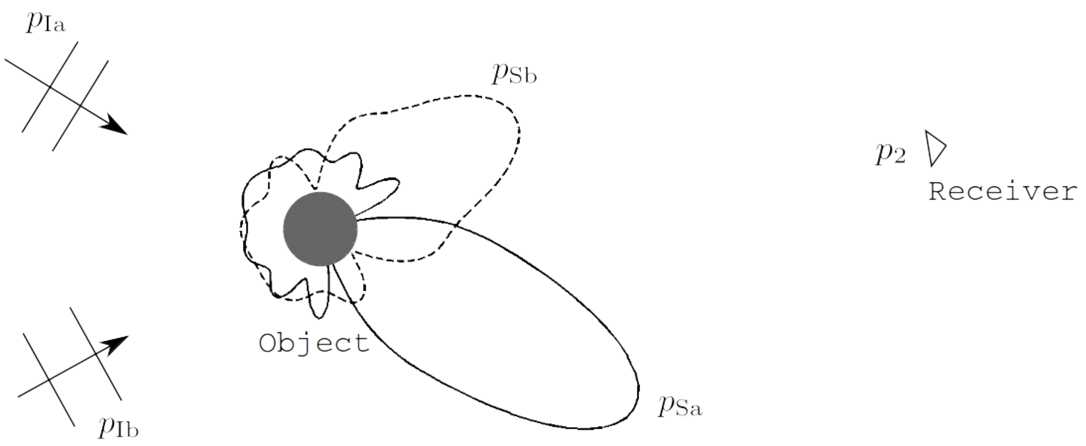

Total Second Order Field

Total second order field $p_2 = p_{\mathrm{I2}} + p_{\mathrm{S2}}$

Second order incident field p_{I2}

Governing equation $\left(\nabla^2 - \frac{1}{c_0^2}\frac{\partial^2}{\partial t^2}\right) p_{\mathrm{I2}} = -\rho_0 \left[\frac{1}{\rho_0^2 c_0^4}\frac{B}{2A}\frac{\partial^2 p_1^2}{\partial t^2} + \nabla \cdot \nabla \cdot (\mathbf{v}_1 \mathbf{v}_1)\right]$

Sommerfeld radiation condition

Includes II, SS, IS and SI interactions $p_{\mathrm{I2}} = p_{\mathrm{II}} + p_{\mathrm{SS}} + p_{\mathrm{IS}} + p_{\mathrm{SI}}$

Independent of the second order boundary condition on the object

Second order scattered field p_{S2}

Governing equation $\left(\nabla^2 - \frac{1}{c_0^2}\frac{\partial^2}{\partial t^2}\right) p_{\mathrm{S2}} = 0$

Sommerfeld radiation condition

Depend on second order boundary condition

- Pressure release : $p_{\mathrm{S2}} = -p_{\mathrm{I2}} - \xi_1 \cdot \nabla p_1$
- Rigid immovable : $\mathrm{v}_{\mathrm{S2}} \cdot \mathbf{n} = -\mathbf{v}_{\mathrm{I2}} \cdot \mathbf{n}$
- Rigid movable : $\mathbf{v}_{\mathrm{S2}} \cdot \mathbf{n} = -\mathbf{v}_{\mathrm{I2}} \cdot \mathbf{n} - \xi_1 \cdot \nabla(\mathbf{v}_1 \cdot \mathbf{n}) + \mathbf{u}_2 \cdot \mathbf{n}$

Confirmation of the Theory with Experiment

- Jones and Beyer (1971)
- Good quantitative agreement between measurement and theory
  - 0.98 correlation coefficient
  - 0.3 dB mean square error
- Wave-wave SS mechanism is confirmed dominant

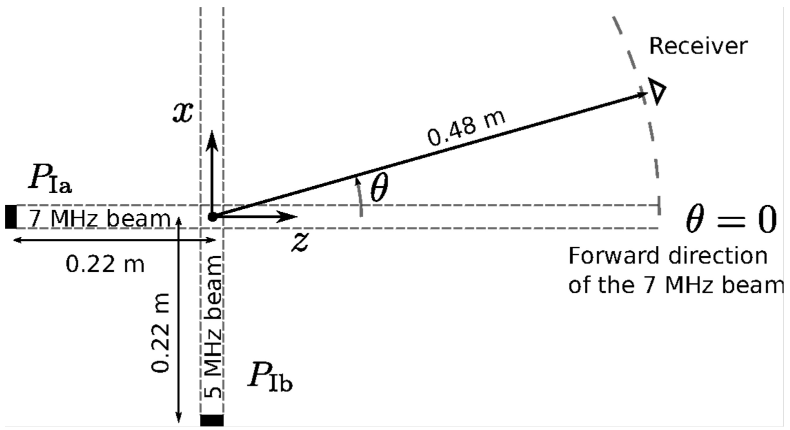

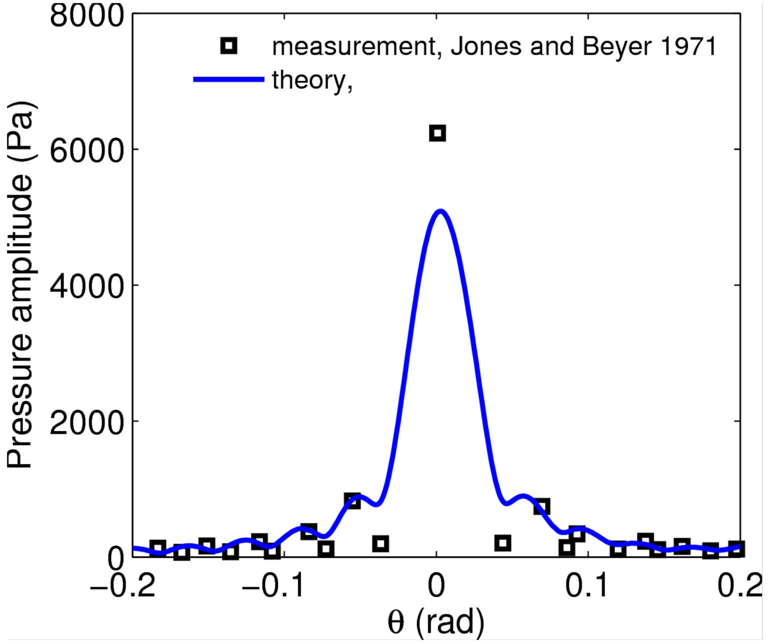

- Primary frequencies: $f_a = 7\ \mathrm{MHz},\ f_b = 5\ \mathrm{MHz}$
- Steel sphere of radius a = 0.3175 cm displaced at the center of the interaction region in water $(k_a a = 93.1\ ,\ k_b a = 66.5,\ k_+ a = 159.6)$

- Theory done by finite difference computation
- Mismatch with measurement due to limited information about transducer

Analytic Solutions for the Wave-Wave Interaction:
Incident-Incident Interaction of Plane Waves of General Time Dependence

- Incident-incident interaction of collinear plane waves of general time dependence

$$
\begin{aligned}
p_{\mathrm{II},ab^{(*)}}(z,t) = {} & \Re\left\{\frac{\beta z}{2Ac_0}\frac{\partial}{\partial t}\left[\tilde{p}_{\mathrm{Ia}}(t \quad z/c_0)\tilde{p}_{\mathrm{Ib}}^{(*)}(t \quad z/c_0)\right]\right\} \\
& - \Re\left\{\frac{1}{2A}\tilde{p}_{\mathrm{Ia}}(t-z/c_0)\tilde{p}_{\mathrm{Ib}}^{(*)}(t-z/c_0)\right\} \\
& \quad \Re\left\{\frac{1}{2A}\left(\frac{\partial}{\partial t}\tilde{p}_{\mathrm{Ia}}(t \quad z/c_0)\right)\int_{\infty}^{t \quad z/c_0}\tilde{p}_{\mathrm{Ib}}^{(*)}(\tau)d\tau\right\} \\
& - \Re\left\{\frac{1}{2A}\left(\frac{\partial}{\partial t}\tilde{p}_{\mathrm{Ib}}^{(*)}(t-z/c_0)\right)\int_{\infty}^{t-z/c_0}\tilde{p}_{\mathrm{Ia}}(\tau)d\tau\right\},
\end{aligned}
$$

Incident-incident interaction of non-collinear plane waves of general time dependence

$$
\begin{aligned}
p_{\mathrm{II},ab^{(*)}}(x,z',t) = {} & \Re\left\{\frac{1}{2A}\left[\frac{\beta}{1 \quad \cos\theta}-1\right]\left[\frac{\partial}{\partial t}\tilde{p}_{\mathrm{Ib}}^{(*)}(t-z'/c_0)\right]\left[\int_{\infty}^{t-x/c_0}\tilde{p}_{\mathrm{Ia}}(\tau)d\tau\right]\right\} \\
& + \Re\left\{\frac{1}{2A}\left[\frac{\beta}{1 \quad \cos\theta}-1\right]\left[\frac{\partial}{\partial t}\tilde{p}_{\mathrm{Ia}}(t-x/c_0)\right]\left[\int_{\infty}^{t \quad z'/c_0}\tilde{p}_{\mathrm{Ib}}^{(*)}(\tau)d\tau\right]\right\} \\
& + \Re\left\{\frac{1}{2A}\left[\frac{2\beta}{1 \quad \cos\theta} \quad (1+\cos\theta)\right]\tilde{p}_{\mathrm{Ia}}(t \quad x/c_0)\tilde{p}_{\mathrm{Ib}}^{(*)}(t \quad z'/c_0)\right\},
\end{aligned}
$$

Analytic Solutions for the Wave-Wave Interaction: Incident-Incident Interaction of Time-Windowed Narrow-Band Plane Waves Helps Resolve Half-Century Old Debate about “Scattering of Sound by Sound”

- Collinear

$$p_{\mathrm{II},ab^{(*)}}(z,t) \approx \Re\left\{ \quad \frac{P_{a0}P_{b0}^{(*)}}{2A}\left[\mathrm{i}\beta k_\pm z \pm \frac{\omega_\pm^2}{\omega_a\omega_b}\right] e^{\mathrm{i}(k_\pm z \quad \omega_\pm t)}\right\} w_1^2(t \quad z/c_0),$$

- Non-collinear

$$p_{\mathrm{II},ab^{(*)}}(x,z',t) \approx \Re\left\{ \frac{P_{a0}P_{b0}^{(*)}}{2A}\left[\pm\left(1 \quad \frac{\beta}{\cos\theta} \quad 1\right)\frac{\omega_\pm^2}{\omega_a\omega_b} + 1 \quad \cos\theta\right] e^{\mathrm{i}(k_a x \pm k_b z' - \omega_\pm t)}\right\}$$
$$\times\, w_1(t \quad x/c_0)\, w_1(t \quad z'/c_0),$$

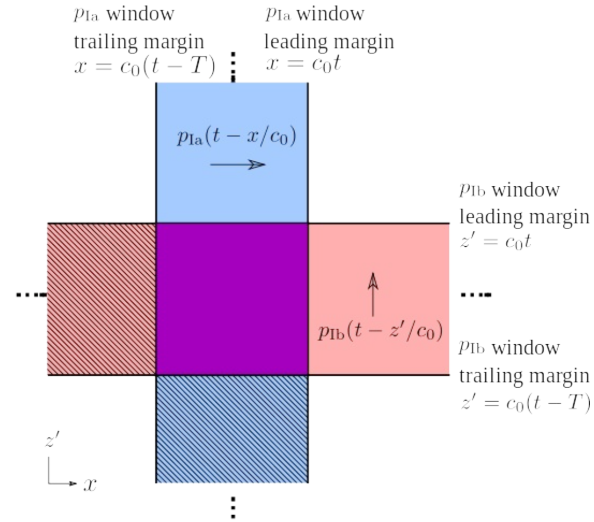

(a) Difference frequency

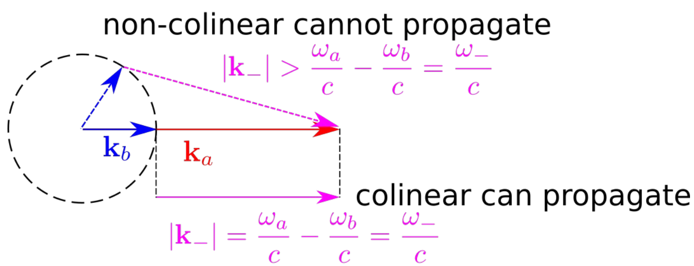

(b) Sum frequency

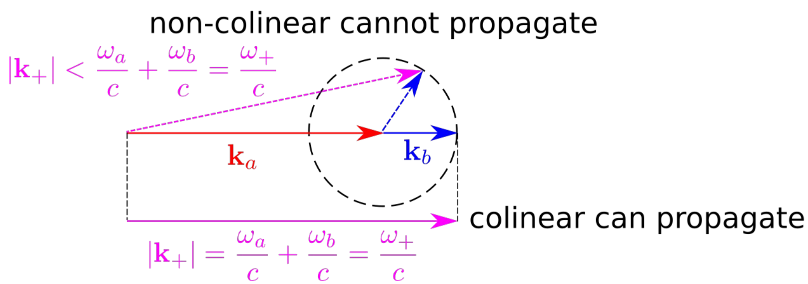

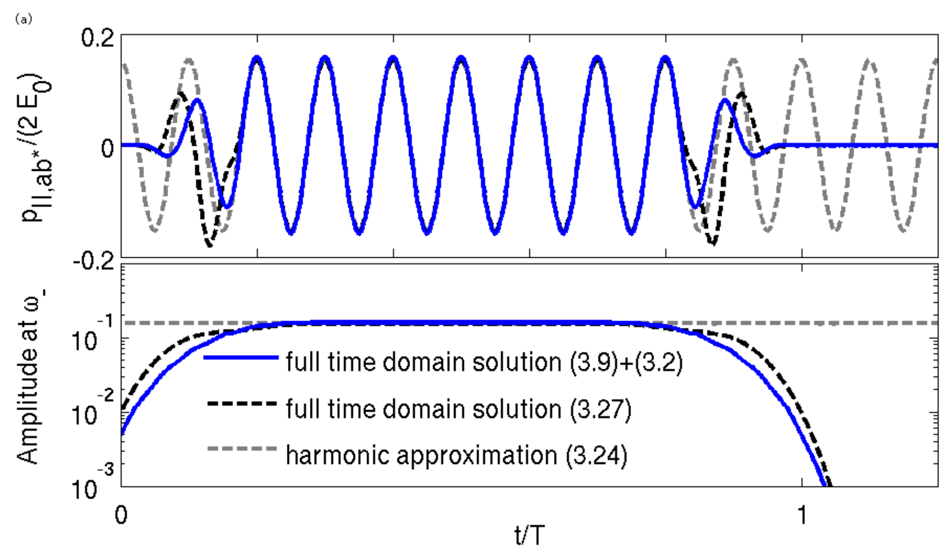

Analytic Solutions for the Wave-Wave Interaction: Scattered-Scattered and Incident-Scattered Interaction

- Far field primary scattered fields

$$P_{\mathrm{Sa}}(\mathbf{r}) = P_{a0}\frac{S_a(\hat{\mathbf{i}}_r)}{k_a}\frac{e^{\mathrm{i}k_a r}}{r} \quad , \quad P_{\mathrm{Sb}}(\mathbf{r}) = P_{b0}\frac{S_b(\hat{\mathbf{i}}_r)}{k_b}\frac{e^{\mathrm{i}k_b r}}{r},$$

- Far field scattered-scattered interaction

$$P_{\mathrm{SS}\pm}(\mathbf{r}) \approx P'_{\mathrm{SS}\pm}(\mathbf{r}) \approx P'^{(2)}_{\mathrm{SS}\pm}(\mathbf{r}) \approx \frac{\omega_\pm^2 \beta P_{a0} P_{b0}^{(*)}}{2\mathrm{i}Ac_0^2 k_a k_b}\frac{e^{\mathrm{i}k_\pm r}}{k_\pm r}\log\left(\frac{r}{r_{\mathrm{ref}\pm}}\right) S_a(\hat{\mathbf{i}}_r) S_b^{(*)}(\hat{\mathbf{i}}_r),$$

- Far field incident-scattered interaction

$$P_{\mathrm{IS}+}(r\hat{\mathbf{i}}_a) \approx P'_{\mathrm{IS}+}(r\hat{\mathbf{i}}_a) \approx \frac{\omega_+^2 \beta P_{a0} P_{b0}}{Ac_0^2}\frac{e^{\mathrm{i}k_+ r}}{2k_a k_b}\left[\mathrm{i}\log\left(\frac{k_+}{k_b}\right)\right] S_b(\hat{\mathbf{i}}_a),$$

$$P_{\mathrm{IS}}\ \ (r\hat{\mathbf{i}}_a) \approx P'_{\mathrm{IS}}\ \ (r\hat{\mathbf{i}}_a) \approx \frac{\omega^2\ \beta P_{a0} P_{b0}^{*}}{Ac_0^2}\frac{e^{\mathrm{i}k\ \ r}}{2k_a k_b}\left[\mathrm{i}\log\left(\frac{k_-}{k_b}\right) + \pi\right] S_b^{*}(\hat{\mathbf{i}}_a),$$

$$P_{\mathrm{SI}\pm}(r\hat{\mathbf{i}}_b) \approx P'_{\mathrm{SI}\pm}(r\hat{\mathbf{i}}_b) \approx \frac{\omega_\pm^2 \beta P_{a0} P_{b0}^{(*)}}{Ac_0^2}\frac{e^{\mathrm{i}k_\pm r}}{2k_a k_b}\left[\pm\mathrm{i}\log\left(\frac{k_\pm}{k_a}\right)\right] S_a(\hat{\mathbf{i}}_b).$$

Analytic Solutions for the Second Order Scattered Field

- Compact gas-filled object or bubble

$$P_{S2\pm}(r) \approx \frac{P_{a0}P_{b0}^{(*)}A_{\text{res}}^{\pm}}{2\rho_0 c_0^2 (k_\pm a)} \left[-\left(\frac{\pm\omega_\pm^2}{\omega_a\omega_b} + \frac{\omega_\pm^2}{\omega_a^2} + \frac{\omega_\pm^2}{\omega_b^2} \right) + B_{\text{res}}^{\pm} \frac{\omega_\pm^2}{\omega_a\omega_b} \right] \frac{e^{ik_\pm r}}{k_\pm r},$$

where,

$$A_{\text{res}}^{\pm} = \alpha(\omega_a)\alpha(\omega_b)\alpha(\omega_\pm) \qquad B_{\text{res}}^{\pm} = \frac{3\gamma(p_0 + \frac{2\sigma}{a})(3\gamma+1) \quad \frac{4\sigma}{a}}{\rho_0 c_0^2 (k_a a)(k_b a)} \quad i\frac{\delta\omega_0\omega_\pm}{\omega_a\omega_b}.$$

For a pressure release object, $A_{\text{res}}^{\pm} = 1 \text{ and } B_{\text{res}}^{\pm} = 0$

- Ratio of wave-wave to second order scattered field for compact object or bubble

$$\frac{P_{SS\pm}}{P_{S2\pm}} = \frac{\beta}{\alpha(\omega_\pm)}(k_a a)(k_b a)(k_\pm a)\left[\pm 1 + \frac{\omega_b}{\omega_a} + \frac{\omega_a}{\omega_b} + B_{\text{res}}^{\pm}\right]^{1} \log\left(\frac{r}{r_{\text{ref}\pm}}\right)$$

$$\frac{P_{IS+}}{P_{S2+}} = \beta\left[1 + \frac{\omega_b}{\omega_a} + \frac{\omega_a}{\omega_b} + B_{\text{res}}^{\pm}\right]^{1} \log\left(\frac{k_+}{k_b}\right)\frac{(k_b a)(k_+ a)(k_+ r)}{\alpha(\omega_a)\alpha(\omega_+)}$$

$$\frac{P_{IS-}}{P_{S2}} = \beta\left[\quad 1 + \frac{\omega_b}{\omega_a} + \frac{\omega_a}{\omega_b} + B_{\text{res}}^{\pm}\right]^{1} i\log\left(\frac{k_-}{k_b}\right) + \pi \frac{(k_b a)(k_- a)(k_- r)}{\alpha(\omega_a)\alpha(\omega\ \ )}$$

$$\frac{P_{SI\pm}}{P_{S2\pm}} = \beta\left[\pm 1 + \frac{\omega_b}{\omega_a} + \frac{\omega_a}{\omega_b} + B_{\text{res}}^{\pm}\right]^{1} \log\left(\frac{k_\pm}{k_a}\right)\frac{(k_a a)(k_\pm a)(k_\pm r)}{\alpha(\omega_b)\alpha(\omega_\pm)}$$

Sensing Resonant Air Bubble In Water Transition Between Dominant 2nd Order Mechanisms

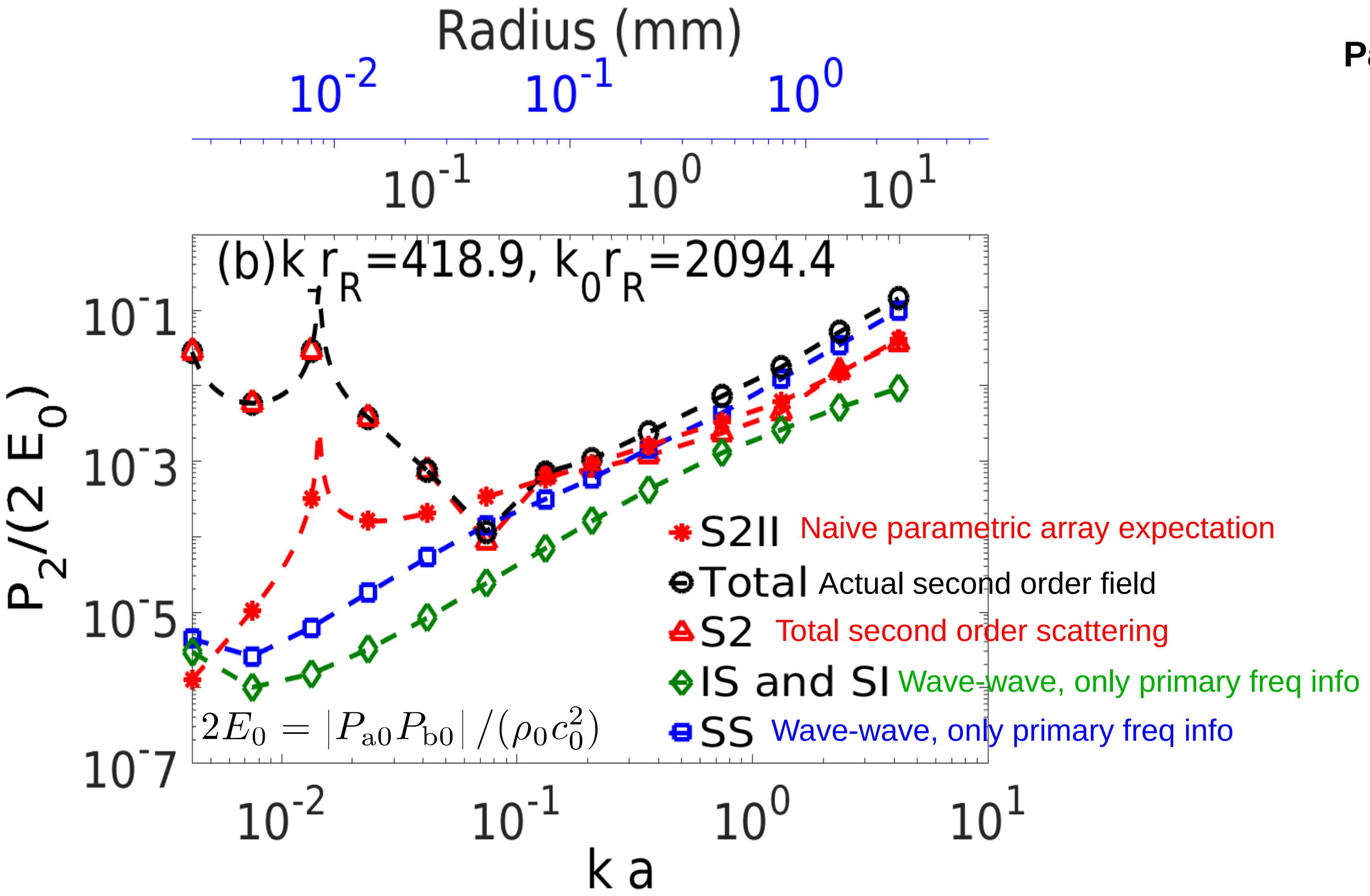

Parametric array scenario

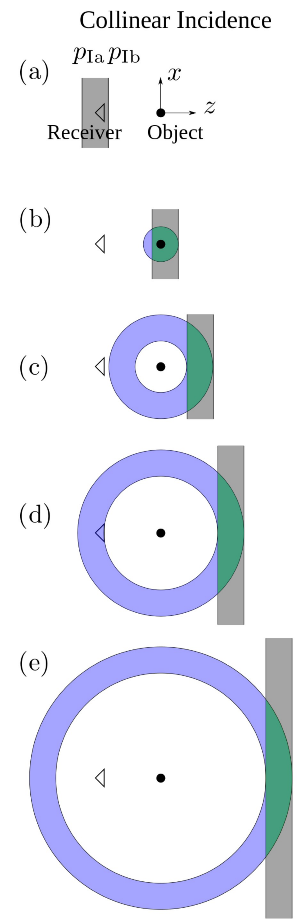

- Upper black abscissa: Second order pressure field measured at 1 m away from a 0.1 mm radius gas bubble in water, where primary and difference frequencies are respectively 1 MHz and 100 kHz. Upper blue abscissa: Second order pressure field measured at 0.25 m away from a 0.1 mm radius bubble in water, where primary and difference frequencies are respectively 2 MHz and 400 kHz.

- Typical assumption of linear scattering of incident parametric array diff freq field is in great error (S2II).

Rigid Sphere

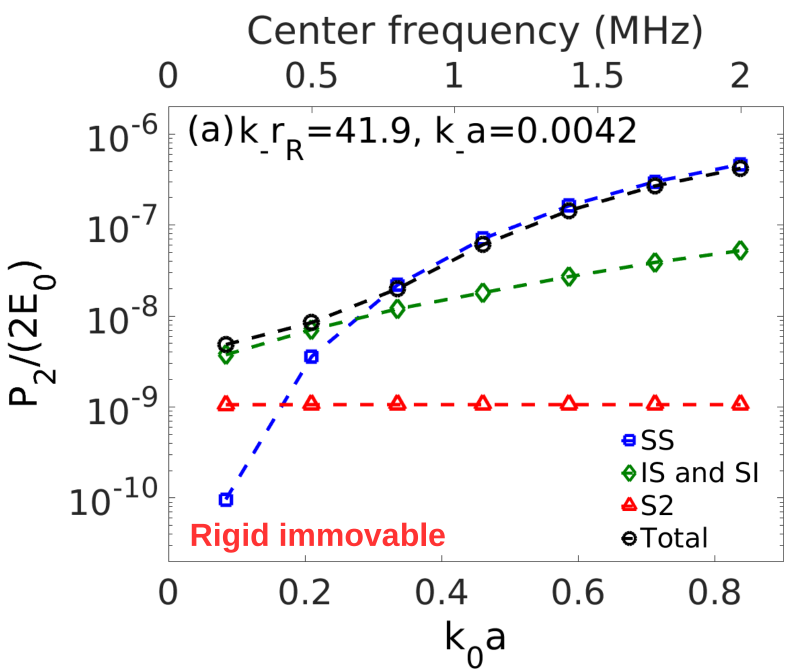

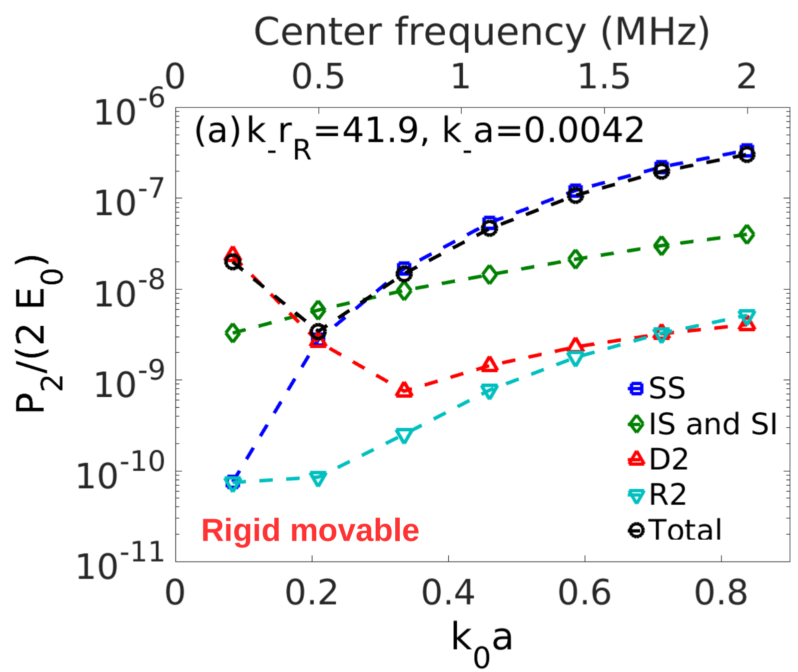

- Upper abscissa: Second order pressure field measured at 1 m away from a 0.1 mm radius sphere in water, where primary and difference frequenices are respectively 1 MHz and 10 kHz.
- Many papers sought to explain difference frequency measurements only in terms of radiation from centroidal motion (Science 1998, PNAS 1999, PRL 2006, Pys.Rev E 2005). We show this is typically an insignificant effect without resonance, R2.
- Problem was previous work arbitrarily considered certain mechanisms
- Current work systematically includes all 2nd order mechanisms
- Similar issues were resolved in nonlinear surface wave hydro in the 1980s

Movable Rigid Sphere In Damped Elastic Structure

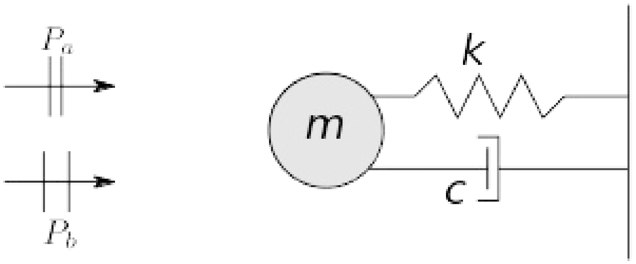

$$\zeta = \frac{c}{2m\omega_0} = \frac{c}{2\sqrt{mk}}, \text{ where } \omega_0 = \sqrt{\frac{k}{m}}$$

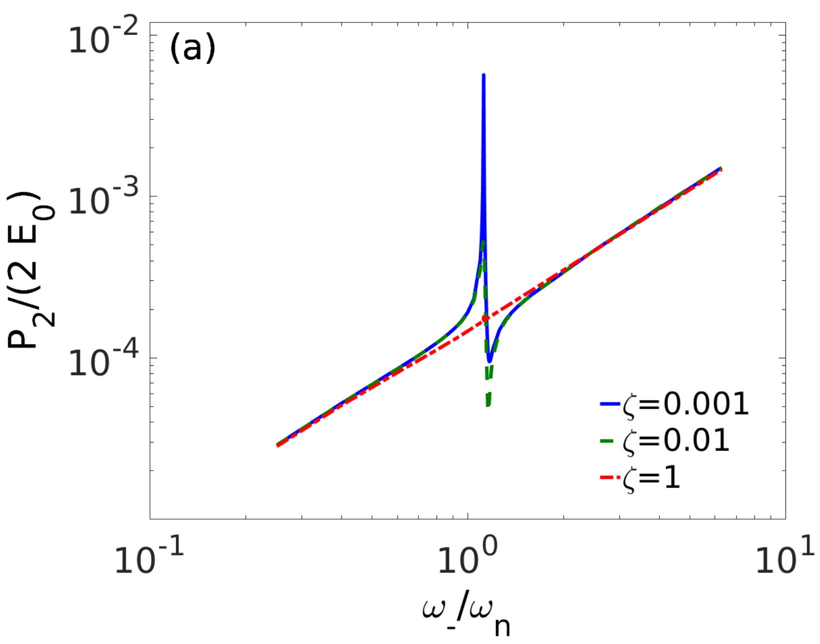

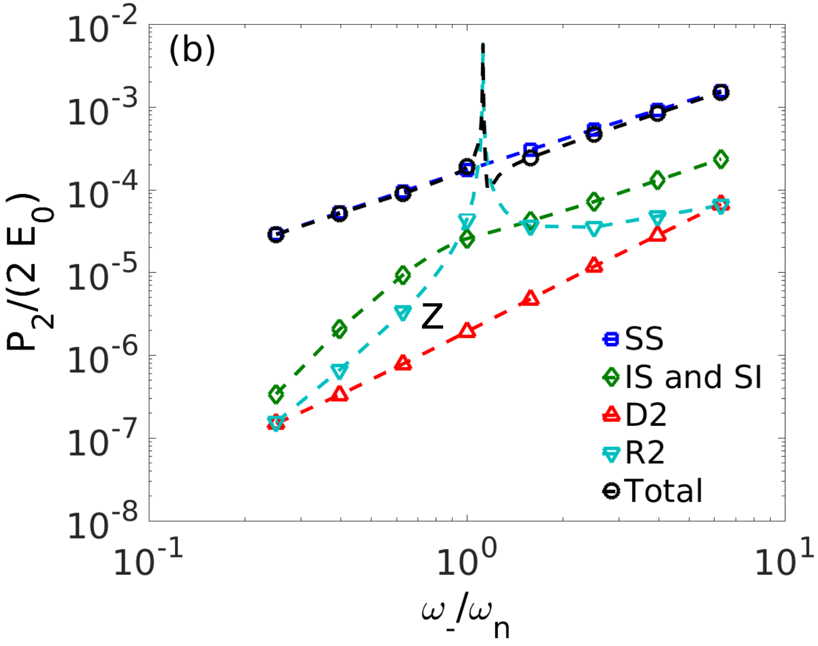

- R2 can become dominant for highly resonant cases.

Sensing Ocean Bubbles With a Parametric Array
Naive S2II Mechanism Assumed in Parametric Array Use Not Correct

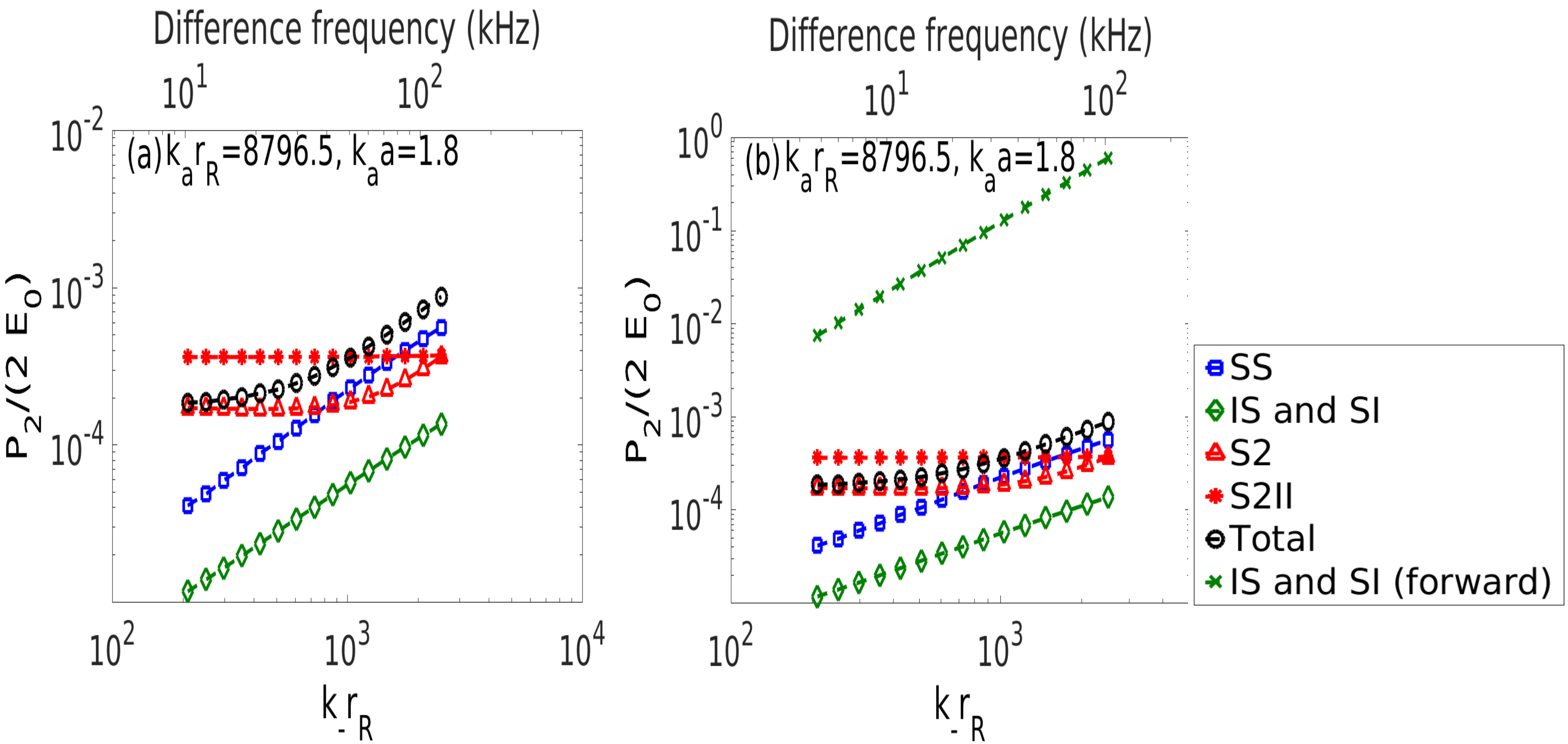

- Upper abscissa: Second order pressure field measured at 4.88 m away from a 0.1 mm radius gas bubble in water, where primary and difference frequencies are respectively 430 kHz and 43 kHz.

Sensing Ocean Bubbles with Pump and Image Frequencies

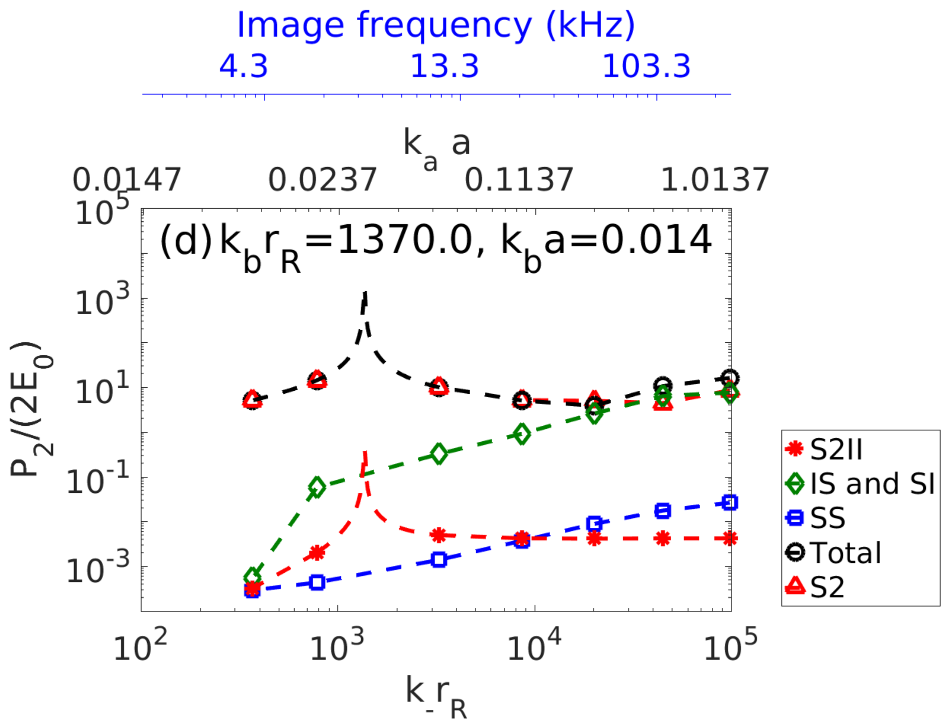

- Primary pump frequency near near surface air bubble resonance, $k \quad a = 0.0137$
- Primary image frequency well above resonance
- Transition between dominant mechanisms
- Example
  - Second order pressure field measured 100 m away from a 1 mm radius underwater bubble with 3.34 kHz primary pump wave frequency and varying primary image wave frequency.

Ocean Fisheries Sensing: Herring at 50 and 100 m Water Depth

Example Notes Issues with Recent Simrad Topaz Parametric Array JASA Paper for Fish Resonance

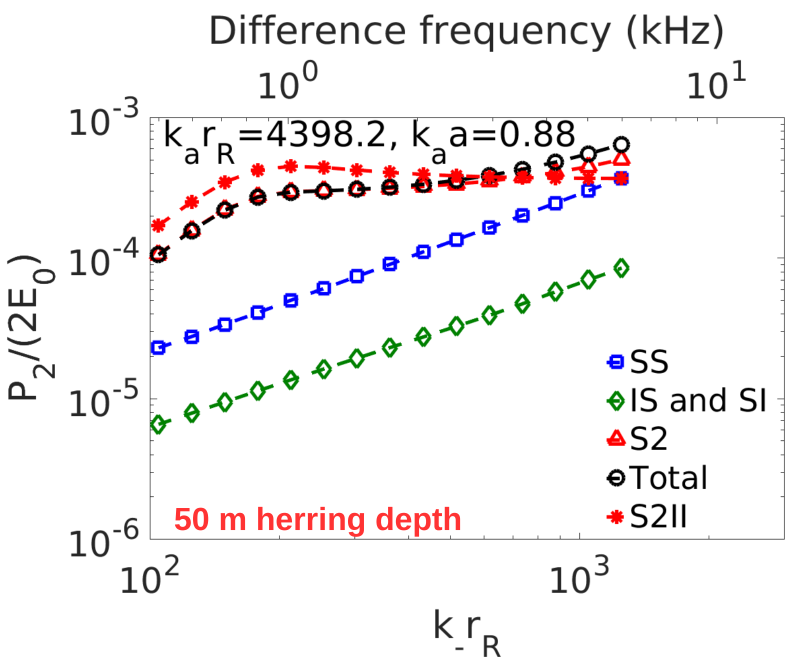

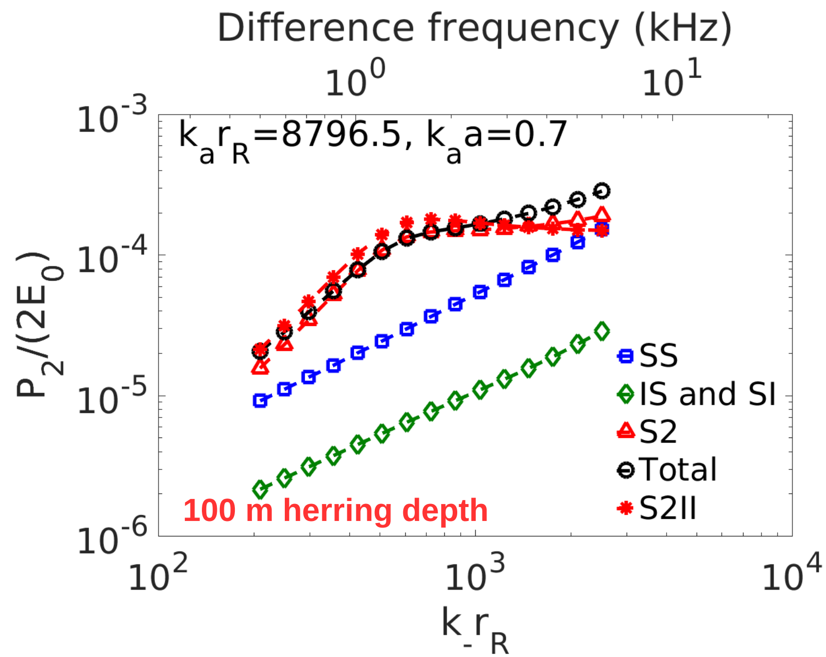

- Equivalent herring swimbladder radius
  - 50 m herring depth: 1 cm
  - 100 m herring depth: 0.8 cm
- Primary frequency: 21 kHz
- Transition between dominant mechanisms
- Naive S2II mechanism assumed in Parametric Array Study is not correct

Ocean Fisheries Sensing with Parametric Array: Cod at 100 m Water Depth

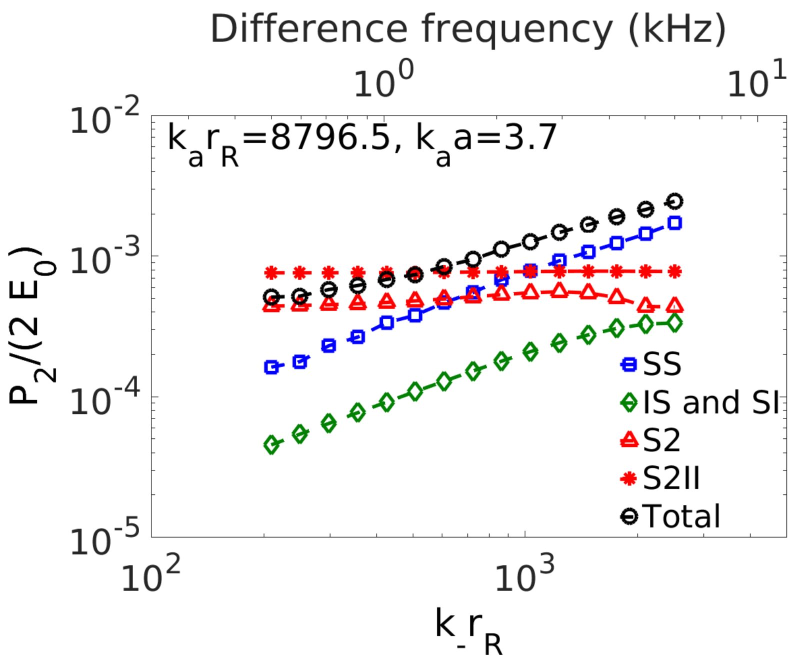

- Equivalent cod swimbladder radius at 100 m: 4.2 cm
- Primary frequency: 21 kHz
- Transition between dominant mechanisms
- Naive S2II mechanism assumed in Paramtric Array use is incorrect

Sensing Objects from IS Interactions

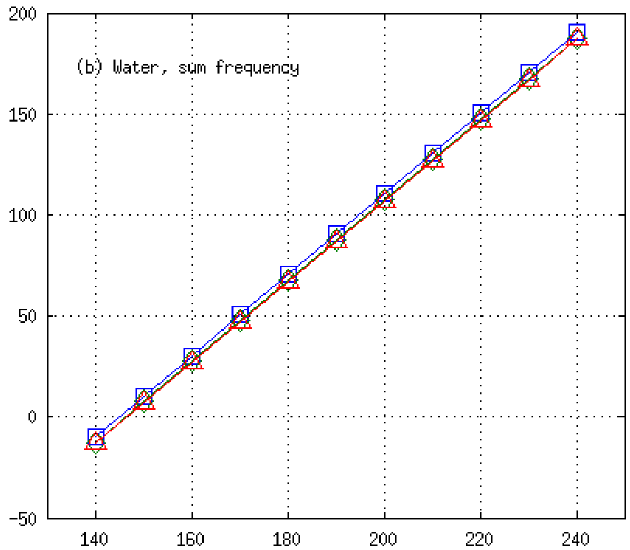

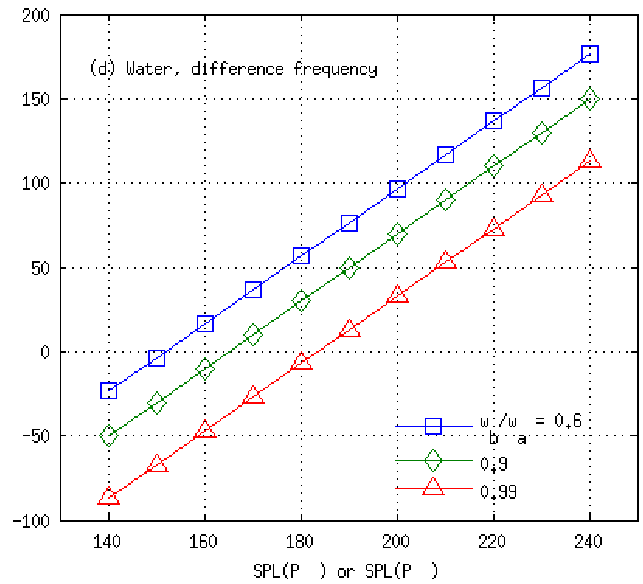

Perpendicular Incidence

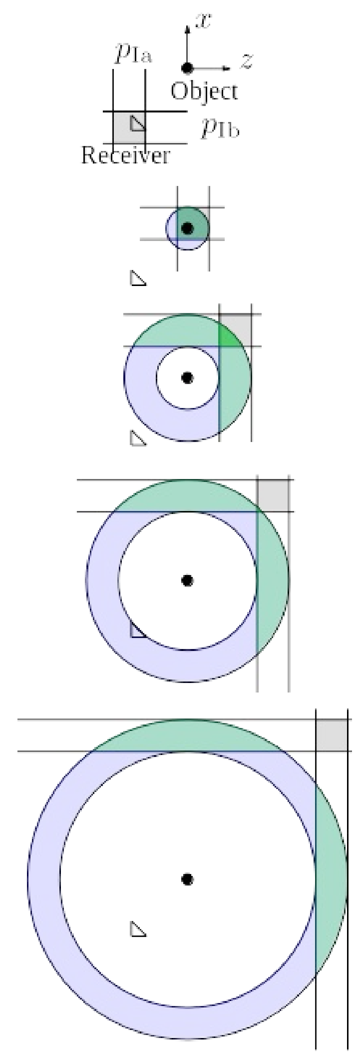

- High frequency incident SPL between 170 dB and 190 dB re 1 μPa gives sum frequency SPL between 48 dB to 90 dB for $\omega_{\mathrm{b}}/\omega_{\mathrm{a}} = 0.6$.
- High frequency incident SPL between 170 dB and 190 dB re 1 μPa gives difference frequency SPL between 37 dB to 77 dB for $\omega_{\mathrm{b}}/\omega_{\mathrm{a}} = 0.6$.

Fundamental Advances in Helmholtz Resonance Theory

where c_{air} :speed of sound in air

C : conductance of sound hole

V : internal volume of air cavity

open window leads to unwanted internal pressure fluctuations known as Helmholtz resonance

- **Conductance of acoustic aperture (sound hole) is proportional to perimeter and not area**
- **Proven theoretically, demonstrated numerically, confirmed experimentally**

Hadi T Nia, Ankita D Jain, Yuming Liu, Mohammad-Reza Alam, Roman Barnas, Nicholas C Makris (2015). *Proc. R. Soc. A*, *471*(2175).

Theoretical proof of proportionality of conductance on sound hole perimeter

Assume potential flow $\Rightarrow u_n = \frac{\partial \phi}{\partial n}$, where u_n is normal velocity at hole and ϕ is velocity potential

Let L be the perimeter of the hole and S be its area

$$C = \frac{1}{2}\iint_S u_n dS \quad \xrightarrow{\text{Boundary element method}} \quad C = \frac{1}{2}\sum_{j=1}^{N}\iint_{s_j} u_n(x,y)dS$$

For each elemental area s_j , from Stokes theorem

$\iint_{s_j} u_n(x,y)dS = \oint_{L_j} Adx + Bdy$, where L_j is total boundary contour of element and $\frac{\partial B}{\partial x} - \frac{\partial A}{\partial y} = u_n(x,y)$

u_n has weak integrable singularity at perimeter of sound hole. Change coordinate system to (x',y') with x' along l_j and y'=0, where l_j is along the perimeter of the hole

$\int_{s_j} u_n(x,y)dS = \int_{l_j} A'dx' + \int_{\Delta l_j} A'dx' + B'dy'$, where $L_j = l_j + \Delta l_j$, $\frac{\partial B'}{\partial x'} - \frac{\partial A'}{\partial y'} = u_n(y')$

$u_n(y') = a(y')^{\beta}$ from 3D corner flow solution, with $-0.5 < \beta < 0$

$\Rightarrow A' = b + \left(\frac{a}{\beta+1}\right)(y')^{\beta+1}$ *and* $B = constant$ is a solution to $\frac{\partial B'}{\partial x'} - \frac{\partial A'}{\partial y'} = u_n(y')$

$\Rightarrow \int_{l_j} A'dx' = bl_j$ where a and b are constants $\Rightarrow C = \frac{1}{2}\sum_{j=1}^{N} bl_j + \underbrace{\frac{1}{2}\sum_{j=1}^{N}\int_{\Delta l_j} A'dx' + B'dy'}_{=0 \text{ (from Stokes theorem)}}$

$\Rightarrow C = \frac{1}{2}bL = \alpha L$, where α is the shape factor that depends on the shape of the hole alone.